Nano-Micro Letters

REVIEW

Check for updates

Recent Advancements and Perspectives of Low-Dimensional Halide Perovskites for Visual Perception and Optoelectronic Applications

Humaira Rafique[1], Ghulam Abbas[1], Manuel J. Mendes[1], Pedro Barquinha[1], Rodrigo Martins[1], Elvira Fortunato[1], Hugo Águas[1] ✉, Santanu Jana[1] ✉

HIGHLIGHTS

- This review uniquely bridges the relationship between 0D, 1D, and 2D structural motifs of halide perovskites and their distinct optoelectronic properties; such as photoluminescence, charge transport, and excitonic behavior and how these impact performance across various devices (e.g., LEDs, photodetectors, synapses). This dimensional-property-functionality mapping is not extensively covered in previous reviews.

- Unlike many earlier reviews focused solely on photovoltaics or LEDs, this article expands into emerging fields like artificial synapses and visual perception-related electronics, offering insights into how low-dimensional perovskites could enable next-generation neuromorphic and intelligent sensing systems.

- The review doesn't just summarize the field it also critically evaluates current limitations in scalability, environmental stability, and device integration, and provides future directions to overcome these, particularly through material design and interfacial engineering, making it highly relevant for guiding industrial research.

ABSTRACT Low-dimensional (LD) halide perovskites have attracted considerable attention due to their distinctive structures and exceptional optoelectronic properties, including high absorption coefficients, extended charge carrier diffusion lengths, suppressed non-radiative recombination rates, and intense photoluminescence. A key advantage of LD perovskites is the tunability of their optical and electronic properties through the precise optimization of their structural arrangements and dimensionality. This review systematically examines recent progress in the synthesis and optoelectronic characterizations of LD perovskites, focusing on their structural, optical, and photophysical properties that underpin their versatility in diverse applications. The review further summarizes advancements in LD perovskite-based devices, including resistive memory, artificial synapses, photodetectors, light-emitting diodes, and solar cells. Finally, the challenges associated with stability, scalability, and integration, as well as future prospects, are discussed, emphasizing the potential of LD perovskites to drive breakthroughs in device efficiency and industrial applicability.

KEYWORDS Low-dimensional perovskites; Light-emitting diodes; Photodetectors; Phototransistors; Photovoltaics
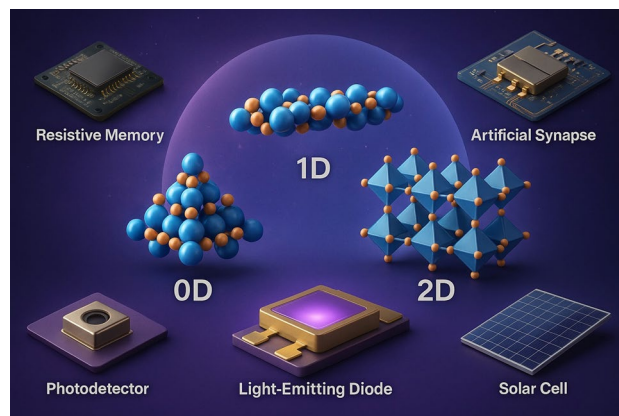
Humaira Rafique and Ghulam Abbas contributed equally to this work.

✉ Hugo Águas, hma@fct.unl.pt; Santanu Jana, s.jana@fct.unl.pt
[1] i3N/CENIMAT, Department of Materials Science, NOVA School of Science and Technology and CEMOP/UNINOVA, Campus de Caparica, 2829-516 Caparica, Portugal

1 Introduction

Dimensionality impacts the electron–matter and light–matter interactions, which affect the characteristics and functionalities of semiconducting nanostructured materials and devices [1]. Over the last three decades, significant advances have been made in the synthesis, processing, and characterization of nanocrystals, one-dimensional (1D) nanowires (NWs), and two-dimensional (2D) quantum wells in typical inorganic semiconductor nanostructures (for example, elemental III–V and metal chalcogenide) [2]. The main goal of these studies is to figure out how dimensions, size, architecture, and compositions impact the characteristics of nanostructures so that new or improved properties and applications may be developed [3]. With critical semiconductor nanostructures, many device systems, including integrated optoelectronic and photonic devices, biosensors, energy conversion and storage devices, could be potentially revolutionized [4, 5]. Among various semiconductor materials, halide perovskites have developed as an important semiconductor class for high-performance solution-processed optoelectronics including lasers [6, 7], photovoltaics [8, 9], and light-emitting diodes (LEDs) [10–12].

The most prominent and unique properties are their high electron/hole mobility and absorption factor, long-range ambipolar transport of charge, high dielectric constant including low exciton binding energy and good defect tolerance. The performance of three-dimensional (3D) hybrid photovoltaics has been boosted with maximum power conversion efficiencies (PCEs), as compared with other established technologies [13]. However, 3D hybrid organic–inorganic perovskite solar cells still lack commercialization due to their unstable behavior [14]. Compared to 3D perovskite materials, the low-dimensional (LD)-hybrid perovskites show better stability against moisture, higher photoluminescence, tunable bandgaps, and lower trap densities, leading to better stable and efficient optoelectronic devices [15]. In comparison with bulk perovskites, LD perovskites have favorable optical and electrical properties, including strong anisotropic absorption as well as emission, higher photoluminescence quantum yields (PLQY), adjustable bandgaps, and high binding energies, and thus could provide a variety of thrilling and potentially unique opportunities. Another advantage is the ease of fabrication of LD perovskite materials via low-cost solution processing and at ambient temperatures in several (0D, 1D, and 2D) forms without a highly sophisticated environment.

In the last decades, LD perovskites have been getting tremendous attention due to their extraordinary properties [16]. The crystal sizes, compositions, and shapes play a dominant role in tuning the density of their electronic states and band gaps, making them artificial atoms. For example, in 2D perovskites, ABX_3 possesses the ability of tenable "A" cation length for the interlayer architecture [17]. This property leads to applying 2D perovskite crystal structures with desirable novel optoelectronic properties. Also, the versatile structures of LD perovskites with better quantum confinement enable them to tune their optoelectronic properties using compositional engineering. Therefore, LD perovskite materials have become the most prominent and efficient candidates for a new generation of several applications based on optoelectronics, including light-emitting diodes [18], phosphorescent material [19], low power transistors [20, 21], exceptionally efficient photodetectors [22, 23], lasers [24], solar cells [25], and printable devices [26, 27].

In parallel with market growth, research and development efforts in flexible electronics have expanded significantly in recent years, as evidenced by the increasing number of publications in the field of flexible and wearable electronics. We analyzed the number of articles published during three distinct time intervals: 2011–2015, 2016–2020, and 2021–2025. Figure 1a illustrates the number of publications on 0D, 1D, and 2D perovskites during each period. A more detailed analysis is provided in Fig. 1b, which highlights the individual contributions of 0D, 1D, and 2D perovskites to the total publications. The percentage of publications focused on 0D materials increased from 18% to 23%, while 2D perovskite research consistently accounted for more than 50% of the total publications on low-dimensional perovskite materials. To gain further insights, we combined the results from 2011 to 2025 to examine the total number of articles across different applications. The data, represented as a pie chart in Fig. 1c, reveal that the majority of publications (72.9%) are focused on solar cells, followed by photodetectors (16%) and light-emitting diodes (LEDs) (approximately 7%). These data were sourced from the Web of Science. In this review article, we briefly discuss the classification, synthesis, and properties of LD perovskites. In addition, the precise structural, optical, and photophysical features are also illustrated that distinguish them as a leading material in the perovskite field. We also summarise the state-of-the-art applications, main challenges, and emerging prospects for LD perovskite-based memory devices, synapse, photodetectors, LEDs, and solar
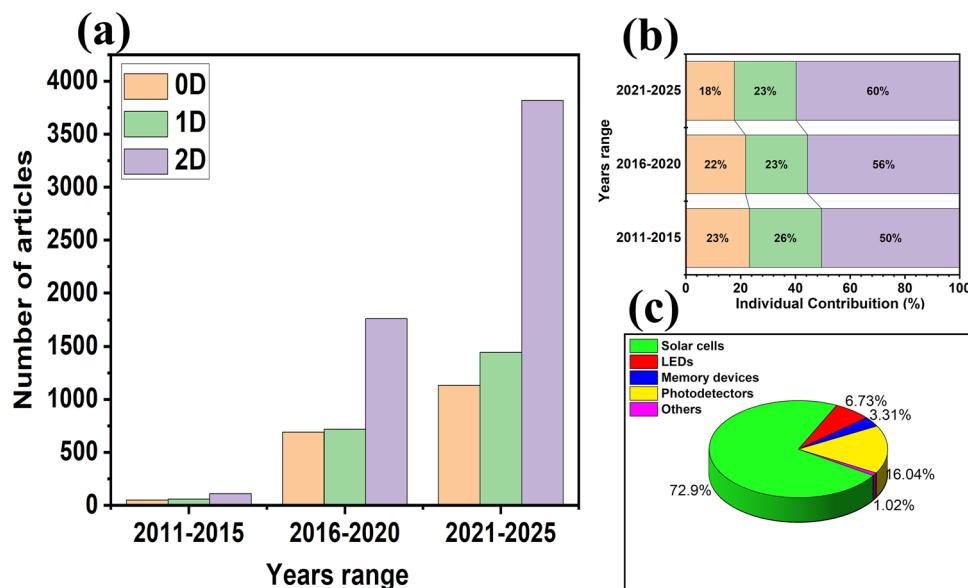
Fig. 1 **a** Number of publications on low-dimensional (0D, 1D, 2D) perovskites from 2011 to 2025 across three-time intervals. **b** Contributions from each low-dimensional perovskite group to the total number of articles. **c** Distribution of publications for different applications of low-dimensional perovskites during the 2011–2025 period

cells with a deep focus toward enhanced device performance and efficiency for industrial applications.

1.1 LD Perovskites Dimensional Classification

The classification of LD perovskites based on their dimensions includes zero-, one-, and two-dimensional perovskites. Zero-dimensional materials include quantum dots, nanoparticles, and nanoclusters, one-dimensional include nanorods, nanowires, and nanotubes, and three-dimensional includes nanoplates, nanolayers, and nanofilms.

Figure 2 shows the structural classification of LD perovskites based on dimensionality, which includes 0D, 1D, and 2D perovskites. The cubic structural diagram of halide perovskites with ABX_3 structure is shown in Fig. 2(left). This structure shows the similarities and differences between
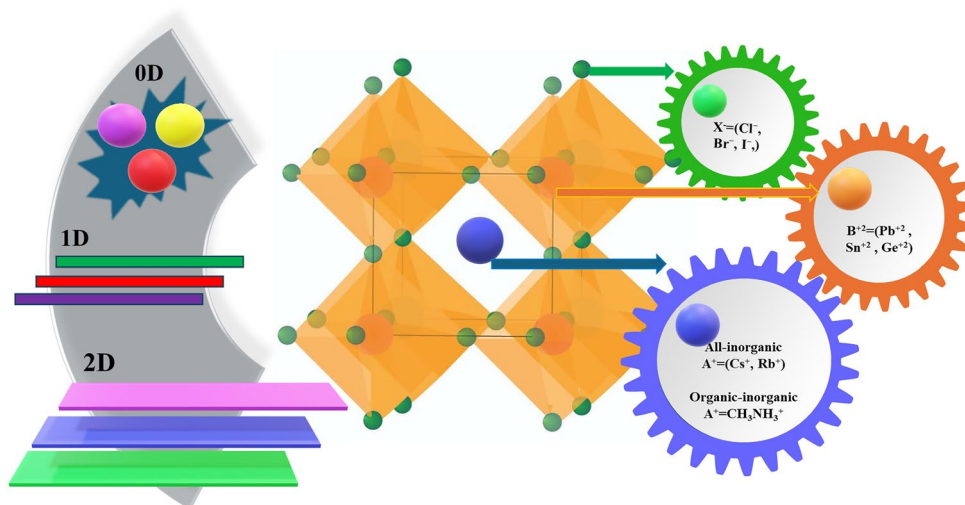

Fig. 2 Classification of LD perovskites based on dimensionality (left) and structural diagram of halide perovskites (ABX_3). Central A site atom (organic or inorganic) determines the nature of all-inorganic or hybrid organic–inorganic perovskites (right)
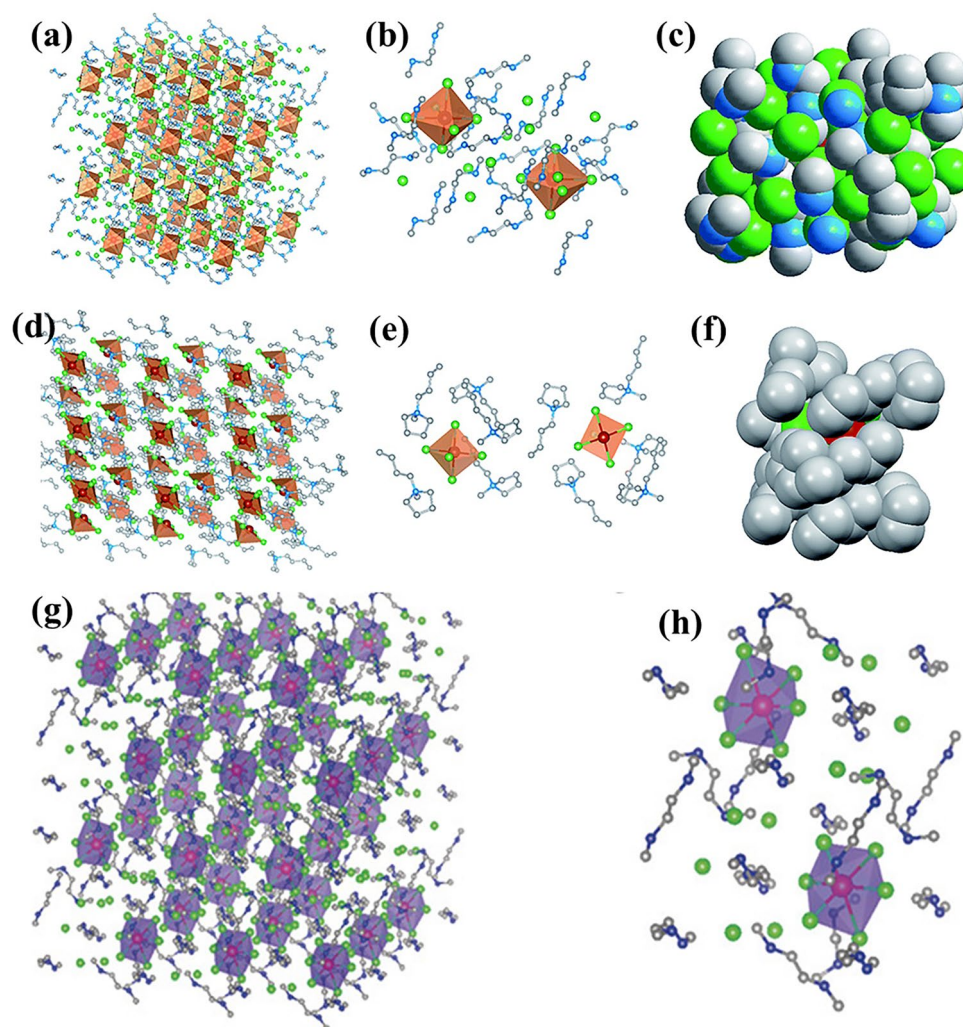
Fig. 3 Single-crystal structures and isolation of 0D organic metal halide hybrids. **a** Crystal structure of $(C_4N_2H_{14}Br)_4SnBr_6$ with $SnBr_6^{4-}$ octahedra (orange) and organic ligands (C/N: gray/blue; Br: green). **b** Two isolated $SnBr_6^{4-}$ octahedra surrounded by $C_4N_2H_{14}Br^+$ ligands. **c** Space-filling model of a single $SnBr_6^{4-}$ octahedron fully encapsulated by organic ligands. **d** Crystal structure of $(C_9NH_{20})_2SbCl_5$ featuring $SbCl_5^{2-}$ quadrangular pyramids (orange) and organic ligands (C/N: gray/blue; Cl: green). **e** Two isolated $SbCl_5^{2-}$ quadrangular pyramids enclosed by $C_9NH_{20}^+$ ligands. **f** Space-filling model of an individual $SbCl_5.^{2-}$ quadrangular pyramid shielded by organic ligands [35]. **g** Crystal structure of 0D Sn bromide perovskite $(C_4N_2H_{14}Br)_4SnBr_6$ and **h** 0D Sn bromide perovskite unit cell [36]

all-inorganic and organic–inorganic hybrid perovskites. The main dissimilarity which differentiates inorganic from hybrid perovskites is the central A site atom (organic or inorganic), which determines the nature of all-inorganic or hybrid perovskites. Commonly used A, B, and X ions are mentioned in green, orange, and blue colors (Fig. 3).

1.1.1 Zero-dimensional Perovskite Materials

0D perovskites have specific structural and optoelectronic properties. Perovskite quantum dots (PQDs) with size less

than its Bohr radii in all three dimensions are considered to be the example of 0D materials [28]. The small sizes result in electron confinement effect and hole wavefunctions [29]. Hence, one can observe that electronic excitations are touching the nanocrystal boundaries and showing better physical, chemical, and optoelectronic properties. These perovskite QDs possess discrete band gaps, and by adjusting the QD sizes, the band gaps may be readily adjusted [30]. Reducing QD sizes may increase the band gap by $1/R^2$ factor, and here, R represents the radius of QDs. The quantum confinement effect enables these PQDs to show narrow emission line

widths and a maximum PL quantum yield toward 100% [31]. These prominent characteristics can be utilized in practical applications of PQDs based optoelectronic devices. Several synthesis methods have been reported for perovskite quantum dots, such as the template-assisted method [32], hot injection method [33], and ligand-assisted method [34].

1.1.2 One-dimensional Perovskite Materials

One-dimensional perovskites are widely investigated for realizing novel optoelectronic performances, due to their superior and fascinating optical properties featuring a high quantum efficiency and a significant surface-to-volume ratio, anisotropic geometry, and better charge confinement compared with bulk materials [38, 39]. Superior crystalline structure and tremendous properties make 1D perovskites one of the most reliable candidates for the next-generation perovskite-based photonic and electronic devices. 1D perovskites possess well-defined crystal structures, unique 1D enclosed surfaces, higher stability, and better film morphology.

There are several methods for the preparation of 1D perovskites, such as solution-processable synthesis, template-based, and vacuum synthesis processes [40]. Several LD perovskites-based optoelectronic devices are reported to show remarkable high photosensitivity, better photoelectric conversion efficiency, and high photoluminescence (PL) efficiency [41–43]. However, 1D perovskites devices have low current outputs and small active areas so that they are not easy to realize practical applications. Researchers are working to overcome this issue by assembling highly ordered architectures of 1D perovskites that maintain the intrinsic properties of individual 1D perovskites [39]. Well-ordered and highly aligned arrays can improve the surface uniformity, current output, active area, and reproducibility of the fabricated devices. Highly ordered 1D arrays are attractive for photovoltaic applications because of the superior light trapping, significant broadband antireflection, and enhanced mechanical properties [44, 45]. The development of well-aligned 1D perovskites will create room for the availability of 1D perovskite-based large-scale and highly integrated optoelectronic devices [44]. Figure 4 shows 1D
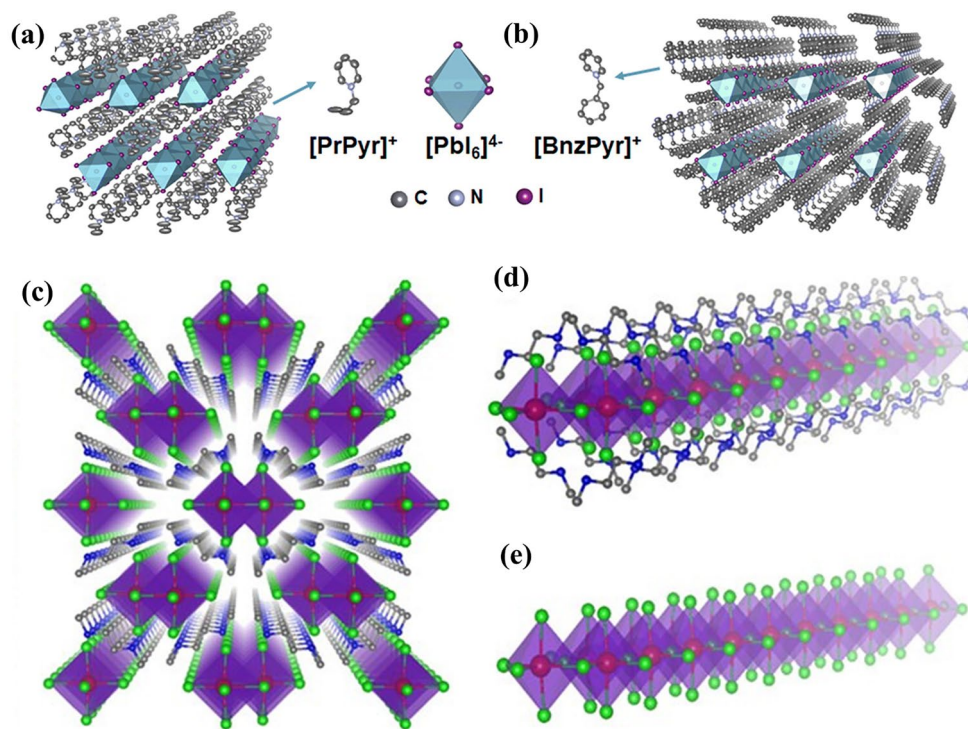

Fig. 4 Structure of 1D halide perovskites. Single crystal structures of **a** 1D lead iodide hybrids (PrPyr)[PbI$_3$] and **b** (BnzPyr)[PbI$_3$]. Here C, N, and I atoms are represented by gray, blue, and purple spheroids, respectively, while the [PbI$_6$]$^{-4}$ coordination sphere represented by cyan octahedron. Insets show the molecular structures of PrPyr$^+$ and BnzPyr.$^+$ cations [46]. **c** Structure of 1D perovskite C$_4$N$_2$H$_{14}$PbBr$_4$. **d** Individual PbBr quantum wire wrapped by the organic cations and **e** PbBr quantum wire with edge-sharing octahedrons [47]

perovskite crystal structure where (a-b) represent the single-crystal structures of (PrPyr)[PbI₃] and (BnzPyr)[PbI₃]. The colors are assigned to each atom as: gray, N: blue, I: purple; [PbI₆]⁴⁻: cyan octahedra. The insets represents organic cations (PrPyr⁺, BnzPyr⁺). Similarly, Fig. 4c shows the 1D perovskite $C_4N_2H_{14}PbBr_4$ where each atoms is represented by a different color like Pb: red, Br: green, N: blue; [PbBr₆]⁴⁻: purple octahedra). Figure 4d, e shows lead bromide quantum wires. Hydrogen atoms omitted in all structures to make the structure simple and easy to understand.

Researchers are developing different assembly methodologies to fabricate 1D arrays [48]. Common techniques involve confinement, meniscus-assisted, and template-guided self-assembly as well as evaporation-induced self-assembly [49]. Every synthesis assembly method gives unique 1D perovskite crystals with different crystal sizes, shapes, aligned horizontal/vertical architecture, periodic structure, other different surface morphologies. Rather than the impact on morphologies and architectures, the synthesis methods have strong influences on the optoelectronic characteristics including charge carrier mobilities, defect states, light extraction, light path lengths, etc. [50, 51].

1.1.3 Two-dimensional Perovskite Materials

LD perovskites have received significant attention in the last decades [52] toward photonic and other optoelectronic applications [53]. As discussed earlier, the main feature of these materials includes their tunable optoelectronic properties [54] with quantum-sized effect [55, 56]. The simple structures of single, double, and multiple layer 2D perovskites and their 3D architectures, and the commonly used organic cations are shown in Fig. 5.

Figure 5a illustrates 3D hybrid perovskite (ABX₃), representing corner-sharing [BX₆]⁴⁻, where A symbolizes an organic cation, B for a metal cation, and X for a halide. In Fig. 5, low-dimensional perovskite structures have been shown with several perovskite layers (n). Here n = 1 represents pure 2D perovskite with R_2BX_4 structure; R represents here a big organic cation. If we increase "n" greater than 1, that is, n > 1, then $R_2A_{n-1}B_nX_{3n+1}$ structure is formed, which leads to the quasi-2D perovskites. $R_2A_{n-1}B_nX_{3n+1}$ is the general formula of 2D perovskites (Fig. 5b) [58, 59]. Figure 5c shows commonly used organic cations and their molecular structures in 2D perovskites.

In recent years, 2D perovskites have got a significant interest in the PV market due to their improved stability. 2D perovskites were initiated in the early 1980s. $(RNH_3)_2MA_{n-1}M_nX_{3n+1}$ is the most used 2D perovskites general formula. By only altering the value of n, we may regulate the thickness of inorganic layers, which has a direct impact on the characteristics of 2D perovskites [60]. Depending upon the values of n, 2D perovskites can be classified into three main classes, if n = 1, then it is called strict 2D, n = 2–5 belongs to quasi-2D, and n > 5 represents quasi-3D perovskites [61]. Most 2D perovskites only consist of the simplest organic cations, such as phenylethyl or butyl ammonium [62]. Now the common interest of researchers is the functional organic cations usage in 2D perovskites so that these functional groups can be utilized to tune the optoelectronic characteristics, leading to better device functionality and efficiency [63, 64].

The flexible structure of 2D perovskites makes plenty of room for materials investigation under compositional engineering, including the choice of R cation. The bulkiest and commonly used R cations are phenylethyl ammonium (PEA⁺) and butylammonium (BA⁺). At the start of the 1990s decade, PEA_2PbI_4 having a bandgap around 2.36 eV and relatively superior exciton binding energy about 200 meV (n = 1) is considered to be the most suitable materials to identify the structure as well as optoelectronic properties for the whole 2D perovskites class [65, 66]. This leads to maximum electroluminescence, high PLQY, and significant optical non-linearity. With the addition of smaller cations, like MA⁺ in PEA⁺ for $PEA_2MA_{n-1}Pb_nI_{3n+1}$, we can get quasi-2D perovskites [67, 68]. Inorganic sheet thickness is also controlled by changing concentrations of MA⁺ ions in different ratios. The most prominent effect of layer thickness is on the bandgap of material which reduces from 2.36 eV (n = 1) to 1.94 eV (n = ∞) by increasing the value of n and reduces exciton binding energy [69]. It has been noted that the number of inorganic layers in a device can not only be used in tuning the optoelectronic properties but also have a strong influence on crystal orientation and crystal formation of 2D perovskites [70]. There is a direct influence of dimensional variation on binding energy as well as band gap on the final material. An increase in dimensions from 0 to 2D of LD perovskites results in the reduction in binding energy and a band gap. Goldschmidt's tolerance factor-derived size constraints are relaxed and provide the vacancy to incorporate larger organic cations into structure showing the change of
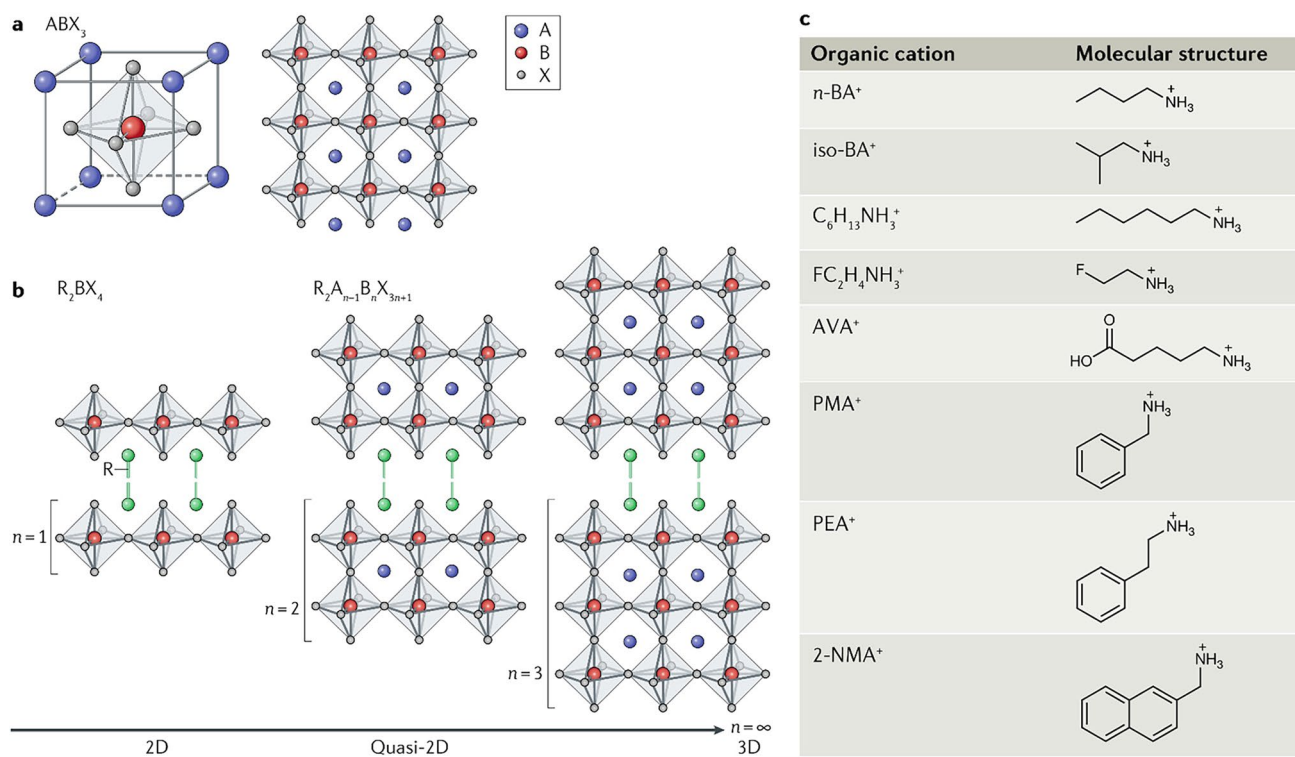
Fig. 5 3D and 2D perovskite's structure. **a** ABX$_3$ structure 3D hybrid perovskite, **b** single-, double-, and multiple-layer 2D perovskites. **c** Commonly used organic cations for 2D perovskites [57]

exciton binding energy and modulate the bandgap of materials [71, 72].

1.2 Compositional Classification

1.2.1 Organic–Inorganic Hybrid Halide Perovskites

The revelation of organic–inorganic hybrid perovskites materials with two-dimensional (2D) structures has enhanced potential in energy harvesting as well as energy storage technologies (e.g., solar cells, LEDs, laser, photodetector, and memory devices). These materials contain metal halide anions and organic cations. A number of hybrid organic–inorganic two-dimensional materials were described by Mitzi et al. in the 1990s with <110> metal halide layers [73]. Later, Kagan et al. utilized 2D perovskites as active semiconducting channel layers [20]. A boom in the use of metal halide perovskites was observed after 2009 when Miyasaka et al. firstly reported. These materials serve as photovoltaic (PV) cells' visible light sensitizers with 3.8% power conversion efficiencies (PCE) [74]. The PCE improves dramatically in a decade from 3.8% (2009) to 25% (2020) [75] due to narrow band gap, well-separated electron–hole pairs, maximum mobility, economical and cost-effective fabrication methods. Considering electroluminescent devices, the first room temperature electroluminescent device consisting of organic–inorganic hybrid halide perovskites was fabricated in 2014 [76]. Recently, the structural control for better quantum confinement is of great interest by reducing the dimensionality of bulk 3D to well-arranged 2D levels [77]. Metal halide layers make an important contribution during phase transformation from 3 to 2D by reducing the number of layers with tailorable band gaps and photoluminescence [78]. It is not easy to obtain the 2D perovskite from bulk 3D by mechanical exfoliation or some other techniques adopted for MoS_2 or graphene. Generally, chemical vapor deposition and solution-based synthesis are adopted for ultra-thin 2D perovskite layers growth. Luckily, PbX_2 has van der Waals arrangements in $MAPbX_3$ which can be availed to make PbI_2 flakes and further utilized to make $MAPnB_3$ by chemical transformation methods [79]. The thickness of resultant perovskites can be controlled from a few to hundreds of layers according to the requirements.

Organic–inorganic hybrid perovskites have attained superior consideration in the optoelectronic industry because of their marvelous properties including tunable bandgap, simple fabrication methods, higher absorption coefficient, which leads to achieve unprecedented PCE of more than 25% [75]. However, the main hindrance in commercialization in organic–inorganic hybrid perovskites is the instability of organic parts under broad exposure to light and relatively higher temperatures. Thermal instability is mainly caused by MA^+ and FA^+ cations due to their decomposition at elevated temperatures of 85 and 150 °C for $MAPbI_3$ and FAPbI thin films, respectively.

1.2.2 Inorganic Halide Perovskites

Inorganic perovskite resolved the thermal instability issue by substituting Cs^+ ions in the place of organic cations in the precursor solution. $CsPbX_3$ was reported in early 1983 but their structure and photo responsive properties were studied in 1958. Recent reports have witnessed that inorganic perovskite possesses better stability and commercialization strength than hybrid perovskites. Considering the synthesis of 2D inorganic perovskites the colloidal synthesis technique is widely adopted [80]. $CsPbBr_3$ were synthesized by Bekenstein et al. at higher temperature by directly injecting Cs-oleate solution into $PbBr_2$ solution having other solvents including oleylamine, octadecene, and oleic acid [81]. Synthesis temperature plays a dominant role to control the size, thickness, and shape of resulting nanoplates. Precise analysis reveals that experiments conducted at 150 °C mostly produce nanocubes, while low-temperature synthesis (~ 130 °C) could be used to make nanoplates with 20 nm lateral dimension and thickness of ~ 3 nm. The ion exchange method is another synthesis technique for $CsPbI_3$ and $CsPbCl_3$ nanoplates deposition onto multiple substrates by centrifugal casting for device fabrication [82]. Small lateral sizes ~ 20–300 nm are not sufficient for the assessment of fundamental properties for device fabrication. Shamsi et al. reported rectangular shaped, better lateral sizes from 300 nm up to a few micrometers of ultra-thin $CsPbBr_3$ sheets and completely dissolving in oleic acid to present short ligands [83]. Oleic acid has been effectively used as a solvent for Cs-oleate which leads to the formation of nanoplates in a broader temperature range (50 to 150 °C). To achieve sizeable and well-controlled lateral dimension (300 nm to 5 mm)

nanoplates, optimum ratios of shorter ligands, octylamine, and octanoic acid can be added into the solution [84].

1.2.3 2D Ruddlesden–Popper (RP) and Dion–Jacobson (DJ) Perovskites

The poor stability of halide perovskites is still a critical issue that needs to be addressed before this low-cost, solution-processable PV technology can be commercialized on a wide scale. Introducing bulky or long-chain monovalent organic cations was previously shown to be a successful method for improving the chemical stability of halide perovskites. Due to better environmental stability, the Ruddlesden − Popper (RP) 2D perovskites got significant attentions from researchers. Commonly single (sometimes multiple) inorganic sheets are sandwiched between organic spacers in 2D perovskites attached by Coulombic forces, such as $C_3H_7NH_3^+$ (PA$^+$), $C_4H_9NH_3^+$ (BA$^+$), and $C_8H_9NH_3^+$ (PEA$^+$), to form 2D RP perovskite phase. As a result, it is exciting to see if customized cation designs might offset the negative impacts of interlayer structures like those found in 2D RP perovskites, allowing for greater stability while limiting carrier transport in solar cells.

Recently, 2D Dion–Jacobson (DJ) perovskites phase with chemical formula $(A)_{n-1}B_nX_{3n+1}$, and alternating cation interlayer (ACI) phases with chemical formula $(A')(A)_nB_nX_{3n+1}$, are attracting a lot of attention from researchers in optoelectronics. The difference of A′ cation makes DJ and ACI phases different. The detailed selection of A, B, and X and structural differences between DJ, RP, and ACI phases are shown in Fig. 6. The chemical formulas of DJ and ACI are a derivative from ABX_3. 2D DJ phase of perovskites can be fabricated by eliminating van der Waals gaps in RP which leads to better structural strength for photovoltaics [85]. These one-of-a-kind interlayer chemistries favor increased stability while allowing for more carrier hopping/tunneling. As a result, the promise of DJ and ACI LHPs to obtain more optimal device performance in solar cells has been demonstrated. The main distinction is the octahedral configuration in these structures has been shown in the middle panel of Fig. 6. The tightly packed interlayers consisting primarily of modest or small cations favor ACI with GA/MA combinations, resulting in a very low distance of ≈3 Å.
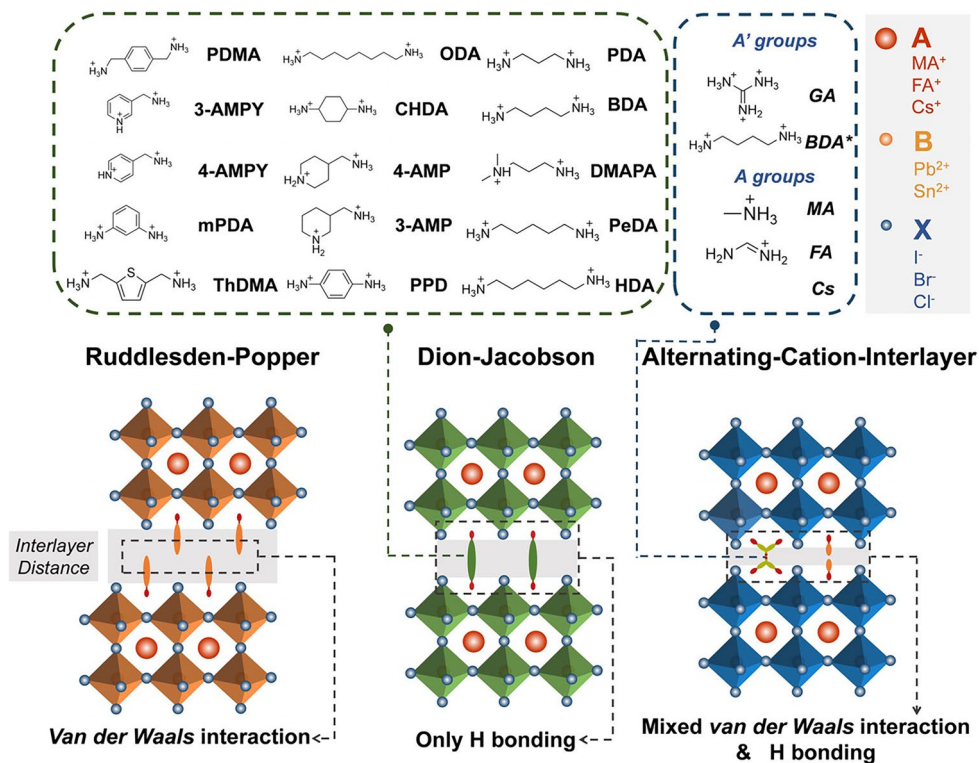
Fig. 6 Brief structural comparison between RP, DJ, and ACI phases, with most frequently adopted interlayer cations [86]

There is still an opportunity for further reduced interlayer distances of ACI to be developed.

Better efficiencies of these phases for photovoltaics and structural stability lead to the long-term utilization of fabricated devices by maintaining 95% of initial PCE for 4,000 h at normal air exposure, damp heat (85 °C and 85% RH, 168 h.), and light illumination for 3,000 h.

1.3 Synthesis of LD Perovskites

Understanding growth, as well as assembly mechanisms, is essential to achieve good controllability on the fabrication and improved device performance applications. The preparation route has a significant impact on structural morphologies and performances of the devices based on LD perovskite materials. The feasible synthesis technique to make them available for industrial applications is always desirable. In this section, the solution phase, vapor phase deposition, and templated synthesis have been demonstrated in a controllable and versatile way for the uniform and better geometry LD perovskites nanostructures. Some important factors

that significantly affect the film quality including deposition temperature, solvent concentration, substrate temperature, and annealing conditions are also reviewed.

1.3.1 Solution Phase Synthesis

Several groups are working to attain a few layers of uniform and compact 2D perovskites, high-quality single crystals, and other LD nanostructures by using solution-processable techniques. Solution-based syntheses offer the benefit of allowing for mass manufacturing of colloidal nanostructures for optoelectronic device fabrication with ambient synthesis conditions including low cost and heterolayer deposition feasibility. As a result, solution-based synthesis techniques (both bottom up and top down) are widely used in the fabrication of several nanostructures [79]. Falling a precursor solution on the substrates and then evaporating the solvent resulted in the formation of ultrathin 2D MHP NSs [87, 88]. Another method for assisting the precipitation of 2D MHP nanostructures is to introduce poor solvents to the precursor solution. Zhang et al. used toluene as a poor

solvent to grow $(PEA)_2PbI_4$ $(PEA = C_8H_9NH_3)$ NSs. After drop casting, they added toluene to the precursor solution and gradually evaporated the solvents [89]. According to Chen et al., the presence of particular polar solvents in the solution can effectively limit crystal development along the c axis, resulting in ultrathin 2D MHPs once the solvent is evaporated [90]. Yuko et al. used a one-step synthesis method for the growth of 2D $(C_3F_7CH_2NH_3)_2PbBr_4$ perovskite by using acetone as a poor solvent. They attained the dielectric as well as quantum confinement effects by using this one-step solution deposition technique [91]. Furthermore, Zhai et al. used a two-step solution synthesis technique with the addition of a ternary solvent for the fabrication of large sized 2D $(C_4H_9NH_3)_2PbBr_4$ perovskites. Figure 7a schematically illustrates the synthesis procedure of these 2D $(C_4H_9NH_3)_2PbBr_4$ perovskites. Starting with the dissolution of $PbBr_2$ and $C_4H_9NH_3Br$ in DMF solvent and undergoing a two-step deposition, the solution crystallizes into 2D $(C_4H_9NH_3)_2PbBr_4$ perovskite instantly after evaporation [92]. The concentration of perovskite precursor and crystallization temperature were shown to be two important parameters influencing the final morphology of the products. The volume ratio effect of DMF on the morphology of perovskites films was studied and recorded for several concentrations. At a higher ratio of DMF (33.3%), the precursor concentration is very small, and randomly shaped perovskites were found. By making the solution more concentrated and decreasing the ratio of DMF up to 9.1%, the fine perovskites cubes were achieved with uniform sizes as shown in Fig. 7b. The concentration of DMF has significant effect on the nucleation density and size of 2D $(C_4H_9NH_3)_2PbBr_4$, by reducing the DMF ratio results in the increase in nucleation density of perovskites and also enhancements in the sizes of the perovskites significantly. Surprisingly the shapes and random morphologies of perovskites were completely transformed into well-aligned cubes. This evolution can be explained by the supersaturation phenomenon, which dominates the development mode of perovskites and transforms them into a cubic shape with enhanced nucleation density. Cloutier and co-workers used solution-processable synthesis technique to fabricate 1D hybrid perovskite nanowires and utilized them to make flexible photodetector [93]. The schematic for the production and deposition of perovskite nanowires on a flexible Kapton substrate using the spin-coating approach is shown in Fig. 7c, the fabricated

nanowires are highly dense and cover the entire surface of the flexible substrate. Figure 7d shows a high-magnification SEM image of a $CH_3NH_3PbI_{3-x}(SCN)_x$ perovskite nanowires network deposited on Kapton substrates. Like 2D and 1D perovskites, the 0D perovskite quantum dots are also fabricated by solution-processable techniques. There are several reports in which different researchers reported the growth of barred and capsulated perovskite quantum dots by solution-processable methods [94, 95]. These quantum dots were then utilized to fabricate highly efficient optoelectronic devices [96–98]. Guo and co-workers used one-step ultrasonication bath treatment approach to make $CH_3NH_3PbBr_3$ PQDs [94]. The diagram of complete "ultrasonication bath synthesis" process is shown in Fig. 7e. The process starts with the mixing of $PbBr_3$ and CH_3NH_3 by ultrasonication followed by the formation of $MAPbBr_3$ and absorption of ligands onto $MAPbBr_3$ to form stable perovskite quantum. Blue background in all images shows the presence of TL solution. The TEM image of synthesized QDs is shown in Fig. 7f.

1.3.2 Vapor Phase Synthesis

The preparation route has a significant impact on structural morphologies and performances of the devices based on LD perovskite materials. The feasible synthesis technique to make them available for industrial applications is always desirable. In this section, the solution phase, vapor phase deposition, and templated synthesis have been demonstrated in a controllable and versatile way for the uniform and better geometry LD perovskites nanostructures. Some important factors that significantly affect the film quality including deposition temperature, solvent concentration, substrate temperature, and annealing conditions are also reviewed.

Comparing the crystallinity and defect density among mechanical exfoliation, solution-based, and vapor-phase techniques, the vapor phase synthesis is considered to be the better choice for higher quality LD nanostructures [99]. This is also advantageous for charging transport and several other properties in optoelectronic applications. Waleed et al. used the CVD technique to grow $CsPbI_3$ NWs in a tube furnace having two heating environments [100]. Li et al. [101] have reported a single-source vacuum thermal evaporation (VTE) technique for the synthesis of $CsPbBr_3$ films as shown in Fig. 8a.
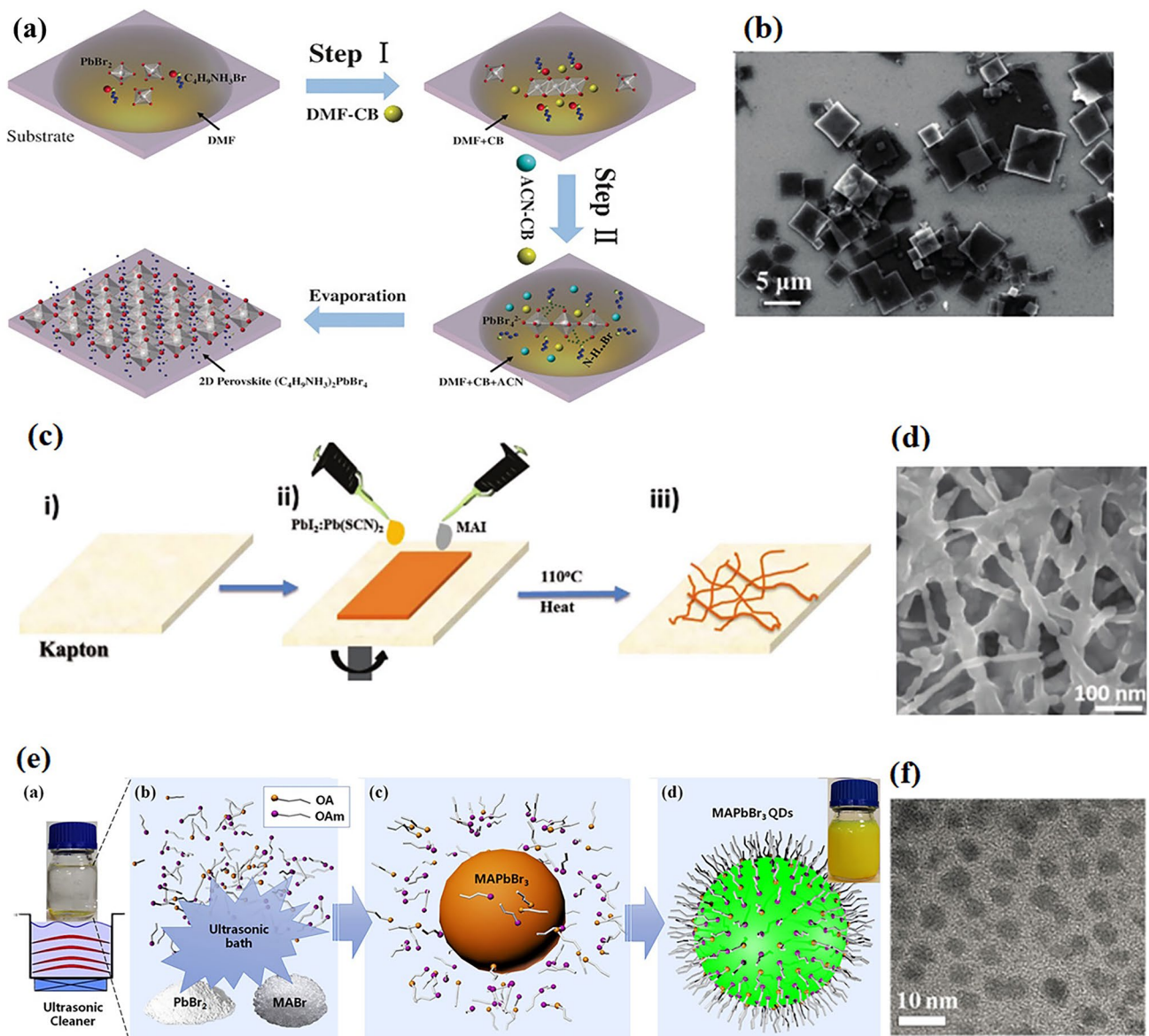
Fig. 7 Solution-processable synthesis. **a** Two-step deposition of 2D $(C_4H_9NH_3)_2PbBr_4$ perovskite. **b** Morphological SEM image of 2D $(C_4H_9NH_3)_2PbBr_4$ synthesized at 9.1% DMF ratios [92]. **c** Synthesis schematic of $CH_3NH_3PbI_{3-x}(SCN)_x$ perovskite NWs growth on flexible tape. **d** SEM showing fabricated perovskite nanowires [93]. **e** Schematic showing all states of ultrasonic bath synthesis for $CH_3NH_3PbBr_3$ perovskite quantum dots. **f** TEM image of synthesized $CH_3NH_3PbBr_3$ perovskite quantum dots [94]

Vapor phase synthesis has been widely used for perovskite nanostructures, by treating pre-grown lead halide nanostructures with gaseous MAI. They used CsBr and $PbBr_2$ precursors to make pinhole-free and highly compact $CsPbBr_3$ nanostructures. They also employed these perovskite films in photovoltaics, observing the influence of thickness and precursor material molar ratio on stoichiometry and photovoltaic performance. The device performance of

$CsPbBr_3$ PSCs enhances from molar ratio at 0.6:1 to 0.9:1 and then reduces constantly to 3.57% by increasing the molar ratio to 1.1:1. Wang et al. [102] produced 2D $MAPbI_3$ perovskite NPs by one-step CVD method on mica substrates. They used dual precursors ($PbCl_2$ and $MACl_2$) for the direct growth of 2D $MAPbI_3$ perovskite NPs. The schematic for dual precursor deposition is shown in Fig. 8b [103]. Xiong et al. utilized a two-step CVD approach to manufacture
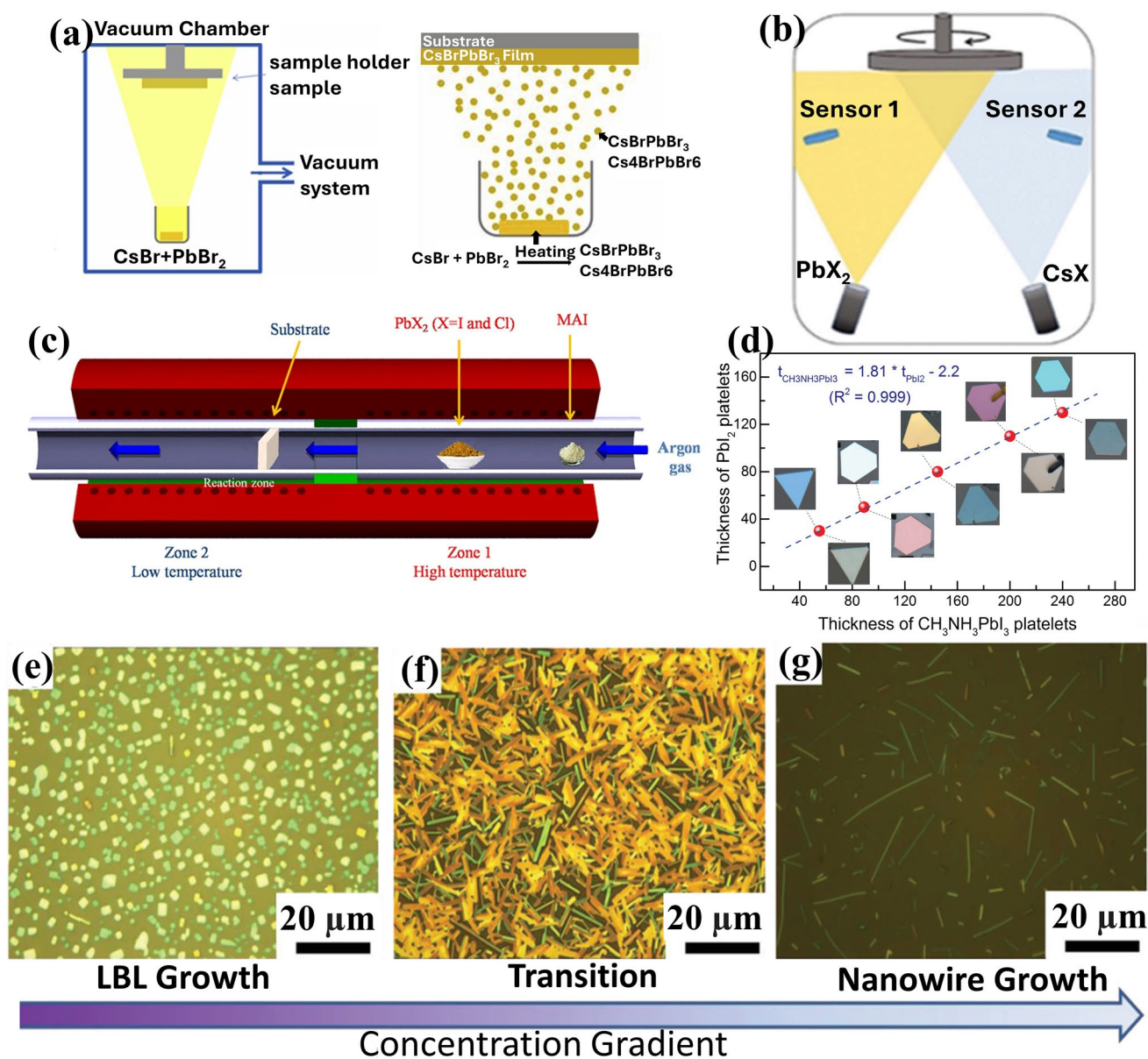
Fig. 8 Schematic illustration of 2D perovskite deposition. **a** Single-source, **b** double-source deposition vacuum deposition method [101]. **c** Tube furnace synthesis of MAPBX$_3$ [104]. **d** PbI$_2$ platelet thickness and color variation before (above data line) and after (below data line) conversion to CH$_3$NH$_3$PbI$_3$. Growth regimes as a function of supersaturation [79]. **e–g** Shape progression from nanoplatelets to nanowires as seen using an optical microscope. **e** Layer-by-layer (LBL) development at high precursor concentrations. **f** Intermediate transition state. **g** At decreasing precursor concentrations, the transformation to nanowire development occurs [105]

high-quality 2D MAPbI$_3$ platelets. They grew PbI$_2$ crystals on muscovite mica via VDW epitaxial growth and later transformed it to perovskite into a CVD furnace by interacting with MAI molecules. The thickness fluctuation of PbI$_2$ platelets earlier (pictures above data line) and after conversion to CH$_3$NH$_3$PbI$_3$ is shown in Fig. 8d (images below data line). The color of PbI$_2$ platelets altered in proportion to

the thickness change (assessed by AFM). The thickness of the CH$_3$NH$_3$PbI$_3$ platelets was around 1.8 times that of PbI$_2$ platelets, which is roughly in line with the two compounds c lattice constant ratio [79]. Commonly used two temperature zone furnaces consisting of the furnace, gas source, exhaust system, and quartz tube reactor are mentioned in Fig. 8c [104].

The concentration of deposited solution also plays a dominant role in the 2D crystal growth. Ghoshal, et al. used a CVD technique to examine the effect of concentration on the growth of 2D $(C_4H_9NH_3)_2PbI_4$ perovskite. During the growing process, the depositing substrate was placed on the quartz tubes and kept at a pressure of 600 mtorr. The diagram depicts the growing process (Fig. 8e-g) demonstrates the concentration-dependent growth of samples of different morphologies. Higher concentration can be used to attain layer-by-layer (LBL) growth as shown on the substrates which were closest to precursors (nanoplatelets growth) as mentioned in Fig. 8e, while low concentration or farthest substrates from precursors grow as nanowires (Fig. 8g). The intermediate positions between LBL nanoplates and nanowires are shown in Fig. 8f [105]. Shaojuan et al. [106] used CVD fabrication in order to investigate the impact of different substrates on the morphology of fabricated 2D perovskites. They reported the controlled synthesis of 2D perovskite with higher quality on several substrates, including flexible polydimethylsiloxane (PDMS), mica, SiO_2/Si, Si, and glass substrates.

1.3.3 Templated Synthesis Method

The liquid synthesis methods are widely used to fabricate perovskite materials with different thicknesses and phases [81, 107]. It is not easy to make a uniform assembly of perovskite nanowires by the solution method. Normally, mixtures of rods, wires, plates, and cubic structures are obtained with different size variations. It is also not possible to align the randomly distributed nucleation center and make equal sizes nanocrystals, nanowires or nanorods by solution-processable method. The alignment and orientation control of 1D perovskites are very difficult to achieve by simple solution-processable synthesis methods [108]. Therefore, to control alignments, pinholes, coverage area, aspect ratio, and orientation of the nanowires, the researchers are using the template method. They found the template-based method very effective to achieve an array of aligned micro- and nanofibers, nanowires, and nanotubes with adjustable diameter and length.

In this technique, a template (either nanoporous membrane) with uniform size pores of the same diameter is used to confine the precursor material into the required nanofibers/wires shape and structure and guide the growth

direction [109]. Several porous materials can be used as templates to fabricate nanofibers and nanotubes. Uniform sizes and diameters of pores allow achieving control over dimensions of the nanofibers. The difficulties of the template-based synthesis method include selection of appropriate templates, filling the pores/template with perovskites, and then removing the template after the growth of the required material. All these challenges are worth exploring to enhance nanowire quality.

Fan and co-workers reported nanoengineering templates to fabricate 3D perovskite $(CH_3NH_3SnI_3)$ nanowire arrays and used them for the first time in photodetectors with higher stability [110]. They also replaced the toxic Pb with Sn to make it environment-friendly and nontoxic. They employed a multistep manufacturing process, beginning with polishing and anodizing an Al foil to create a PAT having nanopore pitch and size, then electrochemically depositing Sn at the bottom of nanopores, as illustrated in Fig. 9a. Furthermore, the sample is placed next to $CH_3NH_3I_3$ powder in a tube furnace at 170 °C to make $CH_3NH_3SnI_3$ NWs. Complete fabrication steps are shown in four parts of Fig. 9a. $CH_3NH_3I_3$ vapors are carried to the PAT by Ar carrier gas, where they react with Sn nanoclusters within the PAT's nanopores. They also reported the decomposition process in the $CH_3NH_3SnI_3$ thin film and NWs. Decomposition in thin films is fast due to the presence of pinholes as schematically shown in Fig. 9b. This is unavoidable, although it can be mitigated by reducing grain boundary area and increasing grain size for improving stability. Regarding NWs, the PAT can effectively protect the MAI NWs due to its chemically and mechanically robust, electrically insulating, and optically transparent nature. As a result of the PAT protection, the NWs will disintegrate vertically, taking longer to break down the full NW array. A schematic of the interaction of water molecules with thin film and NWs is shown in Fig. 9b. Surface morphology and shapes of NWs are mentioned in Fig. 9c where SEM images show the apex of the grown $MASnI_3$ NWs in a well-organized PAT. Perfectly hexagonal structures can be seen from SEM images; Fig. 9c displays a cross-sectional SEM representation of NWs and the bottom images show different alignments and cubic crystal structures of as-grown NWs.

Kovalenko and co-workers synthesized the colloidal Pb halide perovskite nanocrystals with a bright emittance of pure colors that cover the whole visual spectrum [111]. They reported the superiority of these nanocrystals over conventional quantum dots due to their defect-tolerant photo
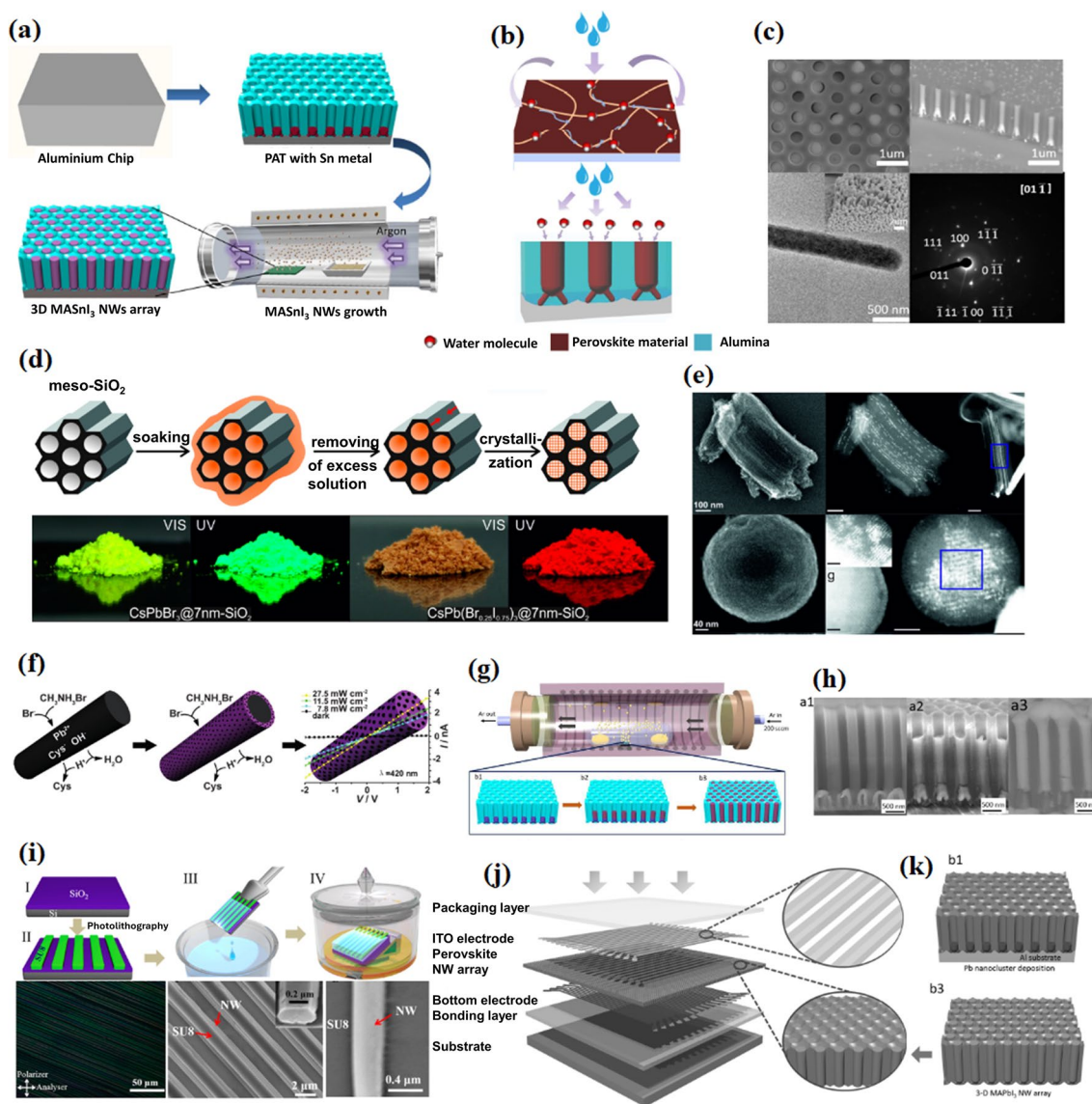
Fig. 9 **a** Schematic diagram of template-based tin perovskite NWs obtained from MAI. **b** Decay of tin perovskite thin film (top image) and NWs sidewall protection of PAT from moisture (bottom). **c** Surface, top, and cross-sectional SEM image of tin perovskite nanowires and TEM of single NW [110]. **d** Multistep templated growth of $CsPbX_3$ NCs in mesoporous silica pores. Bottom optical images show the mesoporous silica with CsPb (Br0.25I0.75)3 NCs (right) and $CsPbBr_3$ (left) under UV and daylight. **e** SE-STEM and HAADF-STEM images of the partially filled samples with $CsPbI_3$ NCs. Followed by EDXS of the area highlighted in the next Figure (bottom last Fig. 9e) [111]. **f** Synthesis of porous $CH_3NH_3PbBr_3$ nanowires by self-template-directed chemical transformation [112]. **g** Schematic of CVD growth process of $FAPbI_3$ NWs. Bottom images (b1-b3) show the template-assisted growth of vertically aligned NW array. **h** Cross-sectional SEM of NWs, grown at multiple steps [113]. **i** Schematic of the growth process for the fabrication of $CH_3NH_3PbI_3$ NW array. Bottom images showing a cross-polarized optical image of the $CH_3NH_3PbI_3$NW array and SEM image of NW array grown on the photoresist strips [114]. **j** Structural schematic of $MAPbI_3$ NWs based image sensor with a magnified image showing 3D NW array inside the nanoengineering template. **k** Schematic showing the growth of high-density and vertically aligned $MAPbI_3$ NW array: Pb in PAM before (b1) and after (b3) $MAPbI_3$ NW growth [115]

physics. They used mesoporous silica pores as templates and filled these templates with perovskite precursors. The obtained perovskite NCs were also able to achieve very brilliant PL with quantum efficiencies reaching 50% after drying. The schematic of synthesis assembly is shown in Fig. 9d. Scanning transmission electron microscopy (STEM) was used for the structural analysis of meso-SiO_2 samples with different pore sizes, e.g., impregnated with either MAPbI3 or $CsPbI_3$ at 7, 4, and 2.5 nm as shown in small figures of Fig. 8e. The first figures show the mesoporous

structure with 1D channel of about 2.2 nm separation. The filling of pores with $CsPbI_3$ can be seen by area selective energy-dispersive X-ray spectroscopy (EDXS) and dark field mode (HAADF-STEM) Fig. 9e (bottom). The final shape and sizes of filled material depend upon the pore sizes and shapes and can be homogeneously distributed throughout the entire particle within its porous structure. Continuing the preparation of porous perovskite nanowires, Zhang and colleagues created porous perovskite ($CH_3NH_3PbBr_3$) nanowires using a self-template-directed synthesis method at ambient temperature and employed them in high-performance photodetectors [112]. They employed a room temperature solution method, using lead-containing precursor nanowires as the Pb source and sacrificial template. The conversion of Pb-containing nanowires into porous perovskite nanowires proceeds via a self-template-directed reaction with HBr and CH_3NH_3Br. The final 1D structure is formed by the disintegration of organic components. Initially, layers based on perovskites were formed on top of Pb-containing nanowires. Pb has a significant chemical reactivity with HBr and CH_3NH_3Br leads to the formation of $CH_3NH_3PbBr_3$. The brief mechanism is shown in Fig. 9f.

Gu et al. used a vapor phase growth technique at a very limited level in nanoporous templates to stabilize the black phase of $FaPbI_3$ nanowires [113]. $FaPbI_3$ with higher decomposition temperature and lower disintegration process has been widely used in high-efficiency and long-term stable optoelectronic devices. Especially the alpha phase of $FaPbI_3$ is very prominent, and numerous unique optoelectronic characteristics are exclusive to the alpha phase. Unfortunately, the desired alpha phase converts into the undesirable delta phase, which has significantly worse optoelectronic properties. Fan and co-workers overcome the stability issue by applying the nanoengineering templates approach to the cubic black phase of $FAPbI_3$ and achieved stability over 7 months without any further treatment at ambient conditions. They also reported the 8 days stability in an extremely humid environment with 97% humidity. Figure 9g depicts the $FAPbI_3$ NWs growth process in a schematic diagram. Cross-sectional SEM images showing the development of NWs at various phases are shown in Fig. 9h(a1-a3). Figure 9h(a1) shows the initial Pb clusters before the growth of NWs, Fig. 9h(a2) shows half-grown NWs, and Fig. 9h(a3) shows the over-grown NWs.

Deng et al. fabricated high quality with smooth surface single-crystal perovskite NWs employing the fluid-guided

antisolvent vapor-assisted crystallization technique on a large scale [114]. The fabricated NWs consist of $MAPb(I_{1-x}Br_x)_3$ arrays with x = 0, 0.1, 0.2, 0.3, and 0.4. Figure 9i shows the schematic of the step-by-step growth process of single-crystalline perovskite ($CH_3NH_3PbI_3$) NW arrays. Initially, they fabricated photoresist stripes on the SiO_2/Si substrate by photolithography. These strips act as a template to grow these NW arrays. The further process consists of dipping the photoresist template into $MAPbI_3$/DFM solution, dragging it out with the hanging solution, placing with CH_2Cl_2 solvent on a tilted glass (~5°), and sealing the fabrication assembly bottle at room temperature. The perfectly constant color shows the growth of continuous and uniform NW arrays at a large scale (Fig. 9i). SEM image shows perfectly aligned NWs with inset showing well-shaped and uniform angular facets (inset in Fig. 9i 2nd SEM image). The last SEM image at higher magnification shows the smooth and crack-free surfaces of $CH_3NH_3PbI_3$ NW arrays (Fig. 9i). Gu et al. used a novel vapor solid–solid reaction (abbreviated as VSSR) method for the growth of 3D $MAPbI_3$ NW arrays in porous alumina membrane (PAM); these PAM are applied to nanoengineering templates [115]. The growing process is initiated by Pb metal nanoclusters at the base of vertical nanochannels. Nanochannels are crucial for controlling the geometry of 3D NWs and grow ultrahigh NW density. Gu et al. used the 3D NWs to fabricate high-efficiency image sensors. Figure 9j depicts a magnified diagram of 3D NW array inside the nanoengineering template, as well as the six-layer structural device of an image sensor based on 3D-NW arrays. The 3D $MAPbI_3$ NW array is between bottom gold (Au) metal electrode and the upper ITO electrode. Figure 9k shows the schematic of perovskite NW development at high density in a PAM. Figure 9k(b1) leads in PAM before and after $MAPbI_3$ NW growth (Fig. 9k(b3)).

1.3.4 Growth of Single-Crystal LD Perovskites

Perovskite single crystals (PSCs) with higher optical absorption, smaller trap-state density, higher carrier lifetime, and better carrier mobility make them prominent than 3D PSCs. 2D layered PSCs are considered an alternative to typical 3D PSCs with better stability and higher performance toward optoelectronic devices. However, the implementation of 2D PSCs is limited by the lack of preparation methods for the high-quality and uniform growth of PSCs. 2D PSC-based
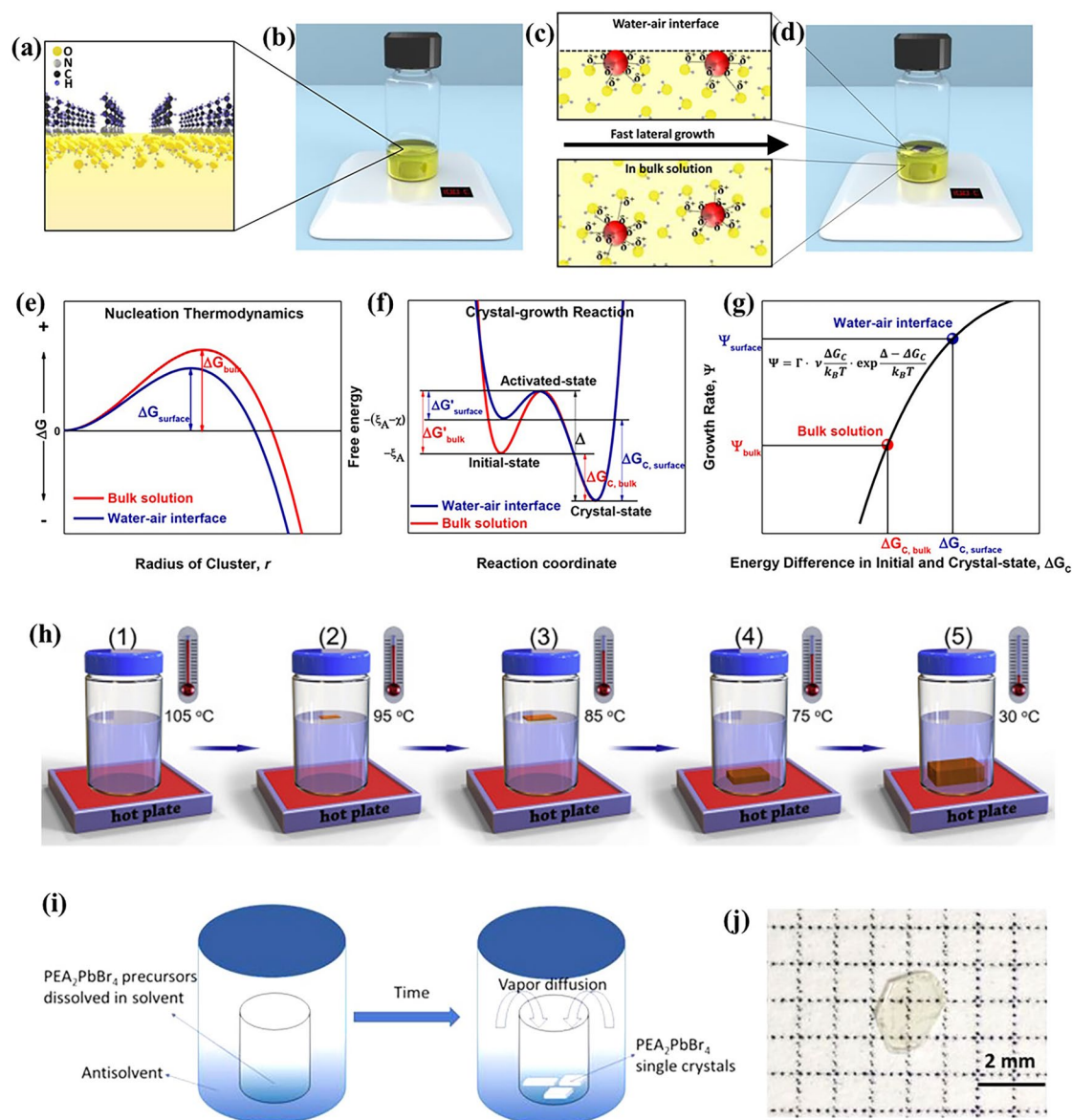
Fig. 10 Illustration and experimental setup for the synthesis of PEA$_2$PbBr$_4$ single crystals at the water–air interface. **a** Schematic of molecular assembly at the interface during nucleation. **b** Experimental arrangement with a precursor solution heated on a hot plate. **c, d** Comparison of crystal growth dynamics at the interface and within the bulk solution, highlighting the rapid lateral growth at the interface. **e** Nucleation thermodynamics showing the difference in energy barriers for bulk versus interfacial nucleation. **f** Energy landscape of the crystal growth process, indicating transitions between initial, activated, and crystalline states. **g** Growth rate dependence on energy variations in different environments [116]. **h** Controlled cooling approach for crystal formation at different temperatures [117]. **i** Vapor diffusion technique for crystallization using an antisolvent. **j** Optical image of a PEA$_2$PbBr$_4$ single crystal [118]

devices exhibit better performance than 3D PSCs for certain optoelectronic applications, particularly those fabricated on the (001) plane. Wang et al. employed density functional theory (DFT) and nucleation theory to develop a supersaturated solution. They then applied the concept of thermodynamic proportionality to temperature to synthesize quasi-2D

perovskite single-crystal membranes (C$_4$H$_9$NH$_3$)$_n$(CH$_3$NH$_3$)$_{n-1}$Pb$_n$I$_{3n+1}$ (where n = 1, 2, 3, 4, and ∞) [116]. The schematic illustration and growth mechanism are shown in Fig. 10. Figure 10a depicts the orientation and alignment of the butyl-ammonium cation, while Fig. 10b presents the experimental setup for the growth process. Figure 10c, d illustrates the

interaction of molecules, where the tensile force on the molecules at the water–air interface is higher. Figure 10e-g provides a graphical representation of the cluster radius dependence on nucleation, variations in the large free energy, and a comparison of the growth rates of precursor molecules in bulk versus the air–water interface, respectively. Similarly, Liu and co-workers used the advantage to grow the 36-mm sized 2D $(PEA)_2PbI_4$ PSCs by using the concept of classic nucleation theory [117].

Figure 10h shows the step-by-step process schematic of $(PEA)_2PbI_4$ PSCs growth assisted by the surface tension mechanism. Tian et al. fabricated exfoliated $(PEA)_2PbBr_4$ 2D PSCs and then fabricated resistive switching memory on them [118]. Figure 10i shows the schematic of the growth process of $(PEA)_2PbBr_4$ of PSCs, and Fig. 10j shows the photograph of a transparent 2 mm single crystal. Recent advancements in crystallization techniques have enabled the growth of large, high-quality 2D perovskite single crystals, leading to devices with remarkable performance metrics, including high responsivity and fast response times. These developments pave the way for the commercialization of PSC-based devices in photodetection and imaging technologies.

1.3.5 Theoretical Simulations and AI-Assisted Design for LD Perovskites

The fundamental properties of low-dimensional perovskites can now be investigated effectively using atomistic simulations and first-principles computations. The unique characteristics of LD perovskites are best understood through theoretical investigations and structural simulations. MD simulations and DFT are two computational methods that are frequently used to forecast their electronic band structures, stability, and defect tolerance. Hardik et al. investigated the effects of A site cation changes (formamidinium (FA) and methylammonium (MA)) on their optical, electrical, and structural characteristics. With potential power conversion efficiencies of 30% and strong optical absorption in the visible and ultraviolet spectrums, both technologies hold potential for solar cells. The results offer important facts for developing and refining 2D perovskites for cutting-edge optoelectronic applications [119]. Dong et al. use DFT calculations to examine the connection between the band gap (E_g) and dielectric constant (ε) in LD perovskites ($CsPbX_3$,

$X = Cl, Br, I$). A theoretical framework for comprehending dielectric behavior is provided by the establishment of a linear connection between ε and $1/E_{g2}$. This study enhances LD perovskites and helps build effective materials for solar cells, LEDs, and other optoelectronic devices [120].

Ozorio et al. examine how the stability and optoelectronic characteristics of two prototype structures $C_{20}H_{20}N_4B_2X_{10}$ (edge-sharing octahedra) and $C_{30}H_{25}N_6BX_6 \cdot 2H_2O$ (isolated octahedra) are affected by halide anions (Cl, Br, I) and trivalent cations (Bi, Sb). They observe that halide substitution affects structural stability and bandgap more than cation substitution, with greater bandgaps and higher stability resulting from smaller halides (Cl) [121]. Hang et al. theoretically investigate the structural and optoelectronic properties of the lead-free perovskites $RbGeBr_2Cl$ and $RbGeI_2Cl$, using DFT calculations with the Perdew–Burke–Ernzerhof (PBE) functional and the GW approximation for accurate bandgap predictions. They demonstrate that both materials have direct bandgaps, tunable optoelectronic properties, and significant UV absorption [122]. The structural, electrical, optical, and thermoelectric characteristics of LD perovskites, namely $Cs_2B'GeCl_6$ (where B' = Zn, Cd), are investigated utilizing sophisticated theoretical techniques based on DFT. The generalized gradient approximation (GGA) and hybrid functional techniques are used in computations to assess important features such density of states (DOS), band structures, optical absorption spectra, thermoelectric performance, and lattice parameters [123].

Regarding MD simulations, Beck et al. perform MD simulations to study the binding and structural properties of the halide perovskite $MAPbI_3$. van der Waals (vdW) corrections, particularly the Tkatchenko–Scheffler (TS) and many-body dispersion (MBD) techniques, are shown to be essential for accurate predictions of lattice constants and bulk modulus. Methylammonium (MA) orientation has an impact that shows that antiparallel MA configurations result in octahedral tilting and lower system energy, while parallel alignment preserves cubic symmetry but poorer stability. Highlighting the importance of dynamic effects, the results provide a computational framework for perovskite material engineering [124]. Magnus et al. use MD simulations to study the structural dynamics of two-dimensional Ruddlesden–Popper perovskites (2D RPPs) with the general formula $BA_2MA_{n-1}Pb_nI_{3n+1}$, where n is the number of inorganic lead iodide layers, BA is butylammonium, and

MA is methylammonium, providing significant insights on the effects of dimensionality on organic cation dynamics and inorganic framework. In 2D systems, MA rotation is more limited by the asymmetric environments produced by BA spacer layers, whereas BA mobility is impacted by its interaction with the inorganic framework and screening by MA cations. Findings demonstrate the intricate relationship between the dynamics of organic components and the inorganic lattice structure in low-dimensional perovskites [125].

Rafael et al. promote the use of lead-free perovskites ($XSnI_3$, X = Cs, K, Rb) in solar cells for green policy efforts by using MD simulations to examine the mechanical characteristics of these materials under environmental stressors. Anisotropic mechanical behavior by simulations, with $RbSnI_3$, shows the lowest stiffness (0.131 GPa) and $CsSnI_3$ the greatest (Young's modulus: 1.361 GPa). Stress tolerance is strongly influenced by temperature and pressure; performance peaks at 270 K and decreases at higher pressures (200 MPa) [126].

Considering the AI and machine learning for the development of LD perovskites, Ruiyang et al. employed ML-driven approach to predict the structural dimensionality of LD perovskites based on ammonium cation properties and found four important chemical descriptors: steric effect index (STEI), eccentricity (Ec), largest ring size (LRS), and hydrogen-bond donor count (HDC) after compiling 86 reported amines and categorizing them as either 2D-forming or non-2D-forming. They developed an 82% accurate prediction model using logistic regression [127]. Wissam et al. employed an AI-driven method that speeds up materials screening by orders of magnitude in comparison with DFT, which highlights the significance of structural features in property prediction while facilitating the effective exploration of large chemical spaces. They further illustrate how hierarchical ML models can fill computational and experimental gaps in perovskite design and can improve its forecasting potential for optoelectronic applications [128]. Also, Songyang et al. uses a K-nearest neighbor model to predict the dimensionality (2D, 1D, or 0D) of LD perovskites based on organic spacer characteristics with 92.3% accuracy. They draw attention to how AI-assisted design has sped up the discovery of LD perovskites, and the incorporation of theoretical simulations in the future may improve prediction accuracy [129]. Sum et al. offer a geometric data analysis (GDA)-based machine learning method for designing 2D perovskites. They suggest using an innovative method

termed density fingerprinting (DF) to depict the periodic and geometrical structural details of perovskite unit cells. To forecast material characteristics, especially bandgaps, these DFs are coupled with a gradient boosting tree (GBT) model [130].

2 Applications for LD Perovskites, Advances, Challenges, and Perspectives

2.1 Fundamental Advantages over Conventional Semiconductors

LD perovskites challenge traditional semiconductors by integrating high-performance properties with remarkable solution processability, unlike silicon, which necessitates epitaxial growth at higher temperatures [131]. Low-temperature (< 150 °C) solution processing allows LD perovskites to reach exceptional electrical quality [132]. New developments in 2D Ruddlesden–Popper perovskites have shown that out-of-plane charge carrier mobilities can surpass 100 cm^2 V^{-1} s^{-1} [133], rivaling single-crystal silicon and allowing for flexible electronics that are not possible with inorganic materials that are stiff. These materials exhibit particularly remarkable quantum confinement effects; in 2D perovskites such as $(PEA)_2PbI_4$, exciton binding energies can approach 200–400 meV [135, [135]. These values are significantly higher than those of transition metal dichalcogenides (~ 20–100 meV) and GaAs (~ 4 meV), which are typical semiconductors [136], permitting strong excitonic occurrences at normal temperature. LEDs have demonstrated exceptional device performance due to this basic advantage, retaining 28.5% external quantum efficiency at realistic brightness levels of 10,000 cd m^{-2} [137].

The special qualities of LD perovskites address long-standing issues in a variety of optoelectronic applications. In terms of display technology, they provide higher color purity with NTSC 150% color gamut while also overcoming the efficiency roll-off that organic LEDs (OLEDs) lacks [137]. In photovoltaics, LD perovskite/silicon tandems use dimensionality-controlled bandgap tuning (1.2–2.3 eV) [138] to possibly achieve efficiency levels beyond 40%, which are beyond the reach of single-junction silicon cells. New developments in on-chip photonics have shown that 2D perovskite optical modulators with a bandwidth of 100 GHz can surpass traditional silicon photonic devices while still

being compatible with CMOS [139–141]. Exact comparisons between organic and inorganic ETLs in perovskite devices have been made possible by numerical modeling studies in 2023–2024; under simulated module settings, inorganic variations exhibit greater thermal and photostability. When included into $CH_3NH_3SnI_3$-based architectures, Cu-based inorganic HTLs showed over 18% efficiency and strong performance metrics, making them perfect for the deployment of scalable, affordable solar modules. Full-scale PV simulations verify that inorganic transport layers provide long-term operational reliability under a variety of environmental conditions in addition to lowering recombination losses [142–145].

Research in 2023–2024 has shown previously unheard-of possibilities using LD perovskites. 2D perovskite memristors with ultralow 0.1 fJ energy per switching event [9] and 10^6 unique conductance states are advantageous for neuromorphic computing applications, offering a $100\times$ improvement over traditional oxide-based devices. The cryogenic restrictions of conventional quantum dots have been removed by room temperature single-photon emitters that exhibit 90% purity [146], revolutionizing quantum technologies. 0D $Cs_3Cu_2I_5$ X-ray detectors outperform commercial amorphous selenium systems in medical imaging, achieving an impressive sensitivity of 0.07 μGy_{air} s^{-1} at just 1 V bias [147].

The qualities which make LD perovskites very remarkable include the reversible bandgap tuning via mechanical strain that surpasses 300 meV [148]. For innovative optical applications, natural light polarization ratios are greater than 10:1 [149]. Also, inorganic-like charge transport and molecular tunability are made possible by hybrid organic–inorganic activity [150]. These developments put LD perovskites in a position to facilitate whole new technological paradigms rather of only serving as substitutes for current semiconductors. Future research directions should focus on establishing global stability standards for implementation in the industry [151] and employing high-throughput screening to create extensive materials databases [152], as well as integrating modern manufacturing processes to expand production [153].

2.1.1 Limitations of LD Perovskites

LD perovskites are a promising family of semiconductor materials, but to reach their full potential, a number of important issues need to be resolved. Anisotropic charge transfer, ambient instability, and production scalability concerns are the most urgent restrictions; they have all received a lot of study attention lately.

Significant differences in charge transport characteristics are caused by the intrinsic anisotropy of 2D perovskites. Significant quantum confinement effects can cause out-of-plane mobilities to surpass 100 cm^2 V^{-1} s^{-1} [154], whereas insulating organic spacers restrict in-plane transport, which usually exhibits mobilities under 20 cm^2 V^{-1} s^{-1} [155].

Significant gains have been made recently in molecular engineering, with conjugated spacers such as thieno[3,2-b]thiophene-2-ethylammonium showing increased environmental stability and enhanced charge transfer (up to 65 cm^2 V^{-1} s^{-1} in-plane mobility) [156]. To further optimize charge transport channels, preferred orientation of quantum wells has been made possible by innovative crystallization procedures that involve solvent vapor annealing [157].

One of the key challenges is maintaining environmental stability while operations are underway. Degradation processes including organic cation breakdown and halide migration continue to occur even though LD perovskites exhibit better stability than their 3D counterparts [158]. Recent advancements in encapsulation technology have shown notable gains in stability, especially in the deposition of hybrid organic–inorganic barriers using atomic/molecular layers [159]. After 2,000 h of constant illumination at 85 °C, for example, devices with AlO_3/parylene nanolaminate encapsulation retained > 95% original efficiency [160]. Fluorinated spacer cations have also been used to increase intrinsic material stability, improving both thermal stability up to 150 °C and moisture resistance [161]. Another major obstacle to commercialization is manufacturing difficulties. Inconsistent phase distribution and film shape are frequently caused by the intricate crystallization processes of LD perovskites. Many of these problems have been resolved by recent advancements in deposition methods and ink engineering [162].

It is now possible to create homogenous films over 15×15 cm^2 regions with a thickness variation of less than 5% thanks to slot-die coating and improved solvent solutions [163]. Furthermore, phase purity and orientation control in large-area devices have been enhanced using vapor-assisted crystallization techniques [164]. Rapid examination of hundreds of processing parameters is now possible because of the advent of high-throughput screening technologies, which
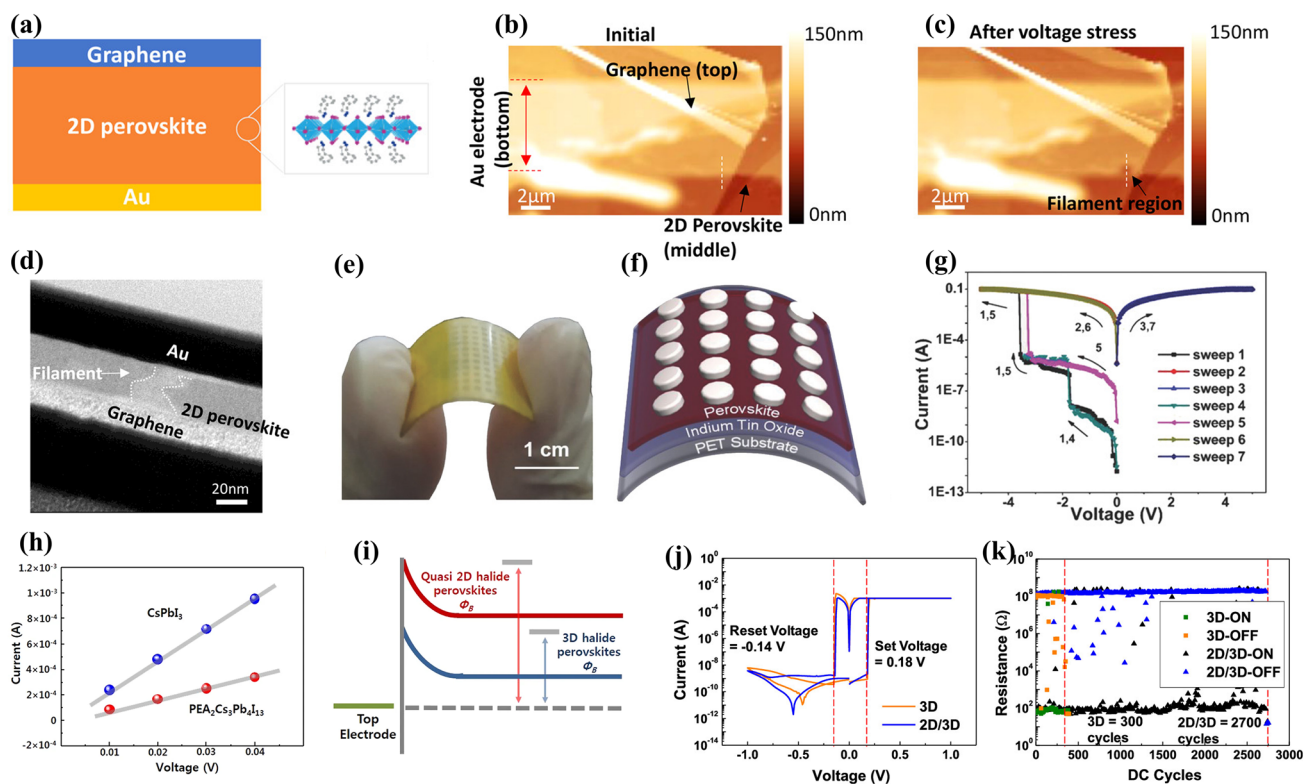
Fig. 11 **a** Structural schematic of graphene/2D perovskite/Au vertical device. **b** AFM of a fresh and **c** after the application of pulsed voltage. **d** TEM image representing filament shape in white dotted line at ~30 nm (diameter) close to graphene and approx. 15 nm close to Au side [118]. **E** Original and **f** schematic diagram of ITO-PET/perovskite film/Al (flexible) device. **g** Current−voltage (I–V) curve of ITO-PET/ $MA_2PbI_2(SCN)_2$/Al -based memory device [176]. **h** Comparison of linear replotted I–V curves for the HRS of $(PEA)_2Cs_3Pb_4I_{13}$ and $CsPbI_3$ based devices. **i** Schematic diagram showing Schottky barrier heights for $(PEA)_2Cs_3Pb_4I_{13}$ and $CsPbI_3$ [177]. **j** I − V properties of 2D/3D heterostructure perovskite-based memristor. **k** Endurance performance comparison between 3D (350 cycles) and 2D/3D heterostructure device (2,700 cycles) with fixed pulse period of 640 µs [178]

have significantly sped process optimization. Emerging solutions provide a number of interesting lines of inquiry. To anticipate crystallization behavior and design optimal spacer molecules, machine learning techniques are used [165]. In situ grazing-incidence X-ray scattering is one of the advanced characterization methods that offer previously unheard-of insights into the kinetics of film development [166]. Additionally, the advancement of universal stability methods is making it possible to compare material performance across many research groups with greater accuracy [167].

2.2 Memory Devices and Synapse

Researchers are working to reduce the power consumption in memristors to link the challenges of massive data. The

key to achieving minimal power utilization is by reducing operational current. Due to the presence of larger densities of defects, such as interstitials and vacancies in perovskite-based memristors, significant leakage current has been found, which will thus lead to extremely low power consumption for devices. Recently, LD perovskites-based memory devices with high ON/OFF current ratios [118], long-term retention [168], low operating voltages [169], and multilevel resistive switching [170] are emerging as future smart memory devices [171–173].

Ren et al. fabricated a 2D organic–inorganic hybrid memristor with low power consumption [118]. The device structure was $Au/(PEA)_2PbBr_4$/graphene where PEA represents phenethylammonium. Figure 11a shows the schematic diagram of graphene/2D perovskite/Au vertical device with structure. Filament formation is observed from Figs. 11b (initial state) and 9c(after voltage stress) by using atomic

force microscopy (AFM) images. Achieving the charge transport suppression in 2D $(PEA)_2PbBr_4$ film, a very small program current (10 pA) is enough to operate the memristor, which is much lower than previously reported memristors. Figure 11d shows the TEM image of filament formation in the device. Seo et al. fabricated 2D hybrid perovskite-based memristor in 2017. They compared the properties of these 2D perovskites-based memristors with 3D variants [174]. The device has Si/SiO$_2$/Ti/Pt/BA$_2$MA$_{n-1}$PbnI$_{3n+1}$/Ag structure where BA is butylammonium, BA$_2$PbI$_4$ (n = 1) is 2D perovskite, when n = 2,3 were quasi-2D, and MAPbI$_3$ (n = ∞) represents 3D perovskite. Quasi-2D perovskites memristors show much reduction in the set voltages and an increase in the ON/OFF current ratio from 10^2 to 10^7. This was explained based on thermal activation energy and higher Schottky barrier heights of 2D perovskite. Tian et al. [118] used 2D $(PEA)_2PbBr_4$ perovskite single crystals to fabricate graphene/ $(PEA)_2PbBr_4$/Au memory devices with as low as ≈ 0.1 pA I$_{OFF}$ and 10^2 ON/OFF current, showing the minimum energy consumption of the device. They also reported multilevel storage for several compliance currents. Lee and co-workers reported the effect of sequentially vapor-deposited BA$_2$PbBr$_4$ grain size impact on the performance of ITO/BA$_2$PbBr$_4$/Au memory cells [175]. Multiple grain sizes (180 nm, 1 μm, 30 μm) were achieved at several transformation temperatures (100, 150, and 200 °C, respectively). There is no effect of grain size on I$_{ON}$ while I$_{OFF}$ reduced from 10^{-4} to 10^{-8} A, resulting in an increase in ON/OFF current ratio from 5 to 2.4×10^3. It has been reported that low-dimensional (0D, 1D, 2D) perovskites are more stable as compared to bulk 3D perovskites and 3D perovskites can be transformed into 2D by substituting the cations or halides parts of larger groups. 2D hybrid perovskite was synthesized by substituting pseudohalide such as thiocyanate (SCN−). Lu and co-workers prepared 2D MA$_2$PbI$_2$(SCN)$_2$ and deposited by solution-processable method and achieved memristive response of the ITO/MA$_2$PbI$_2$(SCN)$_2$/Al memristors [176]. The original and schematic of flexible device is displayed in Fig. 11e, f. Sweeping the voltage between ITO and Al electrodes, binary or ternary memory switching was achieved. Ternary switching is shown in Fig. 11g.

Recently, Jang and co-workers in 2020 made Si/SiO$_2$/Ti/Pt/(PEA)$_2$Cs$_3$Pb$_4$I$_{13}$/Ag memristor based on quasi-2D (PEA)$_2$Cs$_3$Pb$_4$I$_{13}$ perovskites [177]. They achieved a higher ON/OFF current ratio of up to 10^9, which was much higher than all-inorganic CsPbI$_3$ 3D memristor. Higher activation

energy, wider bandgap, and the Schottky barrier height of quasi-2D (PEA)$_2$Cs$_3$Pb$_4$I$_{13}$ perovskite make them prominent against 3D CsPbI$_3$ perovskites. Higher ON/OFF current ratio, low I$_{OFF}$ values, and improvements in stability against moisture by preventing PEA cation degradations under ambient conditions provide a long-time response of up to 2 weeks.

As we reported earlier, the stability of 2D perovskite-based memristors is much better than 3D based memristors. Recently, in 2020, Jang et al. reported the distinguished performance in terms of stability and high ON/OFF ratio of memory devices based on (PEA)$_2$Cs$_3$Pb$_4$I$_{13}$. They achieved ON/OFF ratio as high as 10^9, which is almost three times greater than that of an ordinary CsPbI$_3$ device. The higher value of the ON/OFF ratio was explained based on reduction in high-resistance state current formation. Under ambient circumstances, they reported the ON/OFF current ratio was high till two weeks, whereas CsPbI$_3$-based devices degraded in 5 days. These achievements reveal that quasi-2D halide perovskites are more reliable as compared with 3D perovskite-based devices in resistive switching memory with higher performances and long-term stability. Comparison between I–V curves of 3D CsPbI$_3$ and quasi-2D (PEA)$_2$Cs$_3$Pb$_4$I$_{13}$ at HRS is shown in Fig. 11h. The quasi-2D-based memristor shows a much lower current in the HRS. A schematic showing Schottky barrier heights for CsPbI$_3$ and (PEA)$_2$Cs$_3$Pb$_4$I$_{13}$ is mentioned in Fig. 11i. Jung et al. fabricated 2D/3D heterostructure perovskite films by low-temperature solution process deposition and observed memristive performance with long-term endurance of about 2700 cycles, higher on/off ratio of 10^6 with 640 μs operation speed [178]. Because of its higher thermal conductivity, they found that 2D perovskite may control the Ag conductive filament's rupture. Figure 11j shows the device's I–V curve under the DC sweeping voltage (0 V → + 1 V → 0 V → − 1 V → 0 V). The endurance performance of the device is indicated in Fig. 11k. The 3D perovskite device's endurance was reported to be only 350 cycles, which is significantly shorter than the 2D/3D perovskite device's endurance (~2,700 cycles). In 2018, Kim et al. fabricated highly stable memory device based on CsPbCl$_3$ PQDs surrounded in poly(methyl methacrylate) (PMMA) [179]. They reported 2×10^4 ON/OFF current ratio and 1×10^4 s stability of the device. Recently in 2021 Lee and co-workers reported all-inorganic perovskite quantum dots based light-emitting memories and transformed to light-emitting electrochemical

cell [180]. Wang et al. in 2021 fabricated 1D perovskite-based resistive memory with ultra-low operating voltage about 0.2 V and bipolar I–V hysteresis [172].

2.3 Memory Devices-based optically driven synapses

Biological synapses play a significant role in the signal's transmission for memory, learning, and several other processes with very small power consumption. The biological synapses perform the computing and memory functions simultaneously. This makes the human brain capable of low power (100 fJ) consumers for each synaptic function. The central nervous system is made of $\approx 10^{11}$ neurons, linked by $\approx 10^{15}$ synapses to form a complete architecture for the human brain [181]. Rapidly increasing demand of fast data transfer systems as compared to conventional von Neumann architecture-based computing architecture, big data, and development of internet technologies, the significance of next-generation data computing components with minimum energy consumption by overcoming the limitations of separated main memory and central computing unit (CPU) is becoming more prominent [182]. Researchers are working to attain an alternative to traditional von Neumann architecture in which we need two different processing units for memory and information processing with the consumption of high power to perform neuromorphic computation [183]. Recently, synaptic devices are considered to be an alternative to classical von Neumann architecture as they can perform complex signal processing including decision-making, image classification, and involve the use of artificial neural networks for pattern recognition [184, 185]. Through the removal of the von Neumann architecture's bottleneck, neuromorphic computing simulates the function of biological synapses in information processing. In neuromorphic operating systems, mimicking synapse processing using these devices is crucial. Researchers have driven synaptic devices by electrical and optical signals to encourage the modeling of various synaptic processes. These devices can be classified into electrically, photoelectrically, and optically stimulated synaptic devices depending on the activation of electrical and optical signals, respectively [186].

Many studies are focusing on the device architectures and materials properties for the use in synaptic devices, but the van der Waals (vdW) heterostructures of 2D materials are among the best of researcher's choice due to their unique

mimicking capacity in synaptic plasticity for neuromorphic computing, which is based on the memristive hardware neural networks [187–189]. Different structural and compositional arrangements of perovskite halides make them versatile in electronic, physical, and chemical properties. All-inorganic, as well as organic–inorganic mixed perovskite halides, are extensively utilized for the fabrication of synaptic and memory devices [190, 191]. Under constant irradiation of light, the defects migration in the perovskite layer generate a higher hysteresis in IV response, resulting in better memory performances and artificial synapse devices applications for neuromorphic computing. Thus, defects present in the perovskite layer due to halide vacancies perform an important job in the memory functionalities and characteristics of the synaptic devices. In recent years, the 2D perovskite-based RRAM and the flash memory systems were used to construct the advanced artificial synaptic devices including two-terminal memristive synapses and three-terminal FET-based synapses to mimic the biological synapses. Simultaneously, the perovskites are more promising candidates for utilization in the artificial synapse with the capabilities of concurrent processing and learning due to their ionotropic effects as compared to other semiconductor materials. The movement of halide ions between the layers plays an important role in the conductance of 2D halide perovskite-based devices. This phenomenon is very similar to the synaptic conductance mechanism through intracellular Ca^{2+}, Na^+, and K^+ ions in neurons. Considering the ionotropic effects and better phototunable properties in halide perovskites-based memory devices, the electric bias and photonic illumination are used as external stimuli to simulate several synaptic operations including short-term potentiation (STP) and depression (STD), long-term potentiation (LTP), and depression (LTD), paired-pulse depression (PPD) and facilitation (PPF), spike time-dependent plasticity (STDP), and spike rate-dependent plasticity (SRDP).

In 2019, Sun and co-workers made a photoelectrically stimulated synapse with Pb-free 2D perovskite-based $((PEA)_2SnI_4)$ [192]. They discovered photocurrent activation in a neuron-like process under light illuminations and possess synaptic capabilities such as STP and LTP. They successfully modulated the synaptic connectivity by exposure, irradiance, and wavelength of light spikes. The ternary structure of reported 2D perovskite $(PEA)_2SnI_4$ possesses varied photoelectric properties under different compositions. They proposed the great potential of $(PEA)_2SnI_4$ for
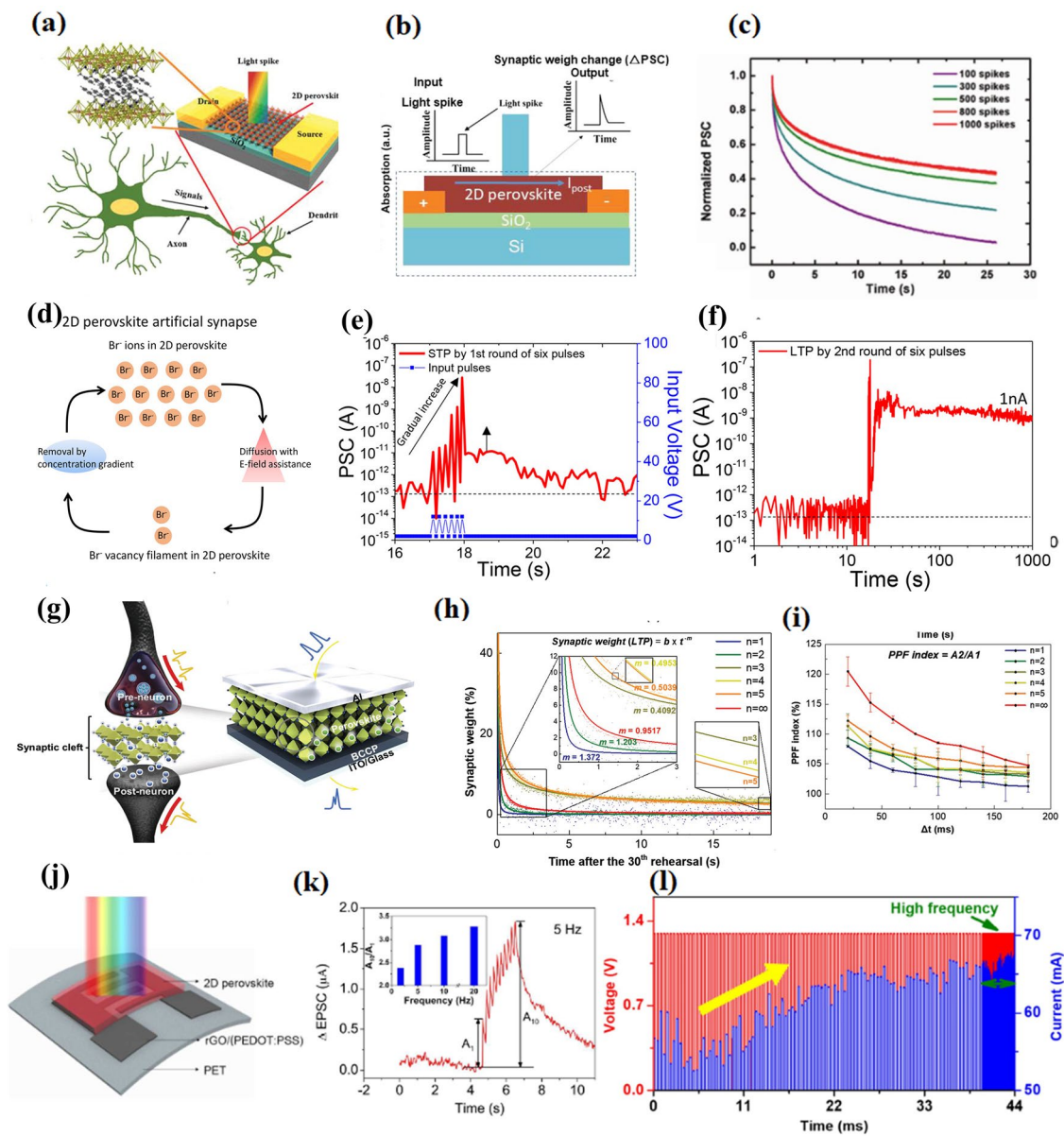
Fig. 12 a Structural schematic of the device and biological synapses with axons to dendrites. Insects show crystal structure of 2D layered perovskite. **b** Side view schematic of device with input light spikes and the output PSC in the insets as an example. **c** Normalized PSC decay under 100 to 1000 light spikes [192]. **d** Schematic of Br ion migration in 2D perovskite-based artificial synapse. **e** STP at first round of six pulses. **f** LTP at the second round of six pulses with the increase in current level to 1 nA with long-term (1000 s) retention [118]. **g** Schematic diagram showing the artificial synapse and perovskite-based artificial synapses device geometry. **h** Decay curves for the current after the 30th rehearsal of perovskite synapses. **i** PPF index under several applied pulses with multiple time intervals $20 \leq \Delta t \leq 180$ ms [194]. **j** Structural schematic for a $(PEA)_2SnI_4$ flexible photoconductor. **k** Change in EPSC under 10 light pulses with time intervals of 200 ms [195]. **l** Neuromorphic behavior at gradual current change under continuous pulse voltage [196]

future multifunctional artificial neuromorphic systems. 3D schematic diagram of 2D perovskite-based synaptic device is shown in Fig. 12a with a crystal structure of $(PEA)_2SnI_4$ (in the top left corner of inset Fig. 12a). The cross-sectional view of as-fabricated devices with artificial

synaptic functionalities including examples of the input light spikes and the output post-synapses current (insets) is demonstrated in Fig. 12b. Figure 12c shows the normalized post-synapse currents after several light stimulations with improved memory response by increasing the number

of light spikes. Device conductivity is typically regarded as synaptic weight in artificial synaptic devices [193]. Tian et al. in 2017 reported 2D RP phase hybrid $PbBr_2$ perovskite single crystals with mixed electrical and ionic transport for low-power consumption nanodevice applications and simple fabrication process [118]. They mentioned the ionic transport due to the bromide ions migration and 20-nm-diameter filaments were observed. They achieved extremely low operating current resistive memories about 10 pA, which is smaller than conventional materials. Figure 12d shows ionic transport in 2D Br-based artificial synapse with Ca^{2+} ions release and recycling process.

The device performance in terms of STP with a constant increase in peak current is shown in Fig. 12e. Figure 12f illustrates the six pulses in the second round used to generate potentiation in the short to long term at a current of about 1 nA. This result can be attributed to filament formation under constant pulses. The device's stability over the long term is reported as more than 1,000 s (Fig. 12f). Recently, in 2019 Lee and co-workers reported dimensionality-dependent plasticity in artificial synapses made of halide perovskites and used it for neuromorphic computing [194]. They reported approximately ≈ 0.7 fJ energy consumption per synaptic event that is very small as compared with previously reported synapses and competitive to that of biological synapses in which energy consumption is considered to be about 1–10 fJ per synaptic event. Figure 12g shows the schematic illustration of artificial synapses (left side) and device structure (right side) of a two-terminal device with ITO (bottom electrode)/ buffer-capped conducting polymer (BCCP)/perovskite layer/Al (top electrode). Figure 12h illustrates how they used repeated stimuli to produce the STP–LTP transition in the reported synapses. After 30, the loss of memory retention fitted a power function $y = b \times t^{-m}$, where m is the power function rate, t is the time duration, b is the scaling fit constant, and y is the synaptic weight [197]. The retention curve gradually declines as m drops, meaning that memory length rises, as seen in Fig. 12h inset. Another important perimeter of a synapse is paired-pulse facilitation (PPF), which is a type of STP. In the PPF, the synaptic strength progressively increases with the applied paired pulse at a small interval Δt. The increase in PPF under two consecutive stimuli of the device is shown in Fig. 12i. Qian and co-workers reported for the first time the lead-free 2D perovskite-based flexible photoconductor and synaptic device by simple solution process method [195]. They claim the improved

stability and high reproducibility of the devices at 30 mol% addition of SnF_2 into the perovskite. Under 470 nm light, the flexible photoconductors' photoresponsivity was 16 A W^{-1} and their detectivity was 1.92×10^{11} Jonesrecorded and claimed to be higher than most of the similar devices. Figure 12j shows the schematic of structural diagram for $(PEA)_2SnI_4$ flexible photoconductor with PET as flexible substrate and perovskite active material under irradiation of light. The dynamic synaptic behavior of the device is mentioned in Fig. 12k. The highest value of EPSC reached by one pulse was greater than the preceding one when ten light pulses were continuously irradiated at 200-ms intervals. The EPSC drops and reaches the starting current when the light is off. This is known as mimicking a biological excitatory synapse's STP behavior.

Kim and co-workers attain multi-leveled resistive switching behavior without compliance in a fully transparent 2D perovskite and utilized it in neuromorphic computing [196]. They reported multileveled resistive switching with pulsed voltage tuning. Under applied voltage pulses, current across the device continuously flipped and reached four different values, all of which remained stable for a long period, confirming multimode RS. Possessing the ability to use a pulse input signal to regulate the device current, the analog memory device can achieve synaptic functionality. They explored the transparent 2D perovskite-based device's progressive current change characteristic in the context of pulse cycling. Normally neuron combines with the input signals to attain the threshold and produce the spike signal. Figure 12l shows the device response under 0 to $+1.3$ V DC voltages pulses.

2.4 Phototransistors and Synapse

Field-effects transistors (FETs) are the most prominent candidate to build novel and modern electronic devices for the future electronic industry. FETs having several superior properties like minimum power consumption, small noise factors, high input resistance, and ease of integration make them superior among other electronic devices. Surprisingly increasing demands of FETs with higher efficiencies and better integration densities are attaining the interest of researchers for developing modern optoelectronic devices which were not compensated by conventional metal oxide semiconductor-based FETs. The performance and efficiency of FETs mainly depend

upon the selection of channels. There are several channel materials reported with improved performances, and higher responsivities but 2D perovskite-based FETs possess significantly high performances and efficiencies with extreme resistance against the short channel effect [198]. The most common methodologies to improve the working of FETs are based on the optimization of interface morphology [199], tuning of Schottky barrier height [200], and optimizing integration density by scaling down the FET into the integrated chip [201]. The density effect can be defended by the Moore's law statement, in which he precepted that quantity of transistors will be doubled on the microchip every two years. He also proposed that the speed and capability of computers will be increased every couple of years with low cost and ease of operation.

There is extensive research in LD perovskite-based photovoltaics and light-emitting diodes but still plenty of room available for FETs and phototransistors (PTs). The exceptional charge transport properties, optoelectronic properties, and cost-effective synthesis make perovskites feasible for practical optoelectronic device applications [202, 203]. The simplest exciting example is LD perovskite-based low-cost and highly sensitive photodetectors. Normally perovskite photodetectors are classified into two main types, photodiodes and photoconductors [204]. Photodiodes with solar cell-like architecture have fast response speeds, low dark currents, and high-frequency operation ranges with low noise. Photo conductance of perovskite-based photoconductors can be modulated under incident light illumination. Phototransistor is a bipolar transistor that allows the light to illuminate its base–collector junction and generate photocurrent, flowing between emitter and collector. PTs are a special type of photoconductor with a high gain due to inherent amplification functionality by the transistors [205]. Similar to photoconductors and photodiodes, the phototransistor responds to the incident light illumination and creates excitons as well as trions in perovskite layer. When there is an external electric field present, these photoelectrons dissociate into free charges, which are gathered as photocurrents at electrodes. Another advantage of PTs over conventional two-terminal photodetectors is the modulation of input signal weak current through the gate–source voltage, permitting an improved and better sensitivity, which is not possible by two-terminal photodetectors. Like FETs, the performance of PTs is also described in terms of detectivity

(D*), responsivity (R), t_{rise} and t_{decay} quantifying their interaction with light. The photoresponsivity is defined by:

$$R = \frac{I_{light} - I_{dark}}{P \times A}$$

Here I_{light} and I_{dark} represent the current under illumination, current in dark, respectively. P represents the incident light's intensity, and A is the device's active region. Similarly, D*, the detectivity, is computed by:

$$D^* = \frac{R \times \sqrt{A}}{\sqrt{2 \times I_{dark} \times q}}$$

Here R represents responsivity, A is the device's active area, q denotes the elementary charge. Time response of PTs is computed by t_{rise} and t_{decay}, which is determined by the time it takes for the current to increase from 10 to 90% of its maximum value and drops from 90 to 10% of its highest value.

Chen al in 2016 fabricated for the first time hybrid 2D perovskite-based phototransistor. They used PEA_2SnI_4 thin films as 2D perovskite and achieved the responsivities about $R = 1.9 \times 10^4$ A W^{-1} below 447 nm illumination light owning power density 5×10^{-3} mW cm^{-2} and $t_{rise} = 0.45$ s [206]. Recently, Wu and co-workers introduced an innovative solid–solid conversion process that transforms unstable 3D perovskite films into highly crystalline, well-oriented 2D configurations via amine steam treatment, significantly enhancing material stability. The resulting 2D films enable self-powered photodetectors with narrowband light sensing, offering a promising route for the advanced manufacturing of high-performance passive sensors [207]. Wang et al. used the same $(PEA)_2SnI_4$ perovskite material to fabricate PTs with vinylidene fluoride-trifluoroethylene as gate dielectric and attained the variation in the dielectric polarization with responsivity $R = 14.57$ A W^{-1}, D* $= 1.74 \times 10^{12}$ Jones, and a t_{rise} (t_{decay}) of 50 ms (1.5 s) under 470 nm illumination having a light power density of 2.1×10^{-3} mW cm^{-2} [208]. Later on, Zhu et al. enhanced the performance of $(PEA)_2SnI_4$ PTs by improving perovskite microstructure by applying solvent engineering and reported with a light power density of 0.3 μ mW cm^{-2} and $R = 1.6 \times 10^5$ A W^{-1} and D* $= 3.2 \times 10^{17}$ Jones under 532 nm light, which is better than Si or InGaAs-based photodiodes [209]. 2D perovskite-based PTs with high gain and better response to the incident light illumination are used in neuromorphic visual systems. These PTs recognize
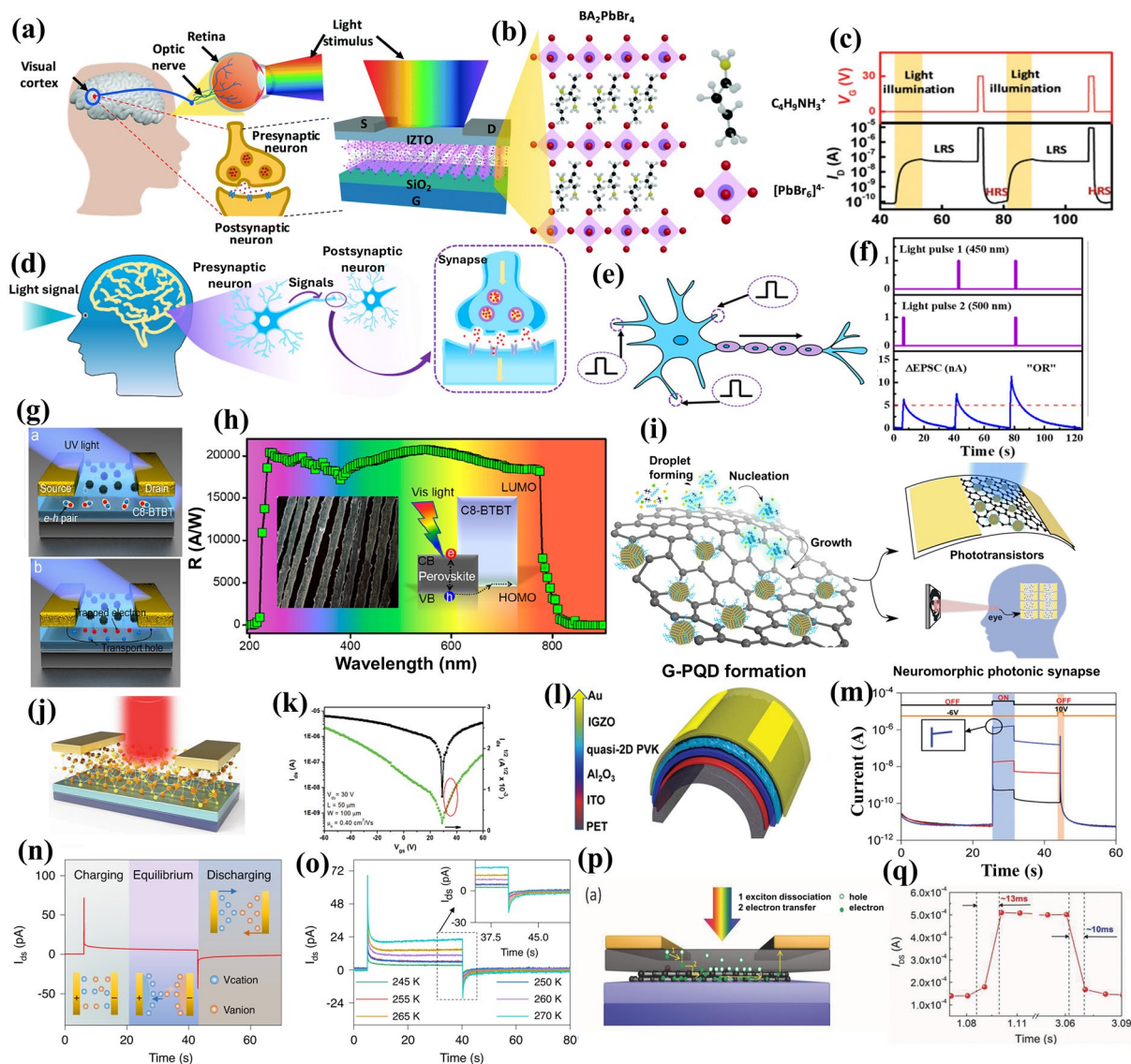
Fig. 13 Phototransistors and synapse. **a** Schematic diagram of the human visual system and 2D perovskite-based optical synapse. **b** Structural diagram of BA$_2$PbBr$_4$ (where, Pb, Br, C, N, H, are represented by blue, red, black, yellow, gray, and blue colors respectively. **c** Variation in device resistance under different optical spikes [210]. **d** Schematic image of a human visual system with signal transmission between pre- and post-neurons. The right size shows the schematic of the CsPbBr$_3$ QDs-based device. **e** Schematic of input and out pulse integration in a neuron. **f** Excitatory post-synaptic current curves at different input light pulses [191]. **g** Schematic of phototransistor device operation under UV illumination. **h** Photoresponsivity of the device against light wavelength, with the inset showing optically driven charge movement mechanism and another inset image of optical microscope showing C8-BTBT single-crystal array embedded with CH$_3$NH$_3$PbI$_3$ nanoparticles [211]. **i** Schematic of the growth process of graphene perovskite superstructure (left side), device architecture (right side), and its applications in the neuromorphic photonic synapse [212]. **j** Scheme of the FET structure under light illumination. **k** Saturate transfer curves of the device with 30 V V$_{ds}$ [213]. **l** Schematic of the flexible quasi-2D PVK/IGZO based phototransistor. **m** Writing and erasing processes of the device under infrared pulse (1064 nm). Inset showing a sharp increase in source–drain current when the gate voltage pulse is applied. The blue-shaded region represents the laser pulse [214]. **n** Schematic showing charging, equilibrium, and discharging process for Au/2D perovskite/Au device and **o** its temporal response curves under dark [214]. **p** Schematic of photogating effect in NGQDs–perovskite/mrGO phototransistor. **q** Photoswitching under light and dark at 2 s intervals with rising/fall time of 13/10 ms [215]

as well as memorize the optical information which is important for optically driven artificial synapses. This optically driven synapse responds well to optical signals with higher

gain and a much lower level of noise. Organic–inorganic hybrid halide perovskites are widely used as optically modulated synapses with a long charge carrier lifetime and high

absorption coefficient. The main hurdle in these hybrid perovskites-based PTs is the difficulty to store the optical information because of rapid recombination of photo-generated carriers after the excitation of illumination.

Recently, Lee and co-workers in 2021 overcome the carriers recombination issue by using indium zinc tin oxide (IZTO) in combination with 2D-layered metal halide perovskite to fabricate broadband optoelectronic synaptic transistors with improved performance and higher optical memory [210]. Figure 13a shows the schematic process of humans using the retina to perceive optical information. Nerve cells inside the retina initiate the transformation of optical data into neural signals. The optic nerve subsequently carries these neural signals to the brain's visual cortex. The whole process needs a huge network of neurons and synapses to process and memorize data. Figure 13a also shows the comparison of fabricated phototransistor devices consisting of 2D layered BA_2PbBr_4 and IZTO with the human visual system. Figure 13b shows the schematic structure of BA_2PbBr_4 containing octahedra $[PbBr_6]^{4-}$ (inorganic layer) sandwiched between two organic $[C_4H_9NH_3]^+$ layers where Pb, Br, C, N, H are represented by blue, red, black, yellow, gray, and blue colors, respectively. The device showed a uniform change in the resistance by transforming between high and low resistance stares under repeated applied optical pulses as shown in Fig. 13c.

Previously in 2020, Hao et al. fabricated a photonic synaptic transistor by $CsPbBr_3$ perovskite quantum dots and organic semiconductors for the artificial visual system [191]. They used a simple solution-processable method to synthesize the material. They reported that the fabricated device possesses basic functionalities, including pair-pulse facilitation, the transformation between short-term and long-term memory, excitatory post-synaptic current, and "learning experience" responses. High photosensitive perovskite material combined with higher conductivity organic semiconductor showed a remarkable response at low voltage of -0.2 V. They reported the synaptic responses at an extremely low operation voltage of -0.0005 V. Schematic of the human visual system compared with the fabricated device is represented in Fig. 13d. Figure 13e displays the schematic diagram of dendrite integration in a neuron. Multiple presynaptic inputs from various dendritic sites can be combined by a neuron to elicit dynamic logic in the post-synaptic neuron. The OR logic operation is demonstrated in Fig. 13f with multiple inputs by utilizing one or two input light pulses and

transforming them into a larger threshold value. Lee and co-workers applied one-step solution-processable synthesis approach to fabricate dual-band phototransistors with higher performance from hybrid perovskite as well as from organic crystal arrays [211]. They reported dual-band phototransistors with responsivity as maximum as 1.72×10^4 A W^{-1} in region of $252 - 780$ nm, the absorption covering the entire $UV - vis$ range and utilized as high-security communication. Figure 13g(a) shows the device's structural diagram and working mechanism. $CH_3NH_3PbI_3$ hybrid perovskite nanoparticles are dispersed at the C8-BTBT surface and electrons holes pair formed with in C8-BTBT when UV falls on the layer. Holes can be controlled in a very small region near BCB/C8BTBT interface by means of an applied electric field, while electrons were trapped within C8-BTBT with strong electron trapping capability; the schematic of the holes restriction and electrons trapping is shown in Fig. 13g(b). Photoresponse of the device against light wavelength at fixed light intensity is shown in Fig. 13h. The inset shows the optically driven charge movement mechanism from the hybrid perovskite layer to C8-BTBT. Another inset image of optical microscope shows C8-BTBT single-crystal array embedded with $CH_3NH_3PbI_3$ nanoparticles. Thomas et al. used organic–inorganic halide perovskite quantum dots combined with graphene to form a superstructure providing generating and transporting charges efficiently on a single platform [212]. Perovskite quantum dots were directly grown on the active sites of graphene surface to form a superstructure. The schematic of the growth process started from droplet forming, nucleation, and growth is shown in Fig. 13i (left side). They employed these superstructures to make ultrathin, ultra-sensitive phototransistors with photonic synaptic activity and neuromorphic computing, which they demonstrated through machine learning and facial recognition. A structural schematic diagram of the fabricated phototransistor and proposed application as neuromorphic photonic synapse is shown in Fig. 13i (right side).

Guo and co-workers fabricated ambipolar phototransistors based on $CsPbBr_3$ all-inorganic perovskite microplates [213]. They reported room temperature anomalous ambipolar transport characteristics. Furthermore, they mentioned that hole mobility is light dependent, but the electron mobility is independent of incident light illumination and remains the same under various light incidences. Figure 13j shows the schematic of the fabricated FET structure under light illumination. The saturated region of $CsPbBr_3$ FETs exhibits

the n-type transfer curve in Fig. 13k, electron mobility of 0.40 cm^2 V^{-1} s^{-1} under 30 V Vds. Phototransistors and photo-induced memory operations were combinedly studied by Liao and co-workers [214]. They employed a heterostructure of indium gallium zinc oxide (IGZO) with quasi-2D perovskite to fabricate highly sensitive flexible phototransistors for broadband photodetection. They reported the photoresponsivity of the device $> 10^5$ A^{-1} W at 457 nm, specific detectivity 5.1×10^{16} Jones, and 457–1064 nm broadband photoresponse. The schematic of flexible quasi-2D perovskite/IGZO heterostructure-based phototransistor with bottom-gate structure is shown in Fig. 13l. Apart from photodetection, they also used this quasi-2D perovskite/IGZO heterostructure for photonic memory operations. The photoresponse of memory in terms of writing/programming and photocurrent stability is shown in Fig. 13m and inset of Fig. 13m, respectively. Jiang et al. fabricated another heterostructure with photoactive dielectric behavior consisting of Al$_2$O$_3$ and 2D perovskite and used them for high-performance phototransistors [214]. 2D perovskite with better availability of photogenerated carrier results in the higher photoresponsivity of $> 10^8$ and 10^6 A W^{-1} at 457 and 1064 nm, respectively. At the same time, Al$_2$O$_3$ facilitates the neutralization of charge trapping and ionic migration of perovskites ensuing better stability under bias voltages. A brief schematic of the charging, equilibrium, and discharging process with the movement of electrons/holes and ionic vacancies under external bias for the Au/2D perovskite/Au device is presented in Fig. 13n. The quick flow of electrons/holes along the external electric field causes a sharp increase in instant current under external bias. At the same time, the ionic vacancies accumulate at the interfaces of 2D perovskite/Au and oppose the external electric filed by forming an internal electric field, explained in Fig. 13n. Later on, the ion-induced electric field reduced to attain equilibrium condition. After removal of bias, the backward movement of ionic vacancies forms a negative current. Thermal response of devices under dark is shown in Fig. 13o.

There are several reports about low-dimensional perovskite combined with other materials to form a heterostructure and utilized as different high-performance phototransistors. Another strategy of composites formation by doping nitrogen into graphene quantum dots (NGQDs)–perovskite composite was used by Liu et al. to fabricate phototransistor with broadband detection (365 to 940 nm range), high photoresponsivity (1.92×10^4 A^{-1} W), and fast response

to light on–off (≈ 10 m) [215]. The schematic of photogating with incident light and charges movement between the hybrid channel layers is shown in Fig. 13p. Green circles indicate electrons, whereas white circles indicate holes. The extreme responsive behavior with magnified photocurrent curve under light illumination (on–off) and switching interval of 2 s is displayed in Fig. 13q; rise and fall time is 13 and 10 ms, respectively, showing the highest photoresponse rate among other graphene- or rGO-based photodetectors.

2.5 Photodetectors

Photodetectors (PDs) are employed to transform optical signals into electrical signals. They have a wide range of applications in different areas including image sensing, optical communications, sensing applications, military applications, environmental monitoring diagnostic tools, digital radiography, and nuclear medicine, etc. The efficiency of PDs mainly relies on fast response speed, high detectivity (D*), high responsivity (R), and on/off ratio. To fabricate the higher efficiency PD, the active layers should have higher carrier mobility, absorption coefficient, better charge carrier collection, and low trap-state density. Nowadays, InGaAs-, Si-, and GaN-based photodetectors are available for commercial use. These available photodetectors have the drawback of their high manufacturing cost and low efficiency.

Researchers are striving to develop low-cost, high-efficiency photodetectors that are compatible with the CMOS technology. For decades, CMOS technologies have been employed to build mature, low-cost, and reliable integration solutions. Photodiodes and phototransistors are widely used for photodetectors. They are divided into further types like PN photodiode, PIN photodiode, and avalanche photodiode. CMOS technology has been used to fabricate PIN photodiode, avalanche photodiode, phototransistor, and a photodiode for the single-chip application. PN photodiode is very commonly used for photodetection and is very easily implemented into the standard CMOS technology. Most PDs in the UV–visible to NIR range are made up of crystalline inorganic semiconductors and their heterojunctions [216]. These semiconductors-based PDs lack in terms of complicated structures and complex fabrication requirements. Commonly used high-cost and higher temperature fabrication methods are metal–organic chemical vapor deposition (MOCVD) and molecular beam epitaxy (MBE). Meanwhile,

the rigidity of the materials bounds them for flexible and large-area PDs. PDs based on solution-processed fabrication techniques are getting more attention for next-generation photosensors [217, 218]. Low-dimensional metal halide perovskites (LDMHPs) are capable candidates for optoelectronic device applications with simple solution deposition methods, weakly bound excitons, high absorption coefficient, long carrier lifetime (> 1 ms), and tunable bandgap (1.48 and 2.23 eV) [48, 83]. $MAPbI_3$ and $MAPbBr_3$ have Urbach energies of 15 and 13 meV, respectively, which is comparable to III–V materials (e.g., Urbach energy of GaAs is 7 meV), and LDMHPs have a significantly greater absorption coefficient than crystalline Si [219]. This small value of Urbach energy refers to the high crystallinity and minimal level of structural irregularity of LDMHP nanocrystals. At the same time, the complete exponential optical absorption edge reveals the absence of deep states within the bandgap. All these parameters make LDMHPs suitable for PDs applications for their higher optoelectronic performance [42, 220]. On a variety of substrates, 2D perovskites with single-crystalline structure can be synthesized. These single-crystalline perovskites possess better surface morphology, highly efficient photoluminescence, lower recombination rate, fewer grain boundaries, lower traps, extended carrier lifespans, and improved mechanical qualities for printed and flexible devices [221–223]. At the same time, these 2D single-crystalline perovskite materials show suppressed ion migration, better mechanical stability, phase stability, and environmental stability of final devices than polycrystalline ones. So, tremendous performances, better stabilities, and flexibility of these 2D Perovskites can produce various PDs that have not yet been noticed in polycrystalline LDMHPs. 2D MHPs are classified into layered and nonlayered MHPs. From three-dimensional MHP structures, nonlayered are directly flattened down to atomically thin films. Unlike 3D perovskites, 2D layered perovskites do not have a size restriction on the interlayer cations. Because of this structural characteristic, organic cations can reach the interlayer gap between inorganic layers. 2D layered MHPs possess better in-plane anisotropic geometry effective light absorption and quicker in-plane transmission of charge carriers due to minimum hopping barriers. 2D layered MHPs are suitable for wavelength selective narrow-band PDs, which can be widely used in machine vision, biomedical sensing, XR-imaging, and military defense systems [204, 224]. 2D layered MHPs able are able to recognize the

circularly polarized light (CPL) which has potential in magnetic memory devices, optical report mechanism, display technologies, telecommunication, and chiral catalysis. All these improvements are attracting the researchers' toward LDMHPs for PD applications. 2D perovskites with better environmental stability and tremendous optoelectronic properties are emerging as an alternative against 3D bulk perovskites. 2D perovskite-based PDs with simple and low-cost synthesis, high efficiency, wide-spectrum-range detection are significantly dominating in the optoelectronic market. Singe-crystal-based 2D perovskite PDs are more efficient in photoresponsivity as compared to film-based perovskite photodetectors due to low trap density and better stability. There are different synthesis methods for single-crystalline perovskite materials, e.g., CVD on mice and $SrTiO_3$ substrate and solution-processable methods. Solution-processable methods are more prominent for the fabrication of single-crystalline structure at ambient conditions.

In 2016, Tan et al. synthesize $(C_4H_9NH_3)_2PbBr_4$ crystals with several to tens of micrometers domain sizes by room temperature simple solution-processable technique on SiO_2/Si substrates and used them to fabricate photodetectors [22]. Octahedral $PbBr_6$ is well connected by corner-sharing Br^- atoms to form a 2D perovskite layer in *bc*-plane. Schematic structural diagram of the fabricated device with detailed SEM image showing 2D perovskite layered pattern and graphene electrodes is shown in Fig. 14a, b. The 2D perovskite crystal under graphene functions as a light-sensitive substance and the graphene electrodes are around 100 nm in length. Figure 14c shows the photoswitching response of the device at approximately 10 on/off current ratios at a very small bias voltage (0.5 V).

Development of nontoxic and stable 2D perovskite material with a wide bandgap is a challenge. Fang and co-workers created 2D all-inorganic perovskite $Sr_2Nb_3O_{10}$ (SNO)-based nanosheets with 1.8 nm thicknesses via liquid exfoliation, and they reported UV PDs based on these SNO few-layer sheets for the first time [225]. These PDs exhibit higher performance in terms of better UV detection with 1.4×10^{14} Jones at 270 nm detectivity, $5.6 \times 10^2\%$ outstanding external quantum efficiency, quick response time ($t_{rise} \approx 0.4$ ms, $t_{decay} \approx 40$ ms), and narrowband responsivity = 1214 A W^{-1}. All these characteristics are higher than any individual reported 2D sheet-based UV PDs. Figure 14d displays an optical view of a flexible device on a PET substrate. Figure 14e represents the structural diagram of SNO sheet-based phototransistors
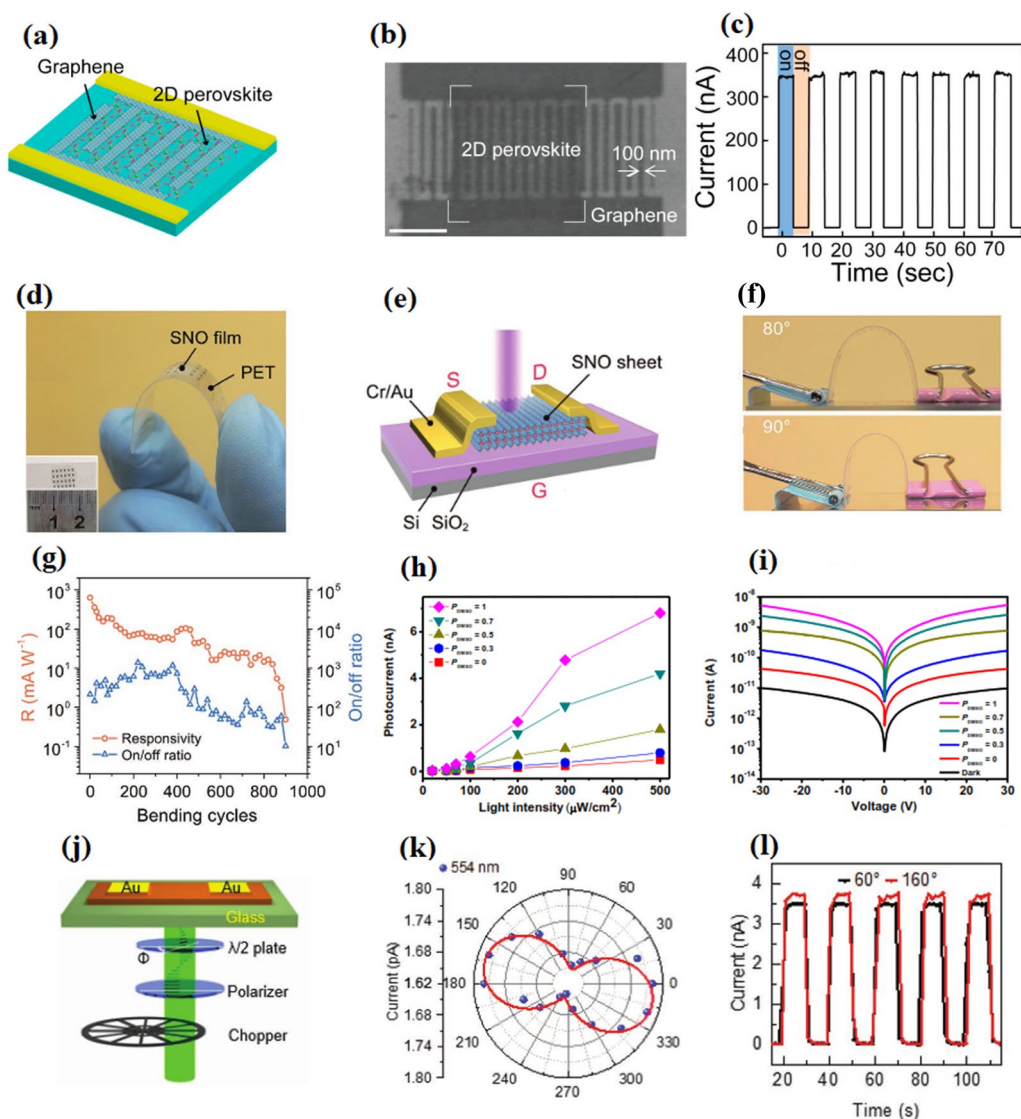
Fig. 14 a Structural schematic of the fabricated device. **b** SEM showing 2D perovskite and Graphene of the fabricated device at 1 µm scale bar. **c** Current–time response of the device with a 470-nm defocused laser with 1 mm spot size, at a 0.5 V, and 10 µW bias voltage and power, respectively [22]. **d** Optical image of a flexible device on PET substrate. **e** Structural schematic of SNO sheet-based phototransistors with source, drain, and gate voltages. **f** Mechanical stability in terms of bending test at 80° and 90° degree bending angles. **g** Flexibility in terms of R_λ variation and ON/OFF ratio at several bending cycles [225]. **h** Photoresponse of the PD with several pure DMSO concentrations under 0–500 µW cm.$^{-2}$ light intensities range [226]. **i** I–V response of the PD with several pure DMSO concentrations in darkness with semilogarithmic scale. **j** Schematic of device architecture and measurement setup configuration. **k** Graphs for photocurrent against polarization angle. **l** Device showing optical switch characteristics under 560 nm monochromatic light [227]

on Si/SiO$_2$ substrates with incident light from upside and source, drain, and gate terminals. The flexible device's mechanical stability on a PET substrate as it is fabricated is shown in Fig. 14f at 80° and 90° degree bending angles. Bending test of flexible PD shows that PD response remains stable with Ip remaining invariant up to 80° bending angle. Figure 14g shows a sharp decline in responsivity and on/off ratio in the first 100 cycles and then constant variation with increasing bending cycles.

Grain boundaries have an important role in photodetector performance by trapping charge carriers and obstructing charge transit in perovskites. High-performance PDs are fabricated by controlling the grain boundaries of perovskite film. Lee et al. synthesized large-grained
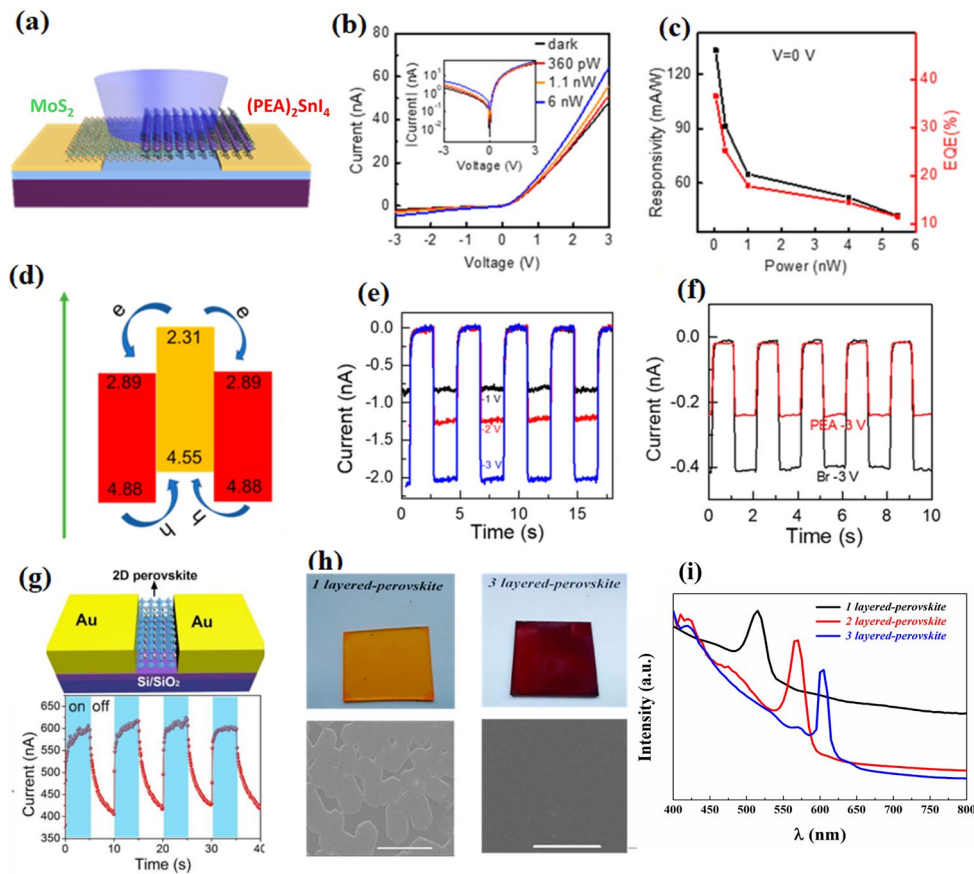
Fig. 15 **a** Structural schematic of fabricated PD. **b** I–T plot in dark and under a 451 nm light. Inset showing logarithmic scale plots and **c** its zero bias responsivity and EQE plot [227]. **d** Band diagram of $(BA)_2PbI_4/(BA)_2MAPb_2I_7$. **e** Optical switching characteristics of the heterostructural photodetector under -1 to -3 V applied bias and illuminated by 540 nm light with 45 mW/cm^2 power density. **f** Optical switching characteristics of the $(BA)_2PbBr_4/(BA)_2MAPb_2Br_7$ and $(PEA)_2PbI_4/(PEA)_2MAPb_2I_7$ device under device at -3 V bias voltage and under the 410 nm light (24 mW/cm) illumination and 540 nm (46 mW cm^{-2} 2) illumination, respectively [228]. **g** Structural schematic of fabricated (PEA)2SnI4 device (top image) and its I–T plot under 3 V bias voltage, 195.8 μW cm.$^{-2}$ at 470 nm light illumination and interval of 5 s. **h** Optical images showing orange and brown colors for 1 and 3 layers-perovskite, respectively. Bottom images showing SEM images with different film morphologies for 1 and 3 layers perovskite at 5 μm scale. **i** UV–vis spectra for layer-structured perovskite materials [229]

and highly crystalline films of 2D RP perovskites $(C_4H_9NH_3)_2(CH_3NH_3)Pb_2I_7$ by hot casting method to fabricate high-performance PDs [226]. They investigated how grain sizes and boundaries affected the performance of PDs. The concentration of DMSO and DMF is essential for film formation and grain boundaries of 2D RP perovskite thin film. Lee and fellows fabricated PDs based on several concentrations of pure DMSO and plotted the photoresponse of the PD under 0–500 μW/cm^2 light intensities range as shown in Fig. 14h. PDs I–V characteristics depending on pure DMSO = 0, 0.3, 0.5, 0.7, and 1 under a light intensity of 300 μW cm^{-2} at 460 nm wavelength and in darkness semilogarithmic scale are shown in Fig. 14i.

Li and co-workers fabricated another single-crystal 2D perovskite-based PDs, to polarization of light [227]. Previously, polarizers were combined with high cost filters to make polarization-sensitive narrowband PDs. To minimize the cost and make a simpler optical system, these single-crystal 2D perovskite-based polarization-sensitive narrowband PDs without any further sophisticated optical components were fabricated. Figure 14j shows a simple diagram of device architecture and design of the measuring setup with the polarizer on top and chopper at the bottom. It was reported that the linear dichroic ratio was 1.56 at 552 nm at an incident angle of 45° and 20 nm (full width at half maximum), that the maximum on–off ratio

could reach 10^3, that the external quantum efficiency was high at 120%, and that the peak specific detectivity was 1.23×10^{10} Jones under normal illumination. Using scotch tape, the crystal plates were first exfoliated to create new surfaces that would make good contact with the electrodes. The device's two typical optical switch characteristics are displayed in Fig. 14k under monochromatic light at 560 nm at two polarization angles with a bias voltage of -5 V. Photoresponse anisotropy of $(iso-BA)_2PbI_4$ single-crystal narrowband PD has been confirmed by observing a larger photocurrent for 160° than that of 60° polarization. Furthermore, as seen in Fig. 14l, the photocurrent against polarization angle response in two-lobed morphologies of the polarization-dependent photocurrent confirmed the photoresponse anisotropy.

Researchers are working to develop the stable, wide-range, and harmless 2D perovskite and their heterostructure-based PDs. n-type few-layer MoS_2 and p-type 2-dimensional perovskite $(PEA)_2SnI_4$ heterostructures based on PD were fabricated for the first time by Li and co-workers [227]. They were able to perform light sensing over the visible and near-infrared wavelength ranges, and a tunable photoresponse peak. Figure 15a presents the diagram of the manufactured device with MoS_2 and perovskite layers with incident light from the top side. $I-V$ responses of the device in various light intensities and in the dark are shown in Fig. 15b. Light with 451 nm illumination and various powers intensities reflects a clear current rectification behavior with a rectification ratio of ~15, due to the exceptional diode features in $(PEA)_2SnI_4/MoS_2$ heterojunction. The rise of photogenerated carriers is revealed by increasing forward and reverse current by increasing light power. Logarithmic plots of I–V responses are plotted in the inset of Fig. 15b. Responsivity and EQE of the graphene/$(PEA)_2SnI_4/MoS_2$/graphene device gradually drop by increasing incident power of the 451 nm light as shown in Fig. 15c. They reported EQE of 38.2% and the maximum responsivity of 121 mA W^{-1} were observed under 451 nm illumination with 36 pW of power.

Continuing the research on 2D perovskite heterostructures, Xiong et al. fabricated highly narrow dual-band PD based on centimeter-sized 2D perovskite heterostructures. They used the solution-processable synthesis method for $(C_4H_9NH_3)_2PbI_4/(C_4H_9NH_3)_2(CH_3NH_3)Pb_2I_7$ heterostructures having better crystalline quality, controllable thickness, sizes, higher phase purity, tunable junction depth, and increased stability for thin dual-band photodetectors. They reported low dark current (about $10-12$ A) and a very narrow dual-band spectral response, with a full width at half maximum of 20 and 34 nm at 540 and 610 nm, respectively. This improved efficiency is linked with the high crystalline purity of heterostructures. Figure 15d displays the manufactured heterostructures' band diagram, which is a type-II structure. Optical characteristics in terms of current–time plots at -1, -2, and -3 V (negative voltages) under 540 nm light illumination are shown in Fig. 15e, which shows the constant rise in photocurrent under a gradual increase in the magnitude of applied voltage. Stability and reversibility of the PD can be observed by the constant response for on and off current for all measured cycles. Furthermore, the stability and reversibility were also confirmed by the constant optical switch responses as shown in Fig. 15f. Ding and co-workers synthesized non-toxic and square-shaped microsheets of 2D Pb-free perovskite $(PEA)_2SnI_{4x}Br_x$ $(x = 0,1,2)$ by using the ternary solvent method [229]. They reported for the first time higher detectivity 2.06×10^{11} Jones, better photoresponsivity of 3.29×10^3 A W^{-1}, and a higher photo-conductive gain of 8.68×10^3 of 2D lead-free perovskite microsheets-based PDs. The schematic diagram of device Au top electrodes, 2D perovskite, and Si/SiO_2 substrates is shown in Fig. 15f upside. Constant photoswitching response at multiple cycles in terms of I–T plots under 195.8 μW cm^{-2} illumination, 5-s on–off intervals, and 470 nm wavelength incident light is shown in Fig. 15g (bottom plot). As discussed earlier, 2D layered perovskites with quantum confinement effect and tunable bandgap can detect circularly polarized light (CPL) and can be used in magnetic memory devices, optical data mechanisms, display technologies, telecommunication, and chiral catalysis [230, 231]. All these advancements are attracting the researchers toward 2D layered perovskites-based PDs. 2D organic and inorganic hybrid perovskite materials are efficient to develop ultra-thin and fast photodetectors due to their outstanding features like high absorption, high mobility, and tunable bandgap. Many photodetectors have been reported based on organic and inorganic hybrid perovskite materials; for example, $MAPbX_3$ materials-based photodetector exhibits outstanding photodetection in visible range and response speed can be suppressed by 1 ns. But restricted by the bandgap, detection of the light is only limited to the visible range. Some reports suggested that detection ability can be increased to NIR region by perovskite materials assisted with quantum dots and polymer. Huang and co-workers synthesized 2D organic–inorganic hybrid layer-structured perovskites. Optical image of $C_4H_9NH_3)_2PbI_4$ (n = 1) and $(C_4H_9NH_3)_2(CH_3NH_3)_2Pb_3I_{10}$
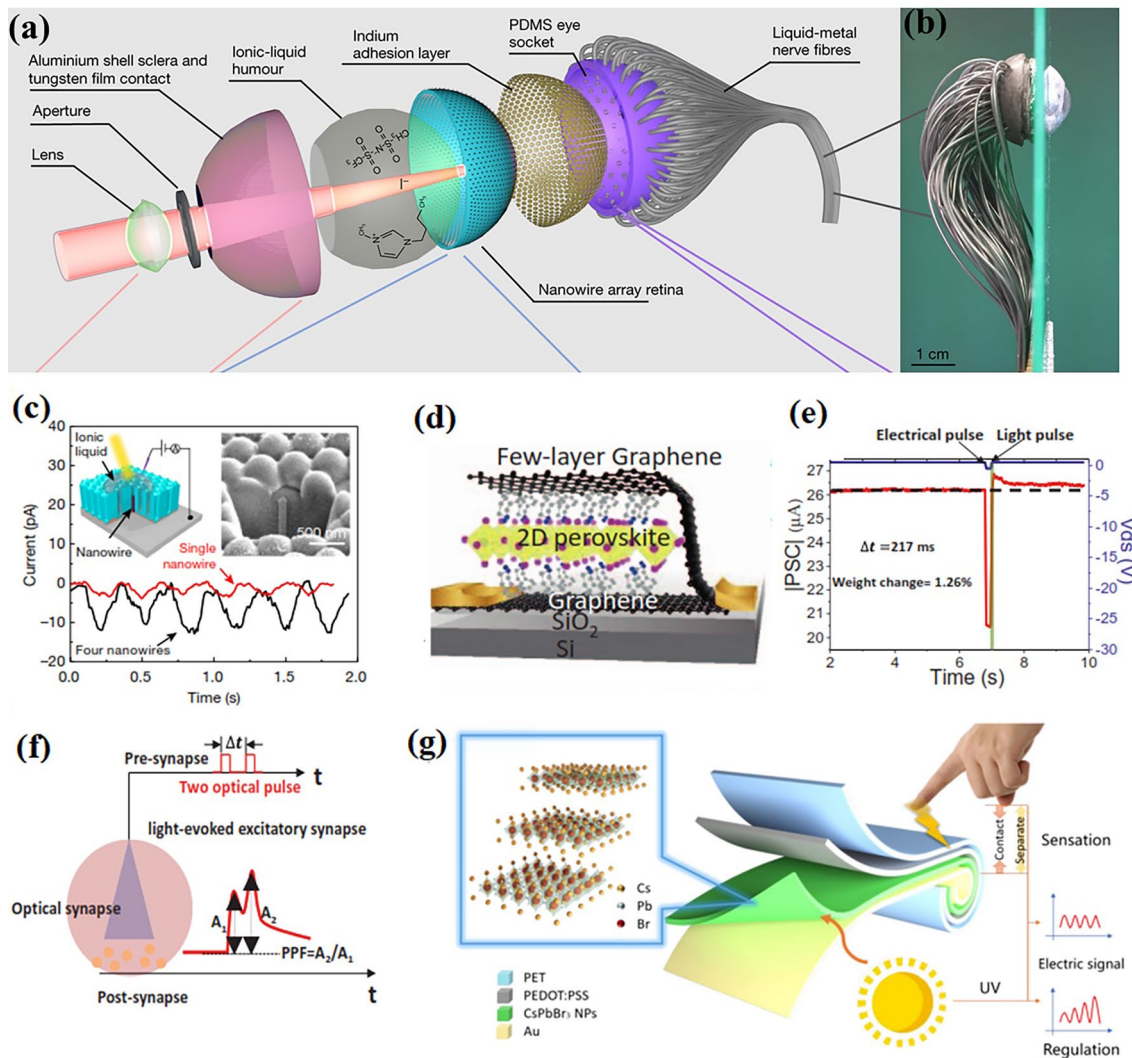
Fig. 16 Brief schematic of EC-EYE architecture with all components **a** exploded, **b** top view and **c** its transient photoresponse [51]. **d** Schematic of the optically stimulated synaptic device consists of 2D perovskite sandwiched between graphene layers on Si/SiO$_2$ substrate side as a post-synaptic terminal. **e** Synaptic response as LTP and 217 ms delay time under pre-synaptic light input and post-electrical pulse. **f** Analysis setup for optically induced synapse with two optical pulses [234]. **g** Structural schematic and working mechanism of e-skin [235]

(n = 3) 3 layered perovskites with yellow and brown colors, respectively, is shown in Fig. 15h. SEM images of 1 layered perovskite clearly show the presence of irregular and partially discontinuous film formation which leads to insufficient light-harvesting (Fig. 15h). SEM image of 3 layered perovskite films shows better film morphology with smooth and flat surfaces. Better film morphologies with several optical band gaps of these layered materials have the potential for improved photoelectronic properties as demonstrated in Fig. 15i. UV–Vis absorption spectrum of 1, 2, and 3 layered perovskites was plotted with different characteristic absorption peaks for all three perovskites, i.e., 515, 570, and 605 nm, respectively.

The corresponding optical band gaps for 1, 2, and 3 layered perovskites (2.33, 2.11, and 2.00 eV) were also reported. The difference in the optical band gaps can be attributed to different molecular structures, which directly affect the photo response of PD for multiple wavelengths of incident lights.

2.6 High-Resolution Artificial Retina and e-Skin

Biological eyes are indeed the most valuable sensory organ for living species on the earth [232]. More than 80% of the information to the brain is provided by our eyes with

concavely shaped retina, highest broad field of view (FOV), and ultra-high-resolution images. The advantage of the retina's domed shape is that it reduces aberration from the curved focus plane, making optical systems simpler. Artificial vision systems, which mimic human vision, are just as important in autonomous technology like robotics [233]. In particular, robots with humanoid features should have visual systems that resemble with humans, in addition to having better device qualities, to support congenial human–robot interaction. The hemispherical shape of the image sensor which resembles the human retina would be adopted to accomplish that goal. Fan and co-workers fabricated a biomimetic electrochemical eye (EC-EYE) with a hemispheric shape by using high-density perovskite nanowire retina [51]. Figure 16a shows a thorough structure of EC-EYE. In this architecture, light-sensitive, functional electrodes are made from nanowires. The counterelectrode is a tungsten (W) layer on an aluminum (Al) hemispherical shell. The cavity is filled with the ionic liquid between two electrodes, acting as an electrolyte and simulating the vitreous humor in human eye. To improve contact between the liquid metal and the nanowires, flexible eutectic gallium indium liquid–metal wires in soft rubber tubes are used to transmit signals between the nanowires and external electronics. Top view of the fabricated EC_EYE is shown in Fig. 16b. The possibility for excellent image resolution is one of the key advantages of adopting high-density nanowire arrays for artificial retina. Inset of Fig. 16c shows with a focused ion beam, a single nanowire grew in a single nanochannel, producing a single pixel with a lateral dimension of 500 nm and a footprint of 0.22 m. The graph (Fig. 16c) shows the photoresponses of 4 nanowires and single nanowire-based devices. Ren and co-workers fabricated 2D perovskite-/graphene-based highly efficient optical synapses and used them as an artificial eye [234]. Due to the huge amount of data interchange between the CPU and memory in traditional von Neumann designs, they consume a lot of power. To solve this limitation, neuromorphic computation with large-scale synapses and neurons, which can be considered a partially distributed architecture, has been proposed by Ren et al. Figure 16d shows the structural diagram of the fabricated device with 2D perovskite sandwiched between graphene layers on Si/SiO$_2$ substrates. As a pre-synaptic input, a light signal is applied to the optical synapse, and an electrical pulse as a post-synaptic input is applied at the drain as mentioned in a graphical illustration (Fig. 16e). LTP occurs when the electrical signal arrives

217 ms after the electrical signal arrives and before the light pulse, i.e., 105 ms. In biosynapses, the paired-pulse facilitation (PPF) effect is a crucial short-term function that our optical synapse can replicate. Two laser pulses are delivered to at $V_g = 10$ V and $V_{bias} = 500$ mV, and PSC reaches maximum after the second light pulse.

Artificial skin, often known as electronic skin (e-skin), is crucial to the development of future artificial intelligence systems. Fabrication of e-skin is another important discovery toward humanoid robotics. Several attempts have been made to fabricate flexible e-skin that can detect several stimuli, but the primary stumbling block is the lack of self-regulation and learning from the environment. Kim and co-workers reported the optically induced, self-powered smart e-skin that uses photosensitive perovskite technology to achieve photoelectric neural computing and tactile sensing to enhance the human–machine interface [235]. 2D perovskite nanoplates were used to achieve the photoelectric and triboelectric effects for the functioning of e-skin. The electrode-free triboelectric concept was used to generate electrical signals from mechanical stress. The skin also works as an optoelectronic memory and possesses several synaptic behaviors. E-skin consists of a single 2 cm × 2 cm element with flexible PET substrate, PEDOT:PSS layer, CsPbBr$_3$ perovskite nanoplates, and Au contacts. The sensation mechanism with optical and mechanical stimuli and heterostructure device architecture is shown in Fig. 16g.

2.7 LD perovskite-based Photovoltaics

In the past decades, rapid population growth and huge industrial progress dramatically increased energy demand. This boom in energy demand forced people to think about clean energy alternatives to conventional fossil fuels. These replacements can be regarded as renewable and sustainable energy resources [236, 237]. Commonly used natural and sustainable energy methods include wind energy, hydraulic energy, bioenergy, and solar energy. However, solar energy is considered to be a distinguished source of electricity due to the continuous and extensive supply of energy by the Sun. Recently, photovoltaics (PV) seems to be the best solar energy harvesting technology; it directly converts solar energy into electrical energy in the most promising way to overcome the energy crises we are facing now [238, 239]. After the discovery of the photovoltaic effect in 1839 by

French physicist Alexandre-Edmond Becquerel, research advanced significantly, culminating in 1954 when Daryl Chapin, Calvin Fuller, and Gerald Pearson successfully developed the first crystalline silicon (c-Si) solar cell at Bell Labs [240]. Following this breakthrough, researchers made continuous improvements in silicon-based solar cells [241–243], including enhancing the quality of amorphous silicon (a-Si) layers [244, 245] for better interface [246] and photocurrent enhancement [247, 248], replacing c-Si wafers with epitaxial silicon (epi-Si) films [249, 250], and make their real life applications [251]. However, despite these advancements, the high cost and lack of flexibility of silicon-based solar cells have limited their wider adoption in the market.

Consequently, much effort has been invested in exploring alternatives to silicon-based solar cells, such as organic solar cells (OSCs), dye-sensitized solar cells (DSCs), perovskite quantum dot-embedded solar cells, organic–inorganic hybrid solar cells, and inorganic perovskite-based solar cells (PSCs). Additionally, the incorporation of electrically harmless nanocoatings has been explored to further enhance the efficiency and durability of these alternative technologies [252–254]. Miyasaka et al. first time used organic–inorganic hybrid perovskite in 2009 for photovoltaic applications with 3.8% PCE [74]. After that in 2012, the performance was enhanced up to 9% by Gratzel and co-workers by using lead iodide perovskite-based solar cells [255]. Several research groups are working to improve the efficiencies and stabilities of perovskite-based solar cells to make them an industrially feasible candidate [256]. Alternately quantum dots embedded in perovskite are also another strategy to fabricate intermediate band solar cells [257].

Matteocci et al. used organic–inorganic hybrid perovskite and added a very small thickness of MoS_2 between $CH_3NH_3PbI_3$ and spiro-OMeTAD enhancing the efficiency of solar cells by about 13.3% [258]. In 2016, Tsai and co-workers enhanced the structural arrangement of the quasi-2D perovskite by hot casting method for a planar PCS and reported 12.5% PCE for BA)$_2$(MA)$_3$Pb$_4$I$_3$ [259]. Due to the low-cost fabrication process and higher power conversion efficiencies (PCE), the PSC (25% PCE) and OSC (10% PCE) rapidly achieved tremendous attention from researchers [260]. Extremely high PCE and very simple fabrication process and their light management properties are making PSCs the best emerging competitor in the field of solar cells [261]. Researchers are predicting that it will beat commercial Si-based solar cells soon [262]. The structural flexibility of 2D perovskites can be utilized to tune the opto-electronic properties and make them feasible for the practical application of devices. The strong excitonic response was observed with $n \leq 2$ most probably due to quantum confinement effects. At room temperature, this results in the highest photoluminescence yield, making it suitable for light-emitting applications. However, $n \leq 2$ perovskites are not suitable for PVs due to their narrow absorption and high exciton binding energy; on contrary, for $n \geq 3$ low exciton binding energy, smaller bandgap, and extended light absorption of perovskites in the visible region make them suitable for photovoltaic application. Figure 17a represents the structural diagram for Au/Spiro-OMeTAD/perovskite/SnO$_2$/FTO solar cell. To confirm the effect of BEAI$_2$ treatment on the performance of the devices, the current density–voltage (J–V) measurements were taken with and without BEAI$_2$ treatment. Figure 17b shows the J–V curves of PSCs with and without BEAI$_2$ treatment. Inset table of Fig. 17b gives complete detail about different performance parameters. The results clearly illustrate the dominant performance of BEAI$_2$ with J_{SC} 23.32 mA cm^{-2}, FF 0.73, and PCE 19.58% which is complete dominant than J_{SC} 22.96 mA cm^{-2}, FF 0.71, and PCE 17.39%. The main booster in efficiency is the formation of 2D layer by post-treatment of BEAI$_2$ at 3D interfaces. In addition to the performance parameters, the post-treated devices show excellent reproducibility as shown in Fig. 17c [263]. Considering more research on 2D perovskite-based solar cells, a graphical conductivity assessment comparison at different temperatures of 3D (MAPbI$_3$) and 2D (BA)$_2$(MA)$_3$Pb$_4$I$_{13}$) films is studied in Fig. 17d, e. Schematic alignment for RPPs energy levels with $n = 2$ and $n = 10$ and its charge transfer mechanism is also mentioned in Fig. 17f [264]. 2D layered perovskites bring ease for tuning the layer thinness by adjusting n values, with a noticeable impact on perovskite structure. In Fig. 17g, the 2D (PA)$_2$(MA)$_{n-1}$Pb$_n$I$_{3n+1}$ family structures with increasing inorganic layer thickness from $n = 1$ to $n = 5$ are presented [70].

Figure 17h shows the stability comparison between 2 and 3D perovskite devices at continuous light irradiation for a long time (< 2,500 h). The graphical results illustrate the long-term stability of 2D perovskites as compared to unstable 3D perovskites. 2D perovskites-based devices are almost 80% stable after 2,500 h [265]. Zhou et al. reported (BA)$_2$(MA$_{1-x}$FA$_x$)$_3$Pb$_4$I$_{13}$, x = 0, and 0.2, Q-2D
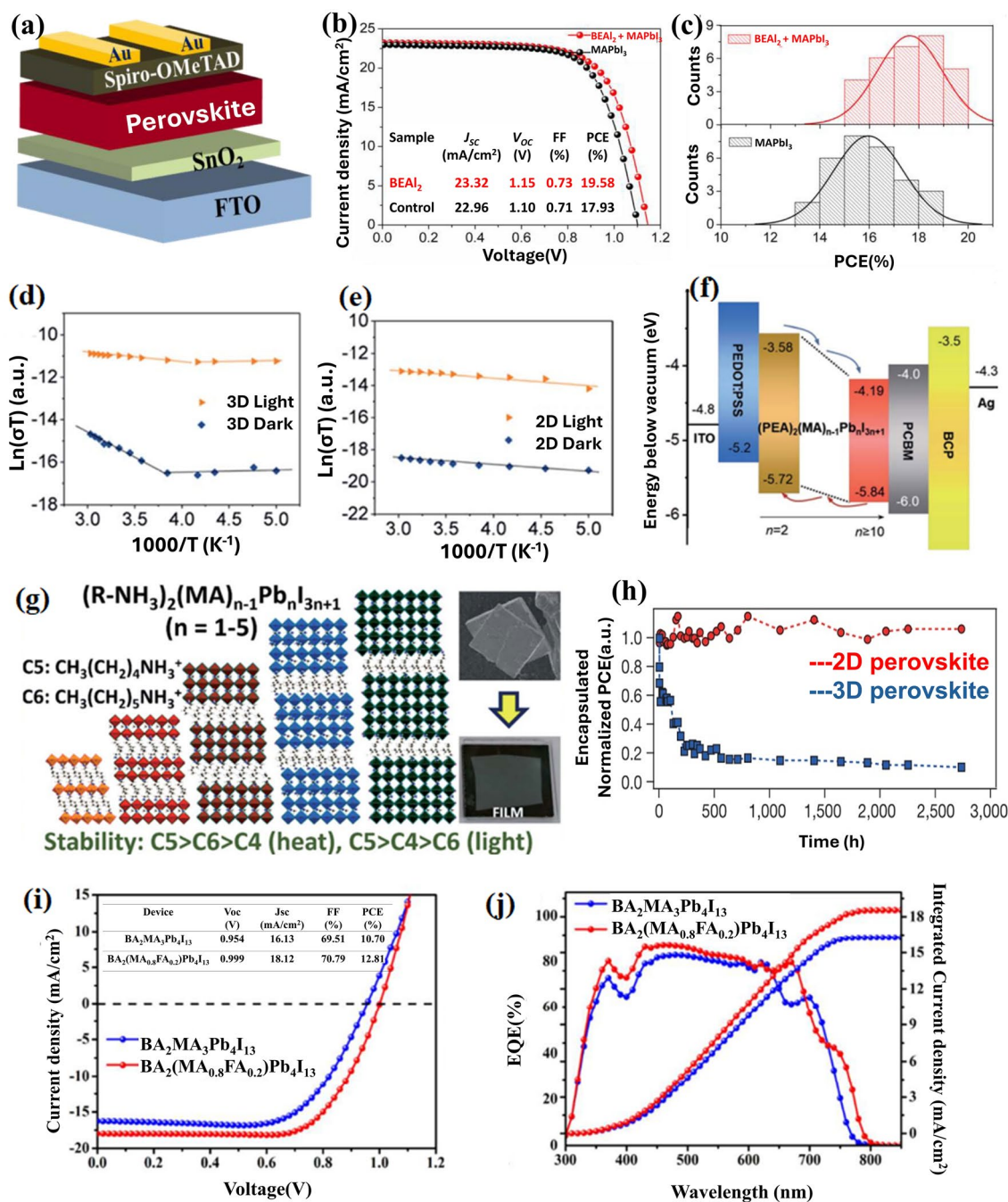
Fig. 17 **a** Structural architecture for Au/Spiro-OMeTAD/perovskite/SnO$_2$/FTO Solar cell. **b** J–V curves of PSCs with and without BEAI2 treatment. **c** Multiple devices stability against PCE for both perovskite solar cell groups [263]. Conductivity assessment at different temperatures of **d** 3D (MAPbI$_3$) and **e** 2D ((BA)$_2$(MA)$_3$Pb$_4$I$_{13}$) films. **f** Schematic alignment for RPPs energy levels with n = 2 and n = 10, and its charge transfer mechanism [264]. **g** 2D (PA)$_2$(MA)$_{n-1}$Pb$_n$I$_{3n+1}$ family structures with increasing inorganic layer thickness from n = 1 to n = 5 [70]. **h** Stability comparison between 2 and 3D perovskite devices at continuous light irradiation for a long time (< 2,500 h) [265]. **i** J − V curve and **j** EQE response for inverted device structure of (BA)$_2$(MA$_{1-x}$FA$_x$)$_3$Pb$_4$I$_{13}$, x = 0, and 0.2, Q-2D perovskite-based solar cells [266]

perovskites as light absorbers films for photovoltaics applications in the inverted architecture of ITO/PEDOT: PSS/perovskite/PCBM/BCP/Ag. In this architecture, PEDOT:

PSS serves as a hole transport layer while PCBM acts as an electron transport layer. Figure 17i, j shows the J − V curve and EQE response for inverted device structure of
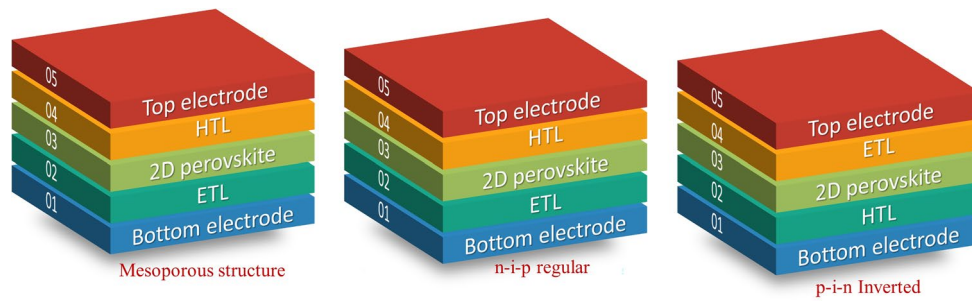
Fig. 18 Solar cell structural configurations with **a** mesoporous, **b** n-i-p, and **c** p-i-I structures

Table 1 Performance and stability of various LD perovskite compositions for photovoltaic applications

Material composition	(PCE) (%)	(Voc) (V)	(Jsc) (mA/cm^2)	(FF) (%)	Stability	Fabrication method	Device architecture	References
$(BA)_2(MA)_{n-1}Pb_nI_{3n+1}$ (n = 3, 4)	12.52%	~1.10	15.2	~75	> 95% after 1655 h in N$_2$	Hot casting	ITO/2D perovskite/ PCBM/Ag	[259]
$(BA_{0.5}PEA_{0.5})_2FA_3Sn4I_{13}$	8.82%	0.60	21.82	67	Improved stability	Spin-coating	Planar heterojunction	[273]
$(ThDMA)(MA)_4Pb_5I_{16}$	15.75%	~1.05	19.8	~78	> 95% after 1655 h in N$_2$	Solvent engineering (DMF:DMSO)	FTO/TiO$_2$/perovskite/ Spiro-OMeTAD/Au	[274]
$(4AMP)(FA)_3Sn_4I_{13}$ (DJ phase)	4.22%	0.64	14.90	44	–	4AMP spacer	ITO/TiO$_2$/ZrO$_2$/perovs-kite/Cr	[275]
$AVA2FA_{n-1}SnnI3_{n+1}$ (⟨n⟩ = 5)	8.71%	0.61	20.15	68	Improved stability	Spin-coating with NH4Cl additive	Planar heterojunction	[276]
$(en)FASnI_3$	7.14%	0.48	22.54	66	Improved stability	Spin-coating	Planar heterojunction	[277]
FA-based quasi-2D RP (n = 5)	16.18%	~1.10	20.1	~80	High humidity/ thermal stability	Antisolvent	ITO/SnO$_2$/perovskite/ Spiro-OMeTAD/Au	[278]
$(BA)_2(MA)_3Pb_4I_{13}$ + GABr	19.3%	~1.15	21.0	~80	Improved light/ thermal stability	Secondary crystal-lization	ITO/NiO$_x$/perovskite/ PCBM/Ag	[279]
$(TN)FASnI_3$	5.53%	0.40	22.72	61	Improved stability	Spin-coating	Planar heterojunction	[280]
$(PDA)(FA)_3SnI_4$ (o-PDA spacer)	7.18%	0.489	20.69	71	–	o-PDA spacer	ITO/PEDOT:PSS/perovs-kite/DCM/BCP/Ag	[281]
$(PEA)_2(FA)_6Sn_4I_{13}$	5.94%	~0.50	18.3	~65	> 100 h in air (unencapsulated)	Hot casting	ITO/PEDOT:PSS/perovs-kite/PCBM/Ag	[282]
$(GA)2FA_{n-1}SnnI_{3n+1}$	9.60%	0.61	21.20	72	Improved stability	Spin-coating with EDA2 additive	Planar heterojunction	[283]
$(PEA)_2PbI_4$	3.2%	1.24	4.5	56	Low (degrades in humid air)	Vacuum-assisted deposition	ITO/PEDOT:PSS/ (PEA)$_2$PbI$_4$/PCBM/Ag	[284]
$AVA_2FA_4Sn_5I_{16}$ (RP phase)	8.71%	0.61	21.0	68	Retained > 80% PCE after 30 days in ambi-ent air (RH ~ 30%	NH$_4$Cl + 5-AVA$^+$ spacer	ITO/PEDOT:PSS/Spiro-OMeTAD/BCP/Ag	[276]
$(PEA)_2FA_{n-1}Sn_nI_{3n+1}$ + SnF$_2$	9.41%	0.61	22.00	70	Improved stability	Spin-coating	Planar heterojunction	[285]
$(BA_{0.7}PEA_{0.3})_2FA_3Sn_4I_{13}$ (RP phase)	8.82%	0.60	21.82	67	–	Mixed BA/PEA spacers	ITO/PEDOT:PSS/Perovs-kite/Ca/LiF/Al	[273]
MASnI3 + 10% TEAI	6.80%	0.53	19.80	65	Improved stability	Spin-coating	Planar heterojunction	[286]
$BA_2FA_3Sn_4I_{13}$ (RP phase)	4.04%	0.42	23.96	40	–	BA spacer	ITO/bi-TiO$_2$/mp-TiO$_2$/ PTAA/Au	[287]
$(C_6H_5C_2H_4NH_3)_{24}PbI_4$	2.8%	1.15	4.1	59	Moderate (stable under N$_2$)	Hot-casting tech-nique	ITO/NiO$_x$/ (C$_6$H$_5$C$_2$H$_4$NH$_3$)$_2$PbI$_4$/ PCBM/Ag	[288]
BDAPbI$_4$ (1D lead iodide wires)	14.1%	-	-	-	95% after 1000 h	Solution process-ing	Not specified	[289]

$(BA)_2(MA_{1-x}FA_x)_3Pb_4I_{13}$, x = 0, and 0.2, Q-2D perovskite-based solar cells, respectively [266].

Compared with more than 26% PCE reported in 2024 for 3D perovskite [267], the Dion–Jacobson 2D PSCs achieved the highest efficiency of 19.11%, among all other low-dimensional perovskite in 2024 [268]. Tremendous advancements in device structure [255, 269], high-quality film formation [270, 271] synthesis methods, architectural engineering of perovskite materials [260, 272] have led to boost the PCE of PSCs. The revolution in PSCs performance opened new ways to understand and enhance the PCE; one of the main approaches is the device architecture which includes mesoporous, n-i-p, and p-i-p device structure as presented in Fig. 18. These structures can be used in planner as well as inverted device structures. Table 1 shows the comparative summary of different LD perovskite material compositions, their photovoltaic performance parameters (PCE, V_{oc}, J_{sc}, FF), stability, fabrication methods, and device architectures.

2.8 LD Perovskite-based LEDs

Low-dimensional perovskites are gaining attention for light-emitting devices because of their unique emission characteristics, which include ultra-broad, strongly Stokes-shifted luminescence with white light chromaticity [290]. Typical "sandwich" architectures are seen in LEDs, which can be classified as single-layer, double-layer, three-layer, or multi-layer structures based on the number of layers. Aside from the substrate, cathode, and anode, the emissive layer (EML) is the only component of the most basic single-layer system. Due to the imbalanced carrier transport and the quenching phenomena of the interface between the electrodes and EML, the device's efficiency is rather low despite its simple preparation method [291]. When compared to a monolayer structure, a double-layer structure increases the carrier transport efficiency and exciton recombination likelihood by adding an additional layer of either the hole transport layer (HTL) or the electron transport layer (ETL) [292]. By creating a new low-temperature reverse microemulsion technique, Zheng et al. fabricate a novel class of nano crystals (NC), which are colloidal semiconductors, by using 0D perovskite Cs4PbBr6 with an 85% yield of the reaction [293]. These 0D perovskite NCs have a superior photoluminescence quantum yield (PLQY) in both colloidal and thin-film forms (PLQY: 65% and

54%, respectively). Zhou et al. reported a 0D-tin mixed halide perovskite-based broadband yellow light emitter with high efficiency [294]. This phosphor's excited state structural rearrangement results in a significant broadband yellow emission with Stokes shift that peaked at 582 nm. It possesses a high PLQY of around 85% at room temperature and a broad full width at half maximum (FWHM) of 126 nm [294].

Cao and co-workers in 2018 fabricated for the first time low-dimensional perovskites-based LEDs by using solution process method that spontaneously form sub micrometer-scale structures; they exhibit high-brightness and efficient electroluminescence [295]. These structures can effectively extract the light from the device while maintaining electroluminescence at every wavelength and viewing angle. Amino acid additives are added to the perovskite precursor solutions to create these perovskites. These compounds can also decrease non-radiative recombination and passivate perovskite surface imperfections to improve the EQE of final devices. Xing et al. use a small ligand called isopropyl ammonium (IPA) which moderately replaces the long ligand called phenylethyl ammonium (PEA) for fabricating the quasi-2D perovskites. The process controls the crystallization of these perovskites to produce stable in color, with blue emissions perovskite thin films with high PLQYs [296]. The combined use of IPA and PEA ligands inhibited the development of the lowest-n and highest-n phases, allowing the formation of the intermediate-n phases to take center stage. The resulting films exhibit steady blue emission and extremely efficient photo luminance. Furthermore, by mixing metal halide perovskites with polymer Tian et al. fabricated perovskite-based red LEDs which are stable and extremely efficient use perovskite composite thin films as the light-emitting interface [297]. Highly luminous perovskite thin films made by varying the molar ratios of organic salts (benzyl ammonium iodide) to inorganic salts (cesium iodide and lead iodide) may emit hues that range from red to very dark red. Compared to their clean quasi-2D perovskite counterparts, thin films of quasi-2D perovskite/PEO composite have much higher photoluminescence quantum efficiencies. For these red perovskite LEDs, remarkable electroluminescence spectrum stability has been attained under continuous device operation.

Sargent et al. reported that by employing a bifunctional chemical additive that concurrently regulates the reduced-dimensional perovskites poly-dispersity and passivates the
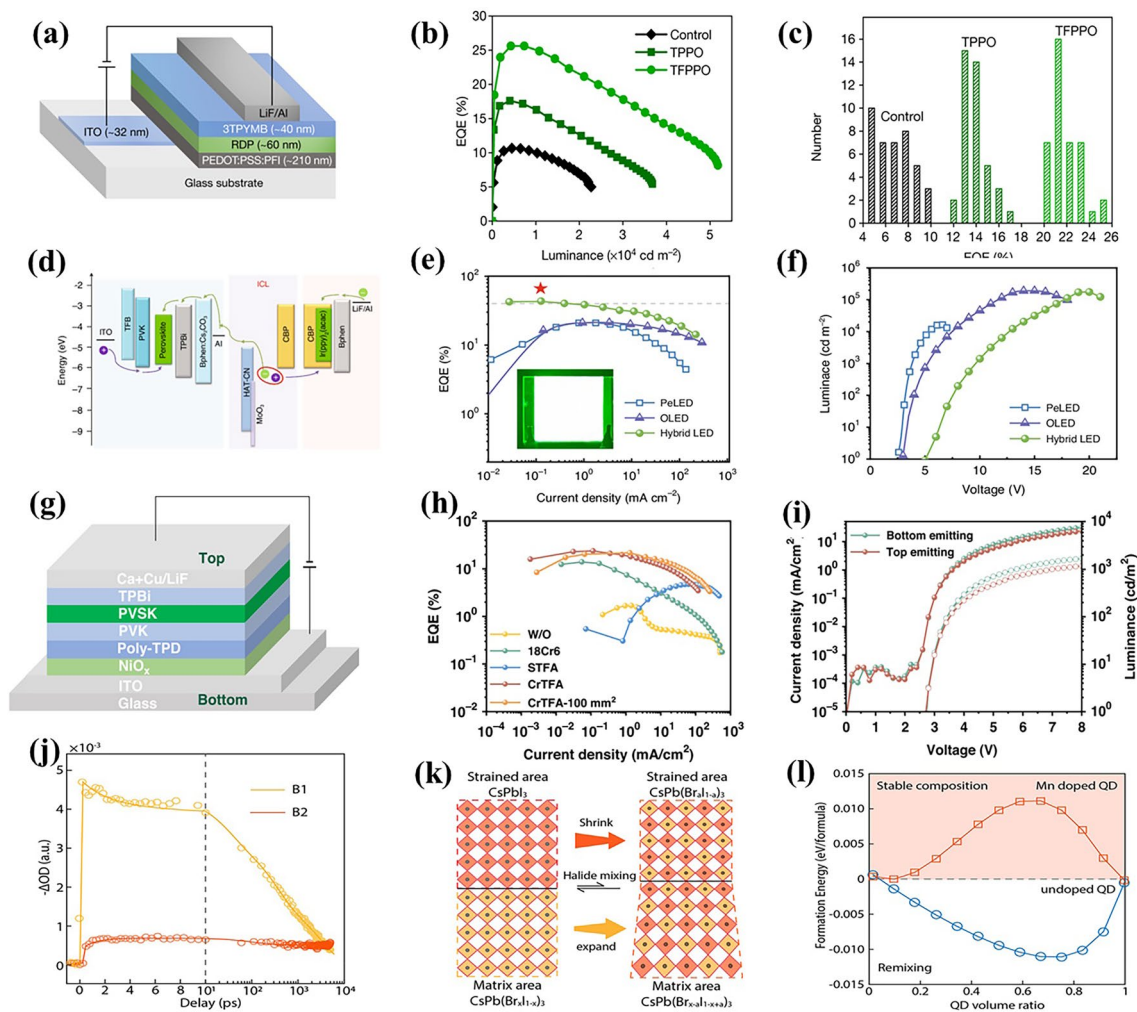
Fig. 19 **a** LED device schematic sowing all layers. **b** Luminance-dependent EQE curves and **c** histogram of 40 devices showing the EQE of TPPO-treated and TFPPO-treated RDPs based devices [298]. **d** Schematic energy band diagram of the fabricated device. **e** EQE-J characteristics of all LEDs and maximum EQE marked by a red star. Inset shows a hybrid LED photograph at 7.5 V bias and a 30 mm×30 mm active area. **f** Voltage-dependent luminance curves [299]. **g** Structural schematic of the device sowing all layers. **h** EQE off all devices. **i** J–V–L of both top and bottom emitting PeLED [300]. **j** Optical properties of QD-in-matrix solids. Representing kinetic traces of the B1 and B2 peaks. **k** Schematic showing transition of QD-in-matrix from a stable to a halide-remixed phase with bromide migration to strained QD. Anion exchange at the QD/matrix interface induces material strain. **l** Total free energy change (red) during the transition in **k** versus strained QD volume ratio. Free energy changes for halide mixing from unstrained iodide domains and matrix perovskite to the halide-remixed phase are also shown (blue) [301]

perovskite quantum well (QW) surfaces, reduced-dimensional perovskites (RDP) with a more monodispersed QW thickness distribution are created, along with a fluorinated triphenylphosphine oxide additive that creates a hydrogen bond with the organic cations, preventing the production of low-thickness QWs and regulating their diffusion during RDP film deposition [298]. By forming coordination bonds with unsaturated sites, the phosphine oxide moiety passivates the perovskite grain boundaries and prevents the production of defects. This produces RDP thin films that are

compact, homogeneous, and smooth, with high photoluminescence quantum yield and narrowband emission.

Figure 19a shows the schematic diagram of LED fabricated by using ITO-coated glass substrates with patterns used to make LEDs (thin-film devices) on which PDOT: PSS (poly(3,4-ethylenedioxythiophene)-polystyrene sulfonate) and PFI (nafion perfluorinated ionomer) with ratio 1:1 were deposited; then, RDPs as active layer and similarly other layers were deposited. Figure 19b shows EQE-Luminance characteristics of control, TPPO (triphenylphosphine

oxide)-treated, and TFPPO (tris(4-fluorophenyl)-phosphine oxide)-treated RDP-based LEDs where TFPPO treatment RDP-based LEDs show enhanced luminance as compared to control and TPPO. Figure 19c shows that RDP-based LEDs treated with TFPPO comparatively have a very high EQE of 25.6% while TPPO-treated LEDs and control had EQEs of 17.6% and 10.7%, respectively.

Yang et al. combine the commercial organic LED along with perovskite LED to create a hybrid LED with a tandem structure that is stable, efficient, and has good color purity [299]. Perovskite and organic LEDs with a near photoluminescence peak are used to attain narrow emission spectra and maximum photon output without photon re-absorption. The green-emitting hybrid LED results from the design of an effective inter-connecting layer in addition to doping the p-type interface that reduces Joule heating and runs competent optoelectric pairing and maximum external quantum efficiency [299]. Figure 19d shows the hybrid device's energy band diagram. Due to the synchronized energy levels of the suggested ICL (inter-connecting layer), carriers were efficiently produced at the interface of MoO_3 (Molybdenum trioxide) and CBP (4,4′-bis(N-carbazolyl)-1,1′-biphenyl)), as schematically illustrated, and inject into the top OLED and bottom PeLED under forward bias. The Al and MoO_3 layers inside the devices have extremely small thicknesses. The thin Al layer, as opposed to an external Al electrode, makes it easier for electrons to separate and move from the ICL. The ultra-thin MoO_3 (less than 1 nm) permits holes to pass through the spacer, which is crucial for raising the charge carrier concentration and removing more carriers. The LUMO (unoccupied lowest molecular orbital) of MoO_3 is deeper than that of HAT-CN (1,4,5,8,9,11-hexaazatriphenylene hexacarbonitrile), but it is also lower than the HOMO (highest occupied molecular orbital) of CBP (4,4′-bis(N-carbazolyl)- 1,1′-biphenyl). This allows electrons to move from p-type interface-doped CBP to HAT-CN, enhancing the built-in electric field and enabling the creation of high-performance devices. Figure 19e shows that the luminance–voltage (L–V) graph has much higher luminance peaks of hybrid LED as compared to single sub-unit devices. Figure 19f shows the EQE-J properties of hybrid LED, PeLED, and LED where the star is highlighting the maximum efficiency value point. The hybrid LEDs are extremely efficient for generating carriers, injections, and recombination indicated by the extremely higher peak of EQE of 43.42%, which corresponds to a current efficiency

that is nearly equal to the sum of the values of PeLED and OLED.

Ning et al. created a supramolecular method to control green emissive perovskites' crystallization kinetics using dual additives which slowdowns crystal growth, lowers nucleation centers, and fabricated LED with improving the efficiency nearly 21.6% also reached the external quantum yield around 23.9% [300]. Figure 19g illustrates the device's schematic, which begins with ITO-coated glass and progresses to the deposition of a NiO_x (nickel oxide) layer. Layers of PVK and poly-TPD are then applied to the NiO_x to create a stacked energy level alignment that speeds up hole injection, perovskites serve as the light-emitting layer; further TPBi (40 nm thick), LiF (1.2 nm thick), and Ca (8 nm)/Cu (4 nm) are deposited, respectively. Figure 19h shows the comparison of external quantum efficiency of various fabricated devices including without using additives, using one and more than one additive. The CrTFA (combination of STFA and 18Cr6 (18- crown-6)) device shows the lowest turn-on voltage, with effective carrier injection, low series resistance, and highest external quantum efficiency while STFA (sodium trifluoroacetate) and 18Cr6 exhibit low external quantum efficiencies because of delayed carrier transfer and high non-radiative recombination. Figure 19i displays the transparent device's current density–luminance–luminescence (J–V–L). The representative device indicates effective carrier injection from both electrodes by turning on at a low voltage of about 2.8 V. The maximum peak value of around 5.7% is obtained from the other side, whereas the ITO side's emission yields a peak of 7.9% for EQE.

Sargent et al. encapsulate strain-induced QDs as nucleation sites to create stable, bright QDs with a thin coating of perovskite precursor solution and to encourage the homogeneous crystallization of a perovskite matrix [301]. Figure 19j depicts that there are no observable emissions from the perovskite matrix in the hybrid material's PL spectrum. In the first 2 ps, the bleach recovery dynamics of B1 and B2 show that B1 recovers quickly while B2's bleach amplitude increases. Figure 19 k reveals the migration of bromide from matrix to strained QD during the change from the compositionally durable QD-in-matrix phase to the halide-remixed phase. The material experiences strain because of anions with varying atomic sizes exchanging places at the QD/matrix contact. Lattice matching is compromised when the halides are moved between the QD and the matrix. The QDs function as charge acceptors and luminophores when surrounded in a semiconducting matrix. Figure 19l shows

Table 2 Comparison of optoelectronic properties including PLQY, dimensionality, and film morphology of LD perovskite-based LEDs

Material composition	External quantum efficiency (EQE)	Film morphology	Photo-luminescence quantum yield (PLQY)	Dimensionality	References
$PEA_2Cs_{16}MA_{08}Pb_3Br_{10}$ + TFPPO	25.6% (max), $22.1 \pm 1.2\%$ (avg)	Compact, smooth, uniform	Highest (improved by passivation)	Quasi-2D (Reduced-Dimensional Perovskite)	[298]
$PEA_2(CsPbBr_{14}Cl_3)_{n-1}PbBr_4$ + DFBP	15.03% (max), 13.55% (avg)	Smooth, dense, uniform	64.3% (under 320 nm excitation)	Quasi-2D (optimized phases)	[302]
$(PEA)_4(S/R-PRDA)_{2-x}Sn_{0.1}Pb_{0.9}Br_4$ chiral 2D perovskite	5.7%	Smoother surface with Sn^{2+} doping	–	2D (Sn^{2+}-doped)	[303]
$(TPA)_2MnBr_4$ (TPA = tri-n-propylammonium)	–	Crystalline powder (for LED deposition)	62%	0D (isolated $[MnBr_4]^{2-}$ tetrahedra separated by TPA^+ cations)	[304]
$(MBA/MPPA/MOPA)_2Cs_{n-1}Pb_nI_{3n+1}$	28.7% (638 nm); 22.2% (627 nm); 25.1% (645 nm)	Smooth, uniform films	> 80% (for optimized MM-MOPA films)	Reduced-dimensional (quasi-2D) Ruddlesden–Popper perovskite with MOPA ligand	[305]
$Cs_3Cu_2I_5$	0.1%	Polycrystalline thin film	90%	0D (Isolated $[Cu_2I_5]^{3-}$ clusters)	[306]
$Ph_4P)_2MnBr_4$	7.2%	Grainy requires host matrix (e.g. TAPC)	–	0D (Isolated $[MnBr_4]^{2-}$ tetrahedra)	[307]
$CsCu_2I_5$	7.4%	Densely packed, fewer defects	84.8%	1D ($[Cu_2I_5]^-$ chains)	[308]
$Cs_3CeCl_6 \cdot 3H_2O$	0.13%	Nanocrystal aggregates	~ 100%	1D ($[CeCl_6]^{3-}$ chains)	[309]
$(PEA)_2SnI_4$	9.32%	Micron-sized islands → compact films	–	2D $[SnI_4]^{2-}$ sheets	[310]
$Cs_3Sb_2Br_9$	0.206%	Ligand-coated, smooth	51.2%	2D $[Sb_2Br_9]^{3-}$ layers	[311]
TEA_2SnI_4 + cyanuric acid	20.29%	Reduced defects	–	2D Quantum-confined $[SnI_4]^{2-}$ sheets	[312]
$CsPbBr_3$ (4 nm)	97%	Uniform small nano crystals (NCs)	4.7%	Zero-dimensional	[313]
$CsPbBr_3$ (3.5 nm)	94%	Small NCs	10.3%,	Zero-dimensional	[314]
$CsPbI_3$ (5.4 nm)	≈100%	Small NCs	28.5%,	Zero-dimensional	[315]
$CsPb(Br/I)_3$	93%	Mixed halide NCs	24.4%	Zero-dimensional	[316]
$CsMnBr_3$	65.1%	Chain structure	–	One dimensional(1D)	[317]
$CsPbBr_3@Cs_4PbBr_6$	> 90%	Nanocomposites	Enhanced stability	Core–shell	[318]

a function of the material's strained QD volume ratio, the total free energies change (red) of the transition seen in (Fig. 19k). The halide mixing process's free energy changes are also depicted (blue) from a combination of matrix perovskite and unstrained iodide domains that have the same volume ratio as the halide-remixed phase. A table showing the comparison between different LD perovskite-based LEDs in their film morphology, PLQY, and dimensionality is presented (Table 1). It highlights the impact of different material compositions and passivation strategies on EQE and morphological characteristics. Table 2 shows a comparative overview of different perovskite compositions highlighting their external quantum efficiency (EQE), film morphology, photoluminescence quantum yield (PLQY), and structural dimensionality, along with references.

3 Challenges and Perspectives

This section discusses the ongoing challenges and future prospects in memory devices and artificial synapses. It further examines recent advancements in phototransistors, photodetectors, and high-resolution retina-inspired sensors. Additionally, emerging LED technologies and innovative

integration strategies are explored to overcome current limitations.

3.1 Perspectives Memory Devices

2D perovskites are appropriate for high-performance memory devices because of their high Schottky barrier height and broad bandgap, and higher activation energy. Researchers achieved superior performances including long retention time, higher on/off current ratio, and low operating/switching voltages, long-term stability, ambient conditions synthesis, and excellent reproducibility of 2D perovskites-based memristors. These achievements reveal that 2D perovskites are more reliable compared with 3D perovskite-based devices in resistive switching memory with higher performances and long-term stability. Remarkable improvements are made in terms of device architecture and performance, but for better device design and memristive characteristics optimization, including charge trapping/detrapping and ionic transport, scientists still require a deeper knowledge of the analytical models and memristive mechanism, universal memristive properties for memory and applications of neuromorphic computing, photonics responses of memory, better controllability for conductive pathways and novel multifunctionalization for industrial applications.

3.2 Perspective Memory and Synapse

Artificial synapses have attained remarkable attention due to their high energy efficiency, fast and reliable performances, self-learning, and massive parallel characteristics. Due to the existence of intrinsic defects, 2D perovskite has greater ion migration and charge trapping effects, making it suited for multi-level artificial synapses. It also has a lot of potential for the future development of neuromorphic computing. 2D perovskites are becoming an alternative for photo and photoelectric stimulated synaptic devices due to achievements toward better synaptic plasticity, fast learning process, long-term STP and LTP with low power consumption. 2D perovskite-based phototunable artificial synapse expands its applications toward visual simulated neuromorphic computing. Halide perovskite-based memristors are suitable for monolithic integration with silicon CMOS-integrated circuits. This will provide an opportunity to integrate nanoscale memristors with CMOS electronic circuits for advanced synaptic functions neuromorphic computing applications.

Two-terminal synaptic devices perform the electronic signals transfer and self-learning process separately, while three-terminal synaptic devices are capable of both learning mechanisms and signal transmission at the same time. Considering synaptic plasticity as a fundamental principle for the human brain's learning and memory process, the simulation of an artificial synapse is desirable to achieve high-efficiency neuromorphic computing. Advanced synthesis methods for 2D perovskite with improved interface engineering methodologies and a combination with new materials for parallel processing of signals are desirable. Deep understanding of optoelectronic properties, controlled as well as uniform wafer-scale synthesis, compatibility with traditional CMOS of 2D perovskite for neuromorphic computing should be focused on the near future research.

3.3 Perspective Phototransistors and Synapse

Even though the perovskite-based phototransistors were among early reported electronic devices, there is plenty of room to reach the level of maturity, expected for commercialization. The challenges which require immediate attention of researchers include hysteresis, low working performances, low trap density, transit frequency, and fast degradation of PTs under ordinary conditions with exposure to health, light, and moisture. Several strategies have been adopted to overcome these issues and fabricate better, efficient, and hysteresis-free perovskite-based PTs. Recently, the researchers are working to improve carrier mobility and device performance, with some strategies including interface engineering, combining heterostructure, altering buffer layer, and utilizing these higher efficiency PTs in some novel functionalities i.e., memory, synapse, etc. [319, 320]. Quantum and bandgap engineering are very hot topics in PTs research these days [321, 322]. The perovskites are advantageous over traditional semiconductors in terms of simple synthesis methodologies and better compatibility with maximum substrates. Moreover, the intermediate charge carrier movements (< 100 cm^2 V^{-1} s^{-1}) are also an advantage of these LD perovskite-based PTs. Higher working frequencies with a broad operating range are also necessary to utilize the PTs as commercial displays, wireless communication including wireless transmitters as well as receivers, military communications instruments, and fast operating computer processors. Operating voltage, channel length, contact

resistance, and parasitic overlap among the gate and source/drain electrodes are also crucial factors in controlling the performances of the PTs-based synaptic devices [323–325].

LD perovskites enable us to fabricate an ultra-thin, low cost, and self-powered PTS with high efficiency and long-term stability. These achievements reveal that LD perovskites are more reliable compared with 3D perovskite-based devices in broad range operation with higher performances and long-term stability.

3.4 Perspectives Photodetectors

Photodetectors are facing different challenges for commercialization including long-term air stability and better performances comparatively silicon-based mature technologies. Many attempts have been seen to overcome the stability issue and further enhance efficiency in the perovskite semiconductors materials by different researchers. Low trap density and controlled growth-defined thickness are two factors that may be utilized to improve air stability, high mobility, and improved efficiency in perovskite semiconducting materials. However, researchers are also trying to overcome these issues by applying different techniques, for example, interface engineering, buffer layer, sandwich device geometry, and combining heterostructure with 2D materials. The new research is focused on bandgap engineering, quantum engineering, and the deposition of novel 2D materials in the heterostructure to create efficient FETs and high-performance photodetectors. The function of bandgap engineering is to control the alloy composition during the material's growth, while quantum engineering contains heterostructure layers. 2D materials allow us to fabricate the ultrathin, self-powered, and low-cost photodetector with high efficiency and air stability. In 2D perovskite materials, fast electron coupling at the interface results in a self-trapping phenomenon in between 2D layered perovskite materials. Self-trapping is very advantageous to adjust the electrical and optical characteristics of 2D perovskite materials. As we mentioned, several research groups have made remarkable development in exploring 2D perovskite-based PDs, but there are some challenges for device engineering, and efficiency improvement needed to be overcome. Researchers achieved the feasibility of nanosheets and nanoplatelets synthesis of perovskite, but

at the same time, the morphology and thickness control remain to be improved. The thickness of nanoplatelets or nanosheets is a critical consideration for the quantum confinement mechanism to tune the optical properties of devices. Therefore, we need better synthesis techniques for improved morphology and thickness of the depositing material that has already been accomplished in traditional semiconductors and metal nanocrystals.

Despite the excellent optical properties shown by 2D perovskites, the stability of air and water remains a barrier to their broad applications. Recently, different coating like silica or Al_2O_3 and organic molecular capping were used to improve stability [326, 327]. However, more work is still needed to get a general method with comprehensive suitability for 2D perovskites. The presence of Pb makes lead halide more toxic than other silicon-based semiconductors, which are hazardous for humans and the environment. There have been several attempts to replace safe metal elements for lead; however, the resulting perovskites perform poorly compared to Pb-based perovskites. For example, Sn-based perovskites with bandgaps were used for better optoelectronic applications, but the oxidation of Sn^{2+} to Sn^{4+} makes them unstable compared to Pb-containing perovskites. Similarly, Ge- and Bi-based perovskites possess higher stability, but the large bandgap of these two perovskites limits their light absorption in long-wavelength range responses. Surface passivation, fabricating hybrid bilayer photodetectors, and phototransistor gating are some ways to attain improved performance and better stabilities of PDs. There is a big room to overcome the stability, performance, and toxicity issues to achieve the commercialization of 2D perovskites-based photodetectors.

3.5 Perspective High-resolution Artificial Retina and e-Skin

To enhance the stability of LD perovskites, various coatings such as silica or Al_2O_3 as well as organic molecular capping have been utilized [328]. However, further research is needed to develop a generic technique that is suitable for all LD perovskites. Lead (Pb) halide is more toxic than other silicon-based semiconductors, which are hazardous to humans and the environment. Many attempts have been made to replace Pb with nontoxic elements;

however, the resulting perovskites perform poorly compared to Pb-based perovskites. There are several reports about all-inorganic perovskite nanoplates showing their potential for optical information processing and advance bionic science research. This also paves the way for the future realization of neuromorphic vision and recognition. Similarly, the multifunction e-skin with mechanoreceptor and photomemory and mimicking human skin is of great interest for future research.

3.6 Current Focus and Challenges of LD Perovskites-based Solar Cell

Despite the rapidly increasing industrial attentiveness in hybrid PSC, their commercialization is restricted to some main issues. One of the most prominent issues is device stability, an unstable device with short lifetimes is not capable to compete with the PV market requirements. The main focus of researchers is to define some basic standardized parameters for solar cell stability testing and overcome these stability issues as soon as possible to make it a commercially available device [329]. Perovskites are considered a new material in photovoltaics; they need a lot of exploratory research to make them a strong competitor in this field. Researchers are working to increase their efficiencies by optimizing the efficiency-reducing defects by altering the synthesis mechanisms correspondingly [259].

Although PSC attained rapid potential, several issues remain to be solved on an urgent basis to make them alternative to conventional PV technologies. The most critical hurdle is the very weak moisture resistance, which leads to rapid degradation of the device. Various groups are working to make a permanent solution for instability, which includes polymer-based coatings etc. Also, the presence of toxic lead in perovskite makes them environment unfriendly. Tin is used as an alternative for lead, but it has lower reported efficiencies. The addition of a new DJ phase with 13.3% cell efficiency and tremendous device stability has opened a new era of research [259, 330]. Even in extreme conditions, such as ambient air (40–70 percent relative humidity [RH]) for 4,000 h, damp heat (85 °C and 85 percent RH) for 168 h, and continuous light irradiation for 3,000 h, unencapsulated devices retain over 95 percent efficiency. This ultrahigh device stability is achieved by alternating hydrogen bonding interactions between diammonium cations and inorganic slabs, which supports the 2D layered perovskite structure [259]. Perovskite solar cells could also be used in high-performance tandem device topologies that efficiently convert ultraviolet and visible light into electricity. An additional advantage of perovskite materials is their tunable bandgap, which complement the absorption of their partner material. This can boost their efficiency and reduce costs for commercialization. The last milestone of PV is the investigation and optimization of fabrication processes [331]. A scalable and reproducible production method can be adopted and perovskite PV modules potentially exceed the office's levelized cost of electricity (LCOE) targets [332].

One of the main challenges in LD perovskites is the photocurrent collection, which is limited due to electric field-assisted electron–hole pair separation and transport across the organic barriers. Also, the absorber layer thickness is limited to 200 nm, allowing for improved absorption and very effective photogenerated carrier separation and transport [333]. Controlling doping concentration in LD perovskites is difficult when it comes to determining the charge carrier, defect density, and band alignment in device functioning. The self-doping of single crystals of $PEA_2PbI_4(MAPbI_3)n1$ (n = 1, 2, 3) has recently been examined as a representative application. In prototypal 2D perovskites, the femtosecond transient absorption spectroscopy is used to explore the exciton–exciton interactions by using pump-probe methods [334].

In a very short period, LD perovskites have become the alternative to 3D perovskites with better stability PSCs. Still, improving the stability of LD perovskite against moisture and air and exploring their usage in efficient and stable PSCs are the main motivation in the PV field. Although there are some improvements in LD perovskite behavior, still some crucial aspects need to be solved on a priority basis for the development of efficient commercial PSC. To accomplish well-aligned LD perovskites growth and improve the charge-transport mechanism in these materials, the next significant challenge is to establish perfect control of the material structure and thin-film morphology. Applying LD perovskite layers as barriers against water diffusion into PSCs has shown significant improvement in device stability, but improving the device efficiency is still challenging in this architecture. Cost-effective and simple synthesis methods

of LD perovskites make them prominent as compared to 3D perovskite-based solar cells.

3.7 Prospectives of LD perovskite-based LEDs

LDPs are viable contenders for the next-generation display technologies with low fabrication cost, outstanding luminous properties, including high color purity, adjustable emission wavelength, and high PLQY. External quantum efficiencies of more than 25% have been attained by green, red, and near-infrared perovskite LEDs throughout the last ten years [302]. Low-dimensional perovskites, primarily Cs_4PbBr_6, have lately made a comeback in a variety of nanocrystal and single-crystal forms as materials with characteristics that connect inorganic semiconductors with organic molecules. In addition to exceptional green photoluminescence with enhanced stability and high quantum yield, these characteristics include spontaneous Pb^{2+} ion emission, a significant exciton binding energy, and a tiny polaron generation following photoexcitation. The presentation of light-emitting diode devices based on Cs_4PbBr_6 also encourages more research into these novel materials and emphasizes the rapid efforts toward their applications as well as highlighting the development of Cs_4PbBr_6 perovskites, with particular attention to their molecular–electronic characteristics and the contentious green photoluminescence.

For many years, low-dimensional perovskite has been widely recognized yet because of 3D perovskite's exceptional power conversion efficiency; low-dimensional perovskites have received less attention. These materials can be synthesized utilizing a variety of organic barriers, which opens an entirely unique class of fascinating materials with enormous optoelectronic potential applications [335]. They have greater potential for LEDs than 3D counterparts because the 3D structure is constrained by the elements that can be altered in the perovskite structure, including the metal, the halide, and the small organic cation (typically methylammonium). Low-dimensional perovskite can employ organic barriers with a variety of configurations, including double bonds, aromatic rings, and chain lengths, to provide a range of optical, structural, and electrical characteristics. Additionally, low-dimensional perovskite is a major focus of future electro-luminance research because of its superior defect tolerances, adjustable emissions, exceptional purity, and enhanced stability, particularly in the presence of moisture and ultraviolet radiation.

3.8 Current Status and Future Potential of LFHPs

Although lead-based perovskites continue to be the industry standard for efficiency in photovoltaics, with power conversion efficiencies (PCEs) in perovskite/silicon tandem systems above 33% [336], LFHPs have become a viable and environmentally beneficial option with unique benefits. Three basic LFHP restrictions are the main cause of the performance difference between these material systems: (1) Sn-based perovskites with deep-level defects localized 0.3–0.5 eV below the conduction band [337], (2) adverse band alignment at interfaces for charge transfer [338], (3) much reduced carrier mobilities (less than 10 cm^2 V^{-1} s^{-1} as opposed to more than 100 cm^2 V^{-1} s^{-1} in their lead-based equivalents) [339].

In tackling these issues, recent developments in two-dimensional (2D) LFHPs show impressive success. However, butylammonium copper chloride (BA_2CuCl_4) has exceptional heat stability up to 200 °C [340], while phenylethyl ammonium tin iodide (($PEA)_2SnI_4$) demonstrates both remarkable moisture stability (> 1,000 h at 85% relative humidity) and strong photoluminescence quantum yield (PLQY = 82%) [341]. Double perovskite $Cs_2AgBiBr_6$ meets or surpasses 10^{13} Jones in specific detectivity in photodetector applications, competing with silicon-based commercial devices [110].

The performance of the LFHP device may be enhanced using three main strategies. With Sn^{2+}/Ge^{2+} alloying in $CsSn_{0.5}Ge_{0.5}I_3$ which reduces trap density by 40% [342] and Mn^{2+} doping in $Cs_2AgInCl_6$ that increases PLQY from 35% to 86% [343], compositional engineering through cation substitution has shown notable improvements. Another key strategy is dimensional control, where 0D $Cs_3Cu_2I_5$ exhibits pure blue emission (CIE coordinates 0.16, 0.07) with 95% PLQY [344] and quasi-2D $(GA)(MA)_3Pb_4I_{13}$ achieves 18.5% PCE with improved stability [345]. With atomic layer deposition of Al_2O_3 increasing device lifetime (T80) to 1,500 h under extreme environmental conditions (85 °C/85% RH) [346] and phenethyl ammonium iodide (PEAI) treatment minimizing interfacial recombination by 60%, interface engineering via surface passivation and encapsulation proved equally important.

Low-dimensional LFHPs have special qualities that make them ideal for applications involving visual perception. In display technologies, 2D $(PEA)_2PbI_4$ allows for polarized light-emitting diodes (LEDs) with remarkable anisotropy ratios that surpass 100:1 [347], while 0D $Cs_3Cu_2I_5$ is a powerful scintillator with light yields that reach 45,000 photons/MeV for X-ray imaging [90]. Emerging applications in AR/VR take use of the ultra-thin (< 100 nm) form factor that 2D perovskite micro-displays may achieve [348], while biomedical applications use $Cs_2AgBiBr_6$'s biocompatibility to produce implanted sensors [349]. These developments demonstrate how LFHPs have the potential to open new technological possibilities that are not possible with lead-based perovskites.

Moving forward, the development of LFHPs should focus on three main areas: (1) establishing robust performance comparisons through universal stability testing protocols [350], (2) building extensive structure–property databases using high-throughput screening techniques [351], and (3) developing scalable manufacturing methods like roll-to-roll processing and inkjet printing [153]. The environmental benefits and distinctive characteristics of LFHPs make them attractive substitutes for particular applications where sustainability and safety are crucial, even if there are still difficulties in matching the peak performance of lead-based perovskites.

4 Summary and Outlook

The rapidly increasing demand for low-dimensional materials in smart optoelectronics has driven extensive efforts to make these materials both industrially feasible and beneficial for improving human quality of life. This demand aligns with the growing interest in portable, lightweight, low-cost, flexible, and wearable electronics. Addressing these challenges is crucial for the development of next-generation electronic devices, representing significant technological advancements in performance characteristics and a wide range of potential applications.

In this review article, we have included a list of modern fabrication processes as well as some notable applications, such as synapse, memory, photodetectors, photovoltaics, and light-emitting devices. Many new opportunities need to be addressed. Recently, there is a significant improvement in the research about low-dimensional perovskites in terms of material synthesis, stability, photonic and optoelectronic application in the last few years, but there is plenty of room available for new prospects and questions to be addressed.

1.Although there is a tremendous achievement in the fabrication techniques of LD perovskites with controlled shape and sizes as compared with conventional semiconductors, it is still very challenging.

2.LD perovskites are also continuously expanding with discoveries and inventions. For future uses of high-quality perovskite NCs, more research is needed to make them compatible with currently existing nano-fabrication synthesis processes.

3.Regardless of the immense utilization of LD perovskites in several aspects, the criticism for better stability toward heat, moisture, and polar solvent with weak metal–halide bond, to achieve complete control over thin-film morphology, and their ionic nature is still challenging.

4.The fabrication techniques including surface passivation, element alteration, and physical encapsulation are widely used to make environmentally stable devices, but these strategies are limiting the performance of the devices. As a result, enhanced stability and better performance are critical for future perovskite-based devices to be commercialized.

In conclusion, LD perovskites with better tunability, ease of manufacturing, and outstanding structural properties are intriguing prospects for future electrical and optoelectronic applications.

Declarations

References

1. Y. Koo, T. Moon, M. Kang, H. Joo, C. Lee et al., Dynamical control of nanoscale light-matter interactions in low-dimensional quantum materials. Light Sci. Appl. **13**(1), 30 (2024). https://doi.org/10.1038/s41377-024-01380-x

2. B.H. Alshammari, M.M.A. Lashin, M.A. Mahmood, F.S. Al-Mubaddel, N. Ilyas et al., Organic and inorganic nanomaterials: fabrication, properties and applications. RSC Adv. **13**(20), 13735–13785 (2023). https://doi.org/10.1039/D3RA01421E

3. Y. Xia, P. Yang, Y. Sun, Y. Wu, B. Mayers et al., One-dimensional nanostructures: synthesis, characterization, and applications. Adv. Mater. **15**(5), 353–389 (2003). https://doi.org/10.1002/adma.200390087

4. A. Zhang, C.M. Lieber, Nano-bioelectronics. Chem. Rev. **116**(1), 215–257 (2016). https://doi.org/10.1021/acs.chemrev.5b00608

5. R. Yan, D. Gargas, P. Yang, Nanowire photonics. Nat. Photonics **3**(10), 569–576 (2009). https://doi.org/10.1038/nphoton.2009.184

6. Q. Han, J. Wang, S. Tian, S. Hu, X. Wu et al., Inorganic perovskite-based active multifunctional integrated photonic devices. Nat. Commun. **15**(1), 1536 (2024). https://doi.org/10.1038/s41467-024-45565-9

7. X. Xu, S. Liu, Y. Kuai, Y. Jiang, Z. Hu et al., Laser fabrication of multi-dimensional perovskite patterns with intelligent anti-counterfeiting applications. Adv. Sci. **11**(42), 2309862 (2024). https://doi.org/10.1002/advs.202309862

8. A. Ravilla, C.A.R. Perini, J.-P. Correa-Baena, A.W.Y. Ho-Baillie, I. Celik, Life cycle assessment of low-dimensional materials for perovskite photovoltaic cells. Energy Adv. **3**(4), 800–811 (2024). https://doi.org/10.1039/D3YA00540B

9. F. Ye, T. Tian, J. Su, R. Jiang, J. Li et al., Tailoring low-dimensional perovskites passivation for efficient two-step-processed FAPbI3 solar cells and modules. Adv. Energy Mater. **14**(4), 2302775 (2024). https://doi.org/10.1002/aenm.202302775

10. M. Li, J. Wang, J. Yao, S. Wang, L. Xu et al., Trade-off between efficiency and stability of CsPbBr$_3$ perovskite quantum dot-based light-emitting diodes by optimized passivation ligands for Br/Pb. Adv. Funct. Mater. **34**(3), 2308341 (2024). https://doi.org/10.1002/adfm.202308341

11. S. Aftab, G. Koyyada, Z. Haider, E. Akman, F. Kabir et al., From lab to luminescence: Perovskite-based dimensional integrations pushing LED boundaries. Mater. Today Phys. **46**, 101490 (2024). https://doi.org/10.1016/j.mtphys.2024.101490

12. H. Dong, C. Ran, W. Gao, M. Li, Y. Xia et al., Metal halide perovskite for next-generation optoelectronics: progresses and prospects. eLight **3**(1), 3 (2023). https://doi.org/10.1186/s43593-022-00033-z

13. K. M. Salim, S. Masi, A. F. Gualdrón-Reyes, R. S. Sánchez, E. M. Barea, M. Krećmarová, J. F. Sánchez-Royo, I. n. Mora-Seró. Boosting long-term stability of pure formamidinium perovskite solar cells by ambient air additive assisted fabrication. ACS Energy Lett. **6**, 3511–3521 (2021). https://pubs.acs.org/doi/https://doi.org/10.1021/acsenergylett.1c01311

14. H. Liu, H. Zhou, Repair strategies for perovskite solar cells. Chem. Res. Chin. Univ. **37**(5), 1055–1066 (2021). https://doi.org/10.1007/s40242-021-1334-9

15. K. Tanaka, T. Takahashi, T. Kondo, T. Umebayashi, K. Asai et al., Image charge effect on two-dimensional excitons in an inorganic-organic quantum-well crystal. Phys. Rev. B **71**(4), 045312 (2005). https://doi.org/10.1103/PhysRevB.71.045312

16. W. Chen, F. Zhang, C. Wang, M. Jia, X. Zhao et al., Nonlinear photonics using low-dimensional metal-halide perovskites: recent advances and future challenges. Adv. Mater. **33**(11), 2004446 (2021). https://doi.org/10.1002/adma.202004446

17. T.W. Kasel, Electronic structure perturbations of perovskite material: Photovoltaic applications (Ph.D thesis of University of Oregon, 2020).

18. K. Chondroudis, D.B. Mitzi, Electroluminescence from an organic–inorganic perovskite incorporating a quaterthiophene dye within lead halide perovskite layers. Chem. Mater. **11**(11), 3028–3030 (1999). https://doi.org/10.1021/cm990561t

19. E.R. Dohner, A. Jaffe, L.R. Bradshaw, H.I. Karunadasa, Intrinsic white-light emission from layered hybrid perovskites. J. Am. Chem. Soc. **136**(38), 13154–13157 (2014). https://doi.org/10.1021/ja507086b

20. C.R. Kagan, D.B. Mitzi, C.D. Dimitrakopoulos, Organic-inorganic hybrid materials as semiconducting channels in thin-film field-effect transistors. Science **286**(5441), 945–947 (1999). https://doi.org/10.1126/science.286.5441.945

21. W. Ahmad, Y. Gong, G. Abbas, K. Khan, M. Khan et al., Evolution of low-dimensional material-based field-effect transistors. Nanoscale **13**(10), 5162–5186 (2021). https://doi.org/10.1039/d0nr07548e

22. Z. Tan, Y. Wu, H. Hong, J. Yin, J. Zhang et al., Two-dimensional $(C_4H_9NH_3)_2PbBr_4$ perovskite crystals for high-performance photodetector. J. Am. Chem. Soc. **138**(51), 16612–16615 (2016). https://doi.org/10.1021/jacs.6b11683

23. G. Zhou, R. Sun, Y. Xiao, G. Abbas, Z. Peng, A high-performance flexible broadband photodetector based on graphene–PTAA–perovskite heterojunctions. Adv. Electron. Mater. **7**(3), 2000522 (2021). https://doi.org/10.1002/aelm.202000522

24. X. Zhang, G. Wu, S. Yang, W. Fu, Z. Zhang et al., Vertically oriented 2D layered perovskite solar cells with enhanced efficiency and good stability. Small **13**(33), 1700611 (2017). https://doi.org/10.1002/smll.201700611

25. P. Chen, Y. Bai, M. Lyu, J.-H. Yun, M. Hao et al., Progress and perspective in low-dimensional metal halide perovskites for optoelectronic applications. Sol. RRL **2**(3), 1700186 (2018). https://doi.org/10.1002/solr.201700186

26. G.E. Eperon, V.M. Burlakov, A. Goriely, H.J. Snaith, Neutral color semitransparent microstructured perovskite solar cells. ACS Nano **8**(1), 591–598 (2014). https://doi.org/10.1021/nn4052309

27. J. Song, L. Xu, J. Li, J. Xue, Y. Dong et al., Monolayer and few-layer all-inorganic perovskites as a new family of two-dimensional semiconductors for printable optoelectronic devices. Adv. Mater. **28**(24), 4861–4869 (2016). https://doi.org/10.1002/adma.201600225

28. C. Lee, S.J. Lee, Y. Shin, Y. Woo, S.-H. Han et al., Synthetic and post-synthetic strategies to improve photoluminescence quantum yields in perovskite quantum dots. Catalysts **11**(8), 957 (2021). https://doi.org/10.3390/catal11080957

29. Y. Liu, S. Bose, W. Fan, Effect of size and shape on electronic and optical properties of CdSe quantum dots. Optik **155**, 242–250 (2018). https://doi.org/10.1016/j.ijleo.2017.10.165

30. X. Fang, W. Zhai, K. Zhang, Y. Wang, L. Yao et al., Wide range tuning of the size and emission color of $CH_3NH_3PbBr_3$ quantum dots by surface ligands. AIP Adv. **7**(8), 085217 (2017). https://doi.org/10.1063/1.4994995

31. S. Parveen, K.K. Paul, R. Das, P.K. Giri, Large exciton binding energy, high photoluminescence quantum yield and improved photostability of organo-metal halide hybrid perovskite quantum dots grown on a mesoporous titanium dioxide template. J. Colloid Interface Sci. **539**, 619–633 (2019). https://doi.org/10.1016/j.jcis.2018.12.105

32. X.-F. Hu, C.-G. Lu, Q. Wang, J.-K. Xu, Y.-P. Cui, A high-precision, template-assisted, anisotropic wet etching method for fabricating perovskite microstructure arrays. RSC Adv. **10**(63), 38220–38226 (2020). https://doi.org/10.1039/D0RA07228A

33. S. Wang, C. Bi, J. Yuan, L. Zhang, J. Tian, Original core–shell structure of cubic $CsPbBr_3$@amorphous $CsPbBr_x$ perovskite quantum dots with a high blue photoluminescence quantum yield of over 80%. ACS Energy Lett. **3**(1), 245–251 (2018). https://doi.org/10.1021/acsenergylett.7b01243

34. Y. Yang, S. Wei, X. Kang, O. Tegus, D. Pan, Short-chain ligand assisted synthesis of $CH_3NH_3PbX_3$ (X = Cl, Br, I) perovskite quantum dots and improved morphology of $CH_3NH_3PbBr_3$ thin films. J. Lumin. **211**, 26–31 (2019). https://doi.org/10.1016/j.jlumin.2019.03.018

35. C. Zhou, H. Lin, Y. Tian, Z. Yuan, R. Clark et al., Luminescent zero-dimensional organic metal halide hybrids with near-unity quantum efficiency. Chem. Sci. **9**(3), 586–593 (2018). https://doi.org/10.1039/c7sc04539e

36. C. Zhou, Y. Tian, M. Wang, A. Rose, T. Besara et al., Low-dimensional organic tin bromide perovskites and their photoinduced structural transformation. Angew. Chem. Int. Ed. **56**(31), 9018–9022 (2017). https://doi.org/10.1002/anie.201702825

37. J. Li, P. Dwivedi, K.S. Kumar, T. Roy, K.E. Crawford et al., Growing perovskite quantum dots on carbon nanotubes for neuromorphic optoelectronic computing. Adv. Electron. Mater. **7**(1), 2000535 (2021). https://doi.org/10.1002/aelm.202000535

38. J. Guo, Q. Hu, M. Lu, A. Li, X. Zhang et al., Pb^{2+} doped $CsCdBr_3$ perovskite nanorods for pure-blue light-emitting diodes. Chem. Eng. J. **427**, 131010 (2022). https://doi.org/10.1016/j.cej.2021.131010

39. W. Zhang, M. Hong, J. Luo, Centimeter-sized single crystal of a one-dimensional lead-free mixed-cation perovskite ferroelectric for highly polarization sensitive photodetection. J. Am. Chem. Soc. **143**(40), 16758–16767 (2021). https://doi.org/10.1021/jacs.1c08281

40. M.M. Rahman, C.-Y. Ge, K. Yoo, J.-J. Lee, Aqueous phase synthesis of trimethylsulfoxonium lead triiodide for moisture-stable perovskite solar cells. Mater. Today Energy **21**, 100803 (2021). https://doi.org/10.1016/j.mtener.2021.100803

41. Y. Liang, F. Li, R. Zheng, Low-dimensional hybrid perovskites for field-effect transistors with improved stability: progress and challenges. Adv. Electron. Mater. **6**(9), 2000137 (2020). https://doi.org/10.1002/aelm.202000137

42. D. Yao, M.T. Hoang, H. Wang, Low-dimensional-networked perovskites with A-site-cation engineering for optoelectronic devices. Small Meth. **5**(5), 2001147 (2021). https://doi.org/10.1002/smtd.202001147

43. Z. Chu, X. Chu, Y. Zhao, Q. Ye, J. Jiang et al., Emerging low-dimensional crystal structure of metal halide perovskite optoelectronic materials and devices. Small Struct. **2**(6), 2000133 (2021). https://doi.org/10.1002/sstr.202000133

44. Z. Ma, F. Li, L. Sui, Y. Shi, R. Fu et al., Tunable color temperatures and emission enhancement in 1D halide perovskites under high pressure. Adv. Opt. Mater. **8**(18), 2000713 (2020). https://doi.org/10.1002/adom.202000713

45. A. Ishii, T. Miyasaka, Direct detection of circular polarized light in helical 1D perovskite-based photodiode. Sci. Adv. **6**(46), eabd3274 (2020). https://doi.org/10.1126/sciadv.abd3274

46. S.K. Vishwanath, B. Febriansyah, S.E. Ng, T. Das, J. Acharya et al., Correction: High-performance one-dimensional halide perovskite crossbar memristors and synapses for neuromorphic computing. Mater. Horiz. **11**(18), 4519–4519 (2024). https://doi.org/10.1039/D4MH90073A

47. Z. Yuan, C. Zhou, Y. Tian, Y. Shu, J. Messier et al., One-dimensional organic lead halide perovskites with efficient bluish white-light emission. Nat. Commun. **8**, 14051 (2017). https://doi.org/10.1038/ncomms14051

48. X. Xu, X. Zhang, W. Deng, J. Jie, X. Zhang, 1D organic–inorganic hybrid perovskite micro/nanocrystals: fabrication, assembly, and optoelectronic applications. Small Meth. **2**(7), 1700340 (2018). https://doi.org/10.1002/smtd.201700340

49. S.-X. Li, Y.-S. Xu, C.-L. Li, Q. Guo, G. Wang et al., Perovskite single-crystal microwire-array photodetectors with performance stability beyond 1 year. Adv. Mater. **32**(28), e2001998 (2020). https://doi.org/10.1002/adma.202001998

50. Y. Wang, X. Liu, Q. He, G. Chen, D. Xu et al., Reversible transformation between CsPbBr$_3$ perovskite nanowires and nanorods with polarized optoelectronic properties. Adv. Funct. Mater. **31**(22), 2011251 (2021). https://doi.org/10.1002/adfm.202011251

51. L. Gu, S. Poddar, Y. Lin, Z. Long, D. Zhang et al., A biomimetic eye with a hemispherical perovskite nanowire array retina. Nature **581**(7808), 278–282 (2020). https://doi.org/10.1038/s41586-020-2285-x

52. J.A. Sichert, Y. Tong, N. Mutz, M. Vollmer, S. Fischer et al., Quantum size effect in organometal halide perovskite nanoplatelets. Nano Lett. **15**(10), 6521–6527 (2015). https://doi.org/10.1021/acs.nanolett.5b02985

53. S. Ahmad, X. Guo, Rapid development in two-dimensional layered perovskite materials and their application in solar cells. Chin. Chem. Lett. **29**(5), 657–663 (2018). https://doi.org/10.1016/j.cclet.2017.08.057

54. H. Huang, A.S. Susha, S.V. Kershaw, T.F. Hung, A.L. Rogach, Control of emission color of high quantum yield CH$_3$NH$_3$PbBr$_3$ perovskite quantum dots by precipitation temperature. Adv. Sci. **2**(9), 1500194 (2015). https://doi.org/10.1002/advs.201500194

55. K.C. Kwon, K.S. Choi, S.Y. Kim, Increased work function in few-layer graphene sheets *via* metal chloride doping. Adv. Funct. Mater. **22**(22), 4724–4731 (2012). https://doi.org/10.1002/adfm.201200997

56. K.T. Nam, S.A. Shelby, P.H. Choi, A.B. Marciel, R. Chen et al., Free-floating ultrathin two-dimensional crystals from sequence-specific peptoid polymers. Nat. Mater. **9**(5), 454–460 (2010). https://doi.org/10.1038/nmat2742

57. G. Grancini, M.K. Nazeeruddin, Dimensional tailoring of hybrid perovskites for photovoltaics. Nat. Rev. Mater. **4**(1), 4–22 (2018). https://doi.org/10.1038/s41578-018-0065-0

58. M. Braun, W. Tuffentsammer, H. Wachtel, H.C. Wolf, Tailoring of energy levels in lead chloride based layered perovskites and energy transfer between the organic and inorganic planes. Chem. Phys. Lett. **303**(1–2), 157–164 (1999). https://doi.org/10.1016/S0009-2614(99)00205-5

59. R. Younts, H.-S. Duan, B. Gautam, B. Saparov, J. Liu et al., Efficient generation of long-lived triplet excitons in 2D hybrid perovskite. Adv. Mater. **29**(9), 1604278 (2017). https://doi.org/10.1002/adma.201604278

60. A. Fraccarollo, A. Zoccante, L. Marchese, M. Cossi, *Ab initio* modeling of 2D and quasi-2D lead organohalide perovskites with divalent organic cations and a tunable band gap. Phys. Chem. Chem. Phys. **22**(36), 20573–20587 (2020). https://doi.org/10.1039/c9cp06851a

61. X. Li, F. Cao, D. Yu, J. Chen, Z. Sun et al., All inorganic halide perovskites nanosystem: synthesis, structural features, optical properties and optoelectronic applications. Small **13**(9). 1603996 (2017). https://doi.org/10.1002/smll.201603996

62. D.B. Mitzi, Templating and structural engineering in organic–inorganic perovskites. J. Chem. Soc., Dalton Trans. **1**, 1–12 (2001). https://doi.org/10.1039/b007070j

63. J. Zhuang, P. Mao, Y. Luan, X. Yi, Z. Tu et al., Interfacial passivation for perovskite solar cells: the effects of the functional group in phenethylammonium iodide. ACS Energy Lett. **4**(12), 2913–2921 (2019). https://doi.org/10.1021/acsenergylett.9b02375

64. F. Yang, P. Zhang, M.A. Kamarudin, G. Kapil, T. Ma et al., Addition effect of pyreneammonium iodide to methylammonium lead halide perovskite-2D/3D heterostructured perovskite with enhanced stability. Adv. Funct. Mater. **28**(46), 1804856 (2018). https://doi.org/10.1002/adfm.201804856

65. M.J. Brites, M.A. Barreiros, V. Corregidor, L.C. Alves, J.V. Pinto et al., Ultrafast low-temperature crystallization of solar cell graded formamidinium-cesium mixed-cation lead mixed-halide perovskites using a reproducible microwave-based process. ACS Appl. Energy Mater. **2**(3), 1844–1853 (2019). https://doi.org/10.1021/acsaem.8b02005

66. Y. Chen, Y. Sun, J. Peng, W. Zhang, X. Su et al., Tailoring organic cation of 2D air-stable organometal halide perovskites for highly efficient planar solar cells. Adv. Energy Mater. **7**(18), 1700162 (2017). https://doi.org/10.1002/aenm.201700162

67. J. Byun, H. Cho, C. Wolf, M. Jang, A. Sadhanala et al., Efficient visible quasi-2D perovskite light-emitting diodes. Adv. Mater. **28**(34), 7515–7520 (2016). https://doi.org/10.1002/adma.201601369

68. B.-E. Cohen, M. Wierzbowska, L. Etgar, High efficiency and high open circuit voltage in quasi 2D perovskite based solar cells. Adv. Funct. Mater. **27**(5), 1604733 (2017). https://doi.org/10.1002/adfm.201604733

69. X. Gan, O. Wang, K. Liu, X. Du, L. Guo et al., 2D homologous organic-inorganic hybrids as light-absorbers for planer

and nanorod-based perovskite solar cells. Sol. Energy Mater. Sol. Cells **162**, 93–102 (2017). https://doi.org/10.1016/j.solmat.2016.12.047

70. C. Ortiz-Cervantes, P. Carmona-Monroy, D. Solis-Ibarra, Two-dimensional halide perovskites in solar cells: 2D or not 2D? Chemsuschem **12**(8), 1560–1575 (2019). https://doi.org/10.1002/cssc.201802992

71. T.M. Koh, V. Shanmugam, J. Schlipf, L. Oesinghaus, P. Müller-Buschbaum et al., Nanostructuring mixed-dimensional perovskites: a route toward tunable, efficient photovoltaics. Adv. Mater. **28**(19), 3653–3661 (2016). https://doi.org/10.1002/adma.201506141

72. T. Ishihara, Optical properties of PbI-based perovskite structures. J. Lumin. **60**, 269–274 (1994). https://doi.org/10.1016/0022-2313(94)90145-7

73. D.B. Mitzi, S. Wang, C.A. Feild, C.A. Chess, A.M. Guloy, Conducting layered organic-inorganic halides containing 〈110〉-oriented perovskite sheets. Science **267**(5203), 1473–1476 (1995). https://doi.org/10.1126/science.267.5203.1473

74. A. Kojima, K. Teshima, Y. Shirai, T. Miyasaka, Organometal halide perovskites as visible-light sensitizers for photovoltaic cells. J. Am. Chem. Soc. **131**(17), 6050–6051 (2009). https://doi.org/10.1021/ja809598r

75. S. Gharibzadeh, I.M. Hossain, P. Fassl, B.A. Nejand, T. Abzieher et al., 2D/3D heterostructure for semitransparent perovskite solar cells with engineered bandgap enables efficiencies exceeding 25% in four-terminal tandems with silicon and CIGS. Adv. Funct. Mater. **30**(19), 1909919 (2020). https://doi.org/10.1002/adfm.201909919

76. Z.-K. Tan, R.S. Moghaddam, M.L. Lai, P. Docampo, R. Higler et al., Bright light-emitting diodes based on organometal halide perovskite. Nat. Nanotechnol. **9**(9), 687–692 (2014). https://doi.org/10.1038/nnano.2014.149

77. P. Tyagi, S.M. Arveson, W.A. Tisdale, Colloidal organohalide perovskite nanoplatelets exhibiting quantum confinement. J. Phys. Chem. Lett. **6**(10), 1911–1916 (2015). https://doi.org/10.1021/acs.jpclett.5b00664

78. Z. Yuan, Y. Shu, Y. Xin, B. Ma, Highly luminescent nanoscale quasi-2D layered lead bromide perovskites with tunable emissions. Chem. Commun. **52**(20), 3887–3890 (2016). https://doi.org/10.1039/C5CC09762B

79. S.T. Ha, X. Liu, Q. Zhang, D. Giovanni, T.C. Sum et al., Synthesis of organic–inorganic lead halide perovskite nanoplatelets: towards high-performance perovskite solar cells and optoelectronic devices. Adv. Opt. Mater. **2**(9), 838–844 (2014). https://doi.org/10.1002/adom.201400106

80. J.H. Han, S. Lee, J. Cheon, Synthesis and structural transformations of colloidal 2D layered metal chalcogenide nanocrystals. Chem. Soc. Rev. **42**(7), 2581–2591 (2013). https://doi.org/10.1039/C2CS35386E

81. Y. Bekenstein, B.A. Koscher, S.W. Eaton, P. Yang, A.P. Alivisatos, Highly luminescent colloidal nanoplates of perovskite cesium lead halide and their oriented assemblies. J. Am. Chem. Soc. **137**(51), 16008–16011 (2015). https://doi.org/10.1021/jacs.5b11199

82. B.A. Koscher, N.D. Bronstein, J.H. Olshansky, Y. Bekenstein, A.P. Alivisatos, Surface- vs diffusion-limited mechanisms of anion exchange in CsPbBr$_3$ nanocrystal cubes revealed through kinetic studies. J. Am. Chem. Soc. **138**(37), 12065–12068 (2016). https://doi.org/10.1021/jacs.6b08178

83. J. Liu, K. Chen, S.A. Khan, B. Shabbir, Y. Zhang et al., Synthesis and optical applications of low dimensional metal-halide perovskites. Nanotechnology **31**(15), 152002 (2020). https://doi.org/10.1088/1361-6528/ab5a19

84. S. Panigrahi, S. Jana, T. Calmeiro, D. Nunes, R. Martins et al., Imaging the anomalous charge distribution inside CsPbBr$_3$ perovskite quantum dots sensitized solar cells. ACS Nano **11**(10), 10214–10221 (2017). https://doi.org/10.1021/acsnano.7b04762

85. B.-E. Cohen, Y. Li, Q. Meng, L. Etgar, *Dion*-jacobson two-dimensional perovskite solar cells based on benzene dimethanammonium cation. Nano Lett. **19**(4), 2588–2597 (2019). https://doi.org/10.1021/acs.nanolett.9b00387

86. J. Gong, M. Hao, Y. Zhang, M. Liu, Y. Zhou, Layered 2D halide perovskites beyond the ruddlesden-popper phase: tailored interlayer chemistries for high-performance solar cells. Angew. Chem. Int. Ed. **61**(10), e202112022 (2022). https://doi.org/10.1002/anie.202112022

87. E. Oksenberg, E. Sanders, R. Popovitz-Biro, L. Houben, E. Joselevich, Surface-guided CsPbBr$_3$ perovskite nanowires on flat and faceted sapphire with size-dependent photoluminescence and fast photoconductive response. Nano Lett. **18**(1), 424–433 (2018). https://doi.org/10.1021/acs.nanolett.7b04310

88. H.-P. Wang, S. Li, X. Liu, Z. Shi, X. Fang et al., Low-dimensional metal halide perovskite photodetectors. Adv. Mater. **33**(7), 2003309 (2021). https://doi.org/10.1002/adma.202003309

89. Y. Zhang, J. Liu, Z. Wang, Y. Xue, Q. Ou et al., Synthesis, properties, and optical applications of low-dimensional perovskites. Chem. Commun. **52**(94), 13637–13655 (2016). https://doi.org/10.1039/C6CC06425F

90. Q. Chen, J. Wu, X. Ou, B. Huang, J. Almutlaq et al., All-inorganic perovskite nanocrystal scintillators. Nature **561**(7721), 88–93 (2018). https://doi.org/10.1038/s41586-018-0451-1

91. N. Nishimura, M. Tojo, Y. Takeoka, Simple one-step synthesis of a two-dimensional perovskite consisting of perfluoroalkyl-based ammonium spacers using acetone as the solvent. Chem. Commun. **56**(71), 10293–10296 (2020). https://doi.org/10.1039/D0CC03874A

92. J. Chen, L. Gan, F. Zhuge, H. Li, J. Song et al., A ternary solvent method for large-sized two-dimensional perovskites. Angew. Chem. Int. Ed. **56**(9), 2390–2394 (2017). https://doi.org/10.1002/anie.201611794

93. I.M. Asuo, P. Fourmont, I. Ka, D. Gedamu, S. Bouzidi et al., Highly efficient and ultrasensitive large-area flexible photodetector based on perovskite nanowires. Small **15**(1), 1804150 (2019). https://doi.org/10.1002/smll.201804150

94. K. Yang, F. Li, Y. Liu, Z. Xu, Q. Li et al., All-solution-processed perovskite quantum dots light-emitting diodes based on the solvent engineering strategy. ACS Appl. Mater.

Interfaces **10**(32), 27374–27380 (2018). https://doi.org/10.1021/acsami.8b09702

95. J. Zhang, B. Wei, L. Wang, X. Yang, The solution-processed fabrication of perovskite light-emitting diodes for low-cost and commercial applications. J. Mater. Chem. C **9**(36), 12037–12045 (2021). https://doi.org/10.1039/d1tc03385a

96. J. Yuan, X. Zhang, J. Sun, R. Patterson, H. Yao et al., Hybrid perovskite quantum dot/non-fullerene molecule solar cells with efficiency over 15%. Adv. Funct. Mater. **31**(27), 2101272 (2021). https://doi.org/10.1002/adfm.202101272

97. D. Ghosh, M.Y. Ali, A. Ghosh, A. Mandal, S. Bhattacharyya, Heterovalent substitution in mixed halide perovskite quantum dots for improved and stable photovoltaic performance. J. Phys. Chem. C **125**(10), 5485–5493 (2021). https://doi.org/10.1021/acs.jpcc.0c11122

98. W.-C. Chen, Y.-H. Fang, L.-G. Chen, F.-C. Liang, Z.-L. Yan et al., High luminescence and external quantum efficiency in perovskite quantum-dots light-emitting diodes featuring bilateral affinity to silver and short alkyl ligands. Chem. Eng. J. **414**, 128866 (2021). https://doi.org/10.1016/j.cej.2021.128866

99. X. Liu, T. Ma, N. Pinna, J. Zhang, Two-dimensional nanostructured materials for gas sensing. Adv. Funct. Mater. **27**(37), 1702168 (2017). https://doi.org/10.1002/adfm.201702168

100. A. Waleed, M.M. Tavakoli, L. Gu, S. Hussain, D. Zhang et al., All inorganic cesium lead iodide perovskite nanowires with stabilized cubic phase at room temperature and nanowire array-based photodetectors. Nano Lett. **17**(8), 4951–4957 (2017). https://doi.org/10.1021/acs.nanolett.7b02101

101. J. Li, R. Gao, F. Gao, J. Lei, H. Wang et al., Fabrication of efficient CsPbBr$_3$ perovskite solar cells by single-source thermal evaporation. J. Alloys Compd. **818**, 152903 (2020). https://doi.org/10.1016/j.jallcom.2019.152903

102. Y. Wang, Y. Shi, G. Xin, J. Lian, J. Shi, Two-dimensional van der waals epitaxy kinetics in a three-dimensional perovskite halide. Cryst. Growth Des. **15**(10), 4741–4749 (2015). https://doi.org/10.1021/acs.cgd.5b00949

103. P. Li, B.N. Shivananju, Y. Zhang, S. Li, Q. Bao, High performance photodetector based on 2D CH$_3$NH$_3$PbI$_3$ perovskite nanosheets. J. Phys. D Appl. Phys. **50**(9), 094002 (2017). https://doi.org/10.1088/1361-6463/aa5623

104. M.M. Tavakoli, L. Gu, Y. Gao, C. Reckmeier, J. He et al., Fabrication of efficient planar perovskite solar cells using a one-step chemical vapor deposition method. Sci. Rep. **5**, 14083 (2015). https://doi.org/10.1038/srep14083

105. D. Ghoshal, T. Wang, H.-Z. Tsai, S.-W. Chang, M. Crommie et al., Catalyst-free and morphology-controlled growth of 2D perovskite nanowires for polarized light detection. Adv. Opt. Mater. **7**(15), 1900039 (2019). https://doi.org/10.1002/adom.201900039

106. Y. Xue, J. Yuan, J. Liu, S. Li, Controllable synthesis of 2D perovskite on different substrates and its application as photodetector. Nanomaterials **8**(8), 591 (2018). https://doi.org/10.3390/nano8080591

107. W. Zheng, X. Xiong, R. Lin, Z. Zhang, C. Xu et al., Balanced photodetection in one-step liquid-phase-synthesized CsPbBr$_3$ micro-/ nanoflake single crystals. ACS Appl. Mater. Interfaces **10**(2), 1865–1870 (2018). https://doi.org/10.1021/acsami.7b18093

108. J. Wang, C. Fang, J. Ma, S. Wang, L. Jin et al., Aqueous synthesis of low-dimensional lead halide perovskites for room-temperature circularly polarized light emission and detection. ACS Nano **13**(8), 9473–9481 (2019). https://doi.org/10.1021/acsnano.9b04437

109. G.L. Messing, S. Trolier-McKinstry, E.M. Sabolsky, C. Duran, S. Kwon et al., Templated grain growth of textured piezoelectric ceramics. Crit. Rev. Solid State Mater. Sci. **29**(2), 45–96 (2004). https://doi.org/10.1080/10408430490490905

110. A. Waleed, M.M. Tavakoli, L. Gu, Z. Wang, D. Zhang et al., Lead-free perovskite nanowire array photodetectors with drastically improved stability in nanoengineering templates. Nano Lett. **17**(1), 523–530 (2017). https://doi.org/10.1021/acs.nanolett.6b04587

111. D.N. Dirin, L. Protesescu, D. Trummer, I.V. Kochetygov, S. Yakunin et al., Harnessing defect-tolerance at the nanoscale: highly luminescent lead halide perovskite nanocrystals in mesoporous silica matrixes. Nano Lett. **16**(9), 5866–5874 (2016). https://doi.org/10.1021/acs.nanolett.6b02688

112. S. Zhuo, J. Zhang, Y. Shi, Y. Huang, B. Zhang, Self-template-directed synthesis of porous perovskite nanowires at room temperature for high-performance visible-light photodetectors. Angew. Chem. Int. Ed. **54**(19), 5693–5696 (2015). https://doi.org/10.1002/anie.201411956

113. L. Gu, D. Zhang, M. Kam, Q. Zhang, S. Poddar et al., Significantly improved black phase stability of FAPbI$_3$ nanowires *via* spatially confined vapor phase growth in nanoporous templates. Nanoscale **10**(32), 15164–15172 (2018). https://doi.org/10.1039/C8NR03058H

114. W. Deng, L. Huang, X. Xu, X. Zhang, X. Jin et al., Ultrahigh-responsivity photodetectors from perovskite nanowire arrays for sequentially tunable spectral measurement. Nano Lett. **17**(4), 2482–2489 (2017). https://doi.org/10.1021/acs.nanolett.7b00166

115. L. Gu, M.M. Tavakoli, D. Zhang, Q. Zhang, A. Waleed et al., 3D arrays of 1024-pixel image sensors based on lead halide perovskite nanowires. Adv. Mater. **28**(44), 9713–9721 (2016). https://doi.org/10.1002/adma.201601603

116. K. Wang, C. Wu, D. Yang, Y. Jiang, S. Priya, Quasi-two-dimensional halide perovskite single crystal photodetector. ACS Nano **12**(5), 4919–4929 (2018). https://doi.org/10.1021/acsnano.8b01999

117. Y. Liu, H. Ye, Y. Zhang, K. Zhao, Z. Yang et al., Surface-tension-controlled crystallization for high-quality 2D perovskite single crystals for ultrahigh photodetection. Matter **1**(2), 465–480 (2019). https://doi.org/10.1016/j.matt.2019.04.002

118. H. Tian, L. Zhao, X. Wang, Y.-W. Yeh, N. Yao et al., Extremely low operating current resistive memory based on exfoliated 2D perovskite single crystals for neuromorphic

computing. ACS Nano **11**(12), 12247–12256 (2017). https://doi.org/10.1021/acsnano.7b05726

119. H.L. Kagdada, B. Roondhe, V. Roondhe, S.D. Dabhi, W. Luo et al., Exploring A-site cation variations in *Dion*–jacobson two-dimensional halide perovskites for enhanced solar cell applications: a density functional theory study. Adv. Energy Sustain. Res. **5**(1), 2300147 (2024). https://doi.org/10.1002/aesr.202300147

120. Y. Dong, R. Zhu, Y. Jia, Linear relationship between the dielectric constant and band gap in low-dimensional mixed-halide perovskites. J. Phys. Chem. C **125**(27), 14883–14890 (2021). https://doi.org/10.1021/acs.jpcc.1c01576

121. M.S. Ozório, A.C. Dias, J.F.R.V. Silveira, J.L.F. Da Silva, Theoretical investigation of the role of anion and trivalent cation substitution in the physical properties of lead-free zero-dimensional perovskites. J. Phys. Chem. C **126**(16), 7245–7255 (2022). https://doi.org/10.1021/acs.jpcc.2c00494

122. H.T. Abdulla, A DFT approach on the investigations of the structural and optoelectronic properties of lead-free and Ge-based mixed halide perovskites $RbGeBr_2Cl$ and $RbGe_12Cl$. Indian J. Phys. **99**(3), 1041–1050 (2025). https://doi.org/10.1007/s12648-024-03354-6

123. M.U. Khandaker, H. Osman, S.A.M. Issa, M.M. Uddin, M.H. Ullah et al., Newly predicted halide perovskites Mg_3AB_3 (a = N, Bi; B = F, Br, I) for next-generation photovoltaic applications: a first-principles study. RSC Adv. **15**(8), 5766–5780 (2025). https://doi.org/10.1039/d4ra09093d

124. H. Beck, C. Gehrmann, D.A. Egger, Structure and binding in halide perovskites: analysis of static and dynamic effects from dispersion-corrected density functional theory. APL Mater. **7**(2), 021108 (2019). https://doi.org/10.1063/1.5086541

125. M.B. Fridriksson, S. Maheshwari, F.C. Grozema, Structural dynamics of two-dimensional ruddlesden–popper perovskites: a computational study. J. Phys. Chem. C **124**(40), 22096–22104 (2020). https://doi.org/10.1021/acs.jpcc.0c05225

126. R.C.B. Cedeno, J. Wei, Theoretical investigation of the mechanical properties of perovskite at various environmental factors change for application in solar cells proposed for green policy. Eng. Anal. Bound. Elem. **152**, 326–333 (2023). https://doi.org/10.1016/j.enganabound.2023.04.017

127. R. Lyu, C.E. Moore, T. Liu, Y. Yu, Y. Wu, Predictive design model for low-dimensional organic-inorganic halide perovskites assisted by machine learning. J. Am. Chem. Soc. **143**(32), 12766–12776 (2021). https://doi.org/10.1021/jacs.1c05441

128. W.A. Saidi, W. Shadid, I.E. Castelli, Machine-learning structural and electronic properties of metal halide perovskites using a hierarchical convolutional neural network. NPJ Comput. Mater. **6**, 36 (2020). https://doi.org/10.1038/s41524-020-0307-8

129. S. Yuan, Y. Liu, J. Lan, W. Yang, H. Xiong et al., Accurate dimension prediction for low-dimensional organic-inorganic halide perovskites *via* a self-established machine learning

130. C.-S. Hu, R. Mayengbam, M.-C. Wu, K. Xia, T.C. Sum, Geometric data analysis-based machine learning for two-dimensional perovskite design. Commun. Mater. **5**, 106 (2024). https://doi.org/10.1038/s43246-024-00545-w

131. M. A. Mahmud. Low-temperature processed perovskite solar cells. (2018) https://doi.org/10.26190/unsworks/3582

132. E. Calabrò, F. Matteocci, A.L. Palma, L. Vesce, B. Taheri et al., Low temperature, solution-processed perovskite solar cells and modules with an aperture area efficiency of 11%. Sol. Energy Mater. Sol. Cells **185**, 136–144 (2018). https://doi.org/10.1016/j.solmat.2018.05.001

133. M. Sharifi, R. Taheri Ghahrizjani, D. A. Amini, E. Mohajerani. Poling-assisted strategies for enhancing open-circuit voltage in highly sensitive, self-powered perovskite photodetector. Self-Powered Perovskite Photodetector. https://doi.org/10.2139/ssrn.5111215

134. Z. Xie, D. Liu, C. Gao, X. Zhang, H. Dong et al., High mobility emissive organic semiconductors for optoelectronic devices. J. Am. Chem. Soc. **147**(3), 2239–2256 (2025). https://doi.org/10.1021/jacs.4c11208

135. S.M. Hasnain, A. Iqbal, I. Qasim, K. Irshad, M.A. Mir et al., Performance evaluation of organomet halide MASnI3 and inorganic $BaZrS_3$ hybrids in perovskites solar cells: Theoretical approach. Hybrid Adv. **9**, 100408 (2025). https://doi.org/10.1016/j.hybadv.2025.100408

136. A. Hichri, S. Jaziri, M.O. Goerbig, Charged excitons in two-dimensional transition metal dichalcogenides: Semiclassical calculation of Berry curvature effects. Phys. Rev. B **100**(11), 115426 (2019). https://doi.org/10.1103/physrevb.100.115426

137. H. Wang, F.U. Kosasih, H. Yu, G. Zheng, J. Zhang et al., Perovskite-molecule composite thin films for efficient and stable light-emitting diodes. Nat. Commun. **11**(1), 891 (2020). https://doi.org/10.1038/s41467-020-14747-6

138. A. Chaves, J.G. Azadani, H. Alsalman, D.R. da Costa, R. Frisenda et al., Bandgap engineering of two-dimensional semiconductor materials. NPJ 2D Mater. Appl. **4**, 29 (2020). https://doi.org/10.1038/s41699-020-00162-4

139. J. Mao, F. Uemura, S.A. Yazdani, Y. Yin, H. Sato et al., Ultrafast perovskite electro-optic modulator and multi-band transmission up to 300 Gbit s^{-1}. Commun. Mater. **5**, 114 (2024). https://doi.org/10.1038/s43246-024-00558-5

140. A. Khalid, M.I. Malik, I. Qasim, Analysis and performance evaluation of non-toxic organo-metal halide $(CH_3NH_3SnI_3)$ perovskite optical absorber based photovoltaic cell. Chem. Inorg. Mater. **5**, 100083 (2025). https://doi.org/10.1016/j.cinorg.2024.100083

141. S.M. Hasnain, I. Qasim, A. Iqbal, M.A. Mir, N. Abu-Libdeh, Novel dual absorber configuration for eco-friendly perovskite solar cells: design, numerical investigations and performance of $ITO-C_{60}-MASnI_3-RbGeI_3-Cu_2O-Au$. Sol. Energy **278**, 112788 (2024). https://doi.org/10.1016/j.solener.2024.112788

142. A. Javed, M.F. Nasir, I. Qasim, Y.M. Alanazi, M.T. Khan, Numerical modelling of an effective perovskite solar cell and PV-module for comparison analysis of organic and inorganic electron transport layers. Int. J. Electrochem. Sci. **19**(8), 100641 (2024). https://doi.org/10.1016/j.ijoes.2024.100641

143. A. Basit, I. Qasim, Optimizing solar cell and module design with SnO_2-ETL and organometal-halide perovskite absorber: SCAPS-1D and PVSyst analysis. Wirel. Power Transf. **12**(1), e001 (2025). https://doi.org/10.48130/wpt-0024-0015

144. O. Ahmad, I. Qasim, S.M. Hasnain, Z.U. Abdin, M.F. Nasir et al., Modelling and numerical simulations of eco-friendly double absorber solar cell "Spiro-OmeTAD/CIGS/$MASnI_3$/CdS/ZnO" and its PV-module. Org. Electron. **117**, 106781 (2023). https://doi.org/10.1016/j.orgel.2023.106781

145. M.S. Hanif, I. Qasim, M.I. Malik, M.F. Nasir, O. Ahmad et al., Development of low-cost and high-efficiency solar modules based on perovskite solar cells for large-scale applications. Heliyon **10**(4), e25703 (2024). https://doi.org/10.1016/j.heliyon.2024.e25703

146. Y.-M. He, G. Clark, J.R. Schaibley, Y. He, M.-C. Chen et al., Single quantum emitters in monolayer semiconductors. Nat. Nanotechnol. **10**(6), 497–502 (2015). https://doi.org/10.1038/nnano.2015.75

147. H. Tsai, F. Liu, S. Shrestha, K. Fernando, S. Tretiak et al., A sensitive and robust thin-film X-ray detector using 2D layered perovskite diodes. Sci. Adv. **6**(15), eaay0815 (2020). https://doi.org/10.1126/sciadv.aay0815

148. J.Q. Grim, A.S. Bracker, M. Zalalutdinov, S.G. Carter, A.C. Kozen et al., Scalable in operando strain tuning in nanophotonic waveguides enabling three-quantum-dot superradiance. Nat. Mater. **18**(9), 963–969 (2019). https://doi.org/10.1038/s41563-019-0418-0

149. X. Yang, L. Ma, M. Yu, H.-H. Chen, Y. Ji et al., Focus on perovskite emitters in blue light-emitting diodes. Light Sci. Appl. **12**(1), 177 (2023). https://doi.org/10.1038/s41377-023-01206-2

150. M. Kober-Czerny, S.G. Motti, P. Holzhey, B. Wenger, J. Lim et al., Excellent long-range charge-carrier mobility in 2D perovskites. Adv. Funct. Mater. **32**(36), 2203064 (2022). https://doi.org/10.1002/adfm.202203064

151. S. Kar, K. Dey, Instabilities and degradation in perovskite materials and devices. Perovskite Optoelectronic Devices. Springer International Publishing, (2024)., pp 573–637 https://doi.org/10.1007/978-3-031-57663-8_17

152. R. Potyrailo, K. Rajan, K. Stoewe, I. Takeuchi, B. Chisholm et al., Combinatorial and high-throughput screening of materials libraries: review of state of the art. ACS Comb. Sci. **13**(6), 579–633 (2011). https://doi.org/10.1021/co200007w

153. D.I. Kutsarov, E. Rezaee, J. Lambert, W.T. Stroud, A. Panagiotopoulos et al., Progress in flexible perovskite solar cells: paving the way for scalable manufacturing. Adv. Mater. Technol. 2401834 (2025). https://doi.org/10.1002/admt.20240 1834

154. C. Cho, S. Feldmann, K.M. Yeom, Y.W. Jang, S. Kahmann et al., Efficient vertical charge transport in polycrystalline halide perovskites revealed by four-dimensional tracking of charge carriers. Nat. Mater. **21**(12), 1388–1395 (2022). https://doi.org/10.1038/s41563-022-01395-y

155. J. Liang, Z. Zhang, Y. Zheng, X. Wu, J. Wang et al., Overcoming the carrier transport limitation in Ruddlesden-Popper perovskite films by using lamellar nickel oxide substrates. J. Mater. Chem. A **9**(19), 11741–11752 (2021). https://doi.org/10.1039/d1ta01038g

156. Z. Xu, D. Lu, X. Dong, M. Chen, Q. Fu et al., Highly efficient and stable Dion−Jacobson perovskite solar cells enabled by extended π-conjugation of organic spacer. Adv. Mater. **33**(51), 2105083 (2021). https://doi.org/10.1002/adma.20210 5083

157. S.S. Hong, J.H. Yu, D. Lu, A.F. Marshall, Y. Hikita et al., Two-dimensional limit of crystalline order in perovskite membrane films. Sci. Adv. **3**(11), eaao5173 (2017). https://doi.org/10.1126/sciadv.aao5173

158. L. Zhao, H. Tian, S.H. Silver, A. Kahn, T.-L. Ren et al., Ultrasensitive heterojunctions of graphene and 2D perovskites reveal spontaneous iodide loss. Joule **2**(10), 2133–2144 (2018). https://doi.org/10.1016/j.joule.2018.07.011

159. H. Pan, J. Chen, R. Cao, V. Murugesan, N.N. Rajput et al., Non-encapsulation approach for high-performance Li–S batteries through controlled nucleation and growth. Nat. Energy **2**(10), 813–820 (2017). https://doi.org/10.1038/s41560-017-0005-z

160. L.J. Sutherland, H.C. Weerasinghe, G.P. Simon, A review on emerging barrier materials and encapsulation strategies for flexible perovskite and organic photovoltaics. Adv. Energy Mater. **11**(34), 2101383 (2021). https://doi.org/10.1002/aenm.202101383

161. X. Wang, K. Rakstys, K. Jack, H. Jin, J. Lai et al., Engineering fluorinated-cation containing inverted perovskite solar cells with an efficiency of >21% and improved stability towards humidity. Nat. Commun. **12**(1), 52 (2021). https://doi.org/10.1038/s41467-020-20272-3

162. J. Yang, E.L. Lim, L. Tan, Z. Wei, Ink engineering in blade-coating large-area perovskite solar cells. Adv. Energy Mater. **12**(28), 2200975 (2022). https://doi.org/10.1002/aenm.20220 0975

163. B. Dou, J.B. Whitaker, K. Bruening, D.T. Moore, L.M. Wheeler et al., Roll-to-roll printing of perovskite solar cells. ACS Energy Lett. **3**(10), 2558–2565 (2018). https://doi.org/10.1021/acsenergylett.8b01556

164. J. Li, Y. Yang, Z. Ye, D. Chen, J. Cui et al., Controlled high-quality perovskite single crystals growth for radiation detection: Nucleation and growth kinetics of antisolvent vapor-assisted crystallization. J. Mater. Sci. Technol. **232**, 276–282 (2025). https://doi.org/10.1016/j.jmst.2025.02.019

165. Q. Tao, P. Xu, M. Li, W. Lu, Machine learning for perovskite materials design and discovery. NPJ Comput. Mater. **7**, 23 (2021). https://doi.org/10.1038/s41524-021-00495-8

166. X. Zeng, A.V. Pogrebnyakov, A. Kotcharov, J.E. Jones, X.X. Xi et al., *In situ* epitaxial MgB_2 thin films for superconducting electronics. Nat. Mater. **1**(1), 35–38 (2002). https://doi.org/10.1038/nmat703

167. Y. Hu, Y. Chu, Q. Wang, Z. Zhang, Y. Ming et al., Standardizing perovskite solar modules beyond cells. Joule **3**(9), 2076–2085 (2019). https://doi.org/10.1016/j.joule.2019.08.015

168. K. Kang, H. Ahn, Y. Song, W. Lee, J. Kim et al., High-performance solution-processed organo-metal halide perovskite unipolar resistive memory devices in a cross-bar array structure. Adv. Mater. **31**(21), 1804841 (2019). https://doi.org/10.1002/adma.201804841

169. C.V. Mary Vijila, P.S. Subin, M. Shaji, K.R. Kumar, M.K. Jayaraj, Perovskite quantum dot based resistive memory with very low operating power. The 3rd International Conference on Optoelectronic and Nano Materials for Advanced Technology (icONMAT 2019) Kerala, India. Author(s), (2019). 070004. https://doi.org/10.1063/1.5093879

170. H. Yang, Y. Yan, X. Wu, Y. Liu, Q. Chen et al., A multilevel vertical photonic memory transistor based on organic semiconductor/inorganic perovskite quantum dot blends. J. Mater. Chem. C **8**(8), 2861–2869 (2020). https://doi.org/10.1039/c9tc06622e

171. Y. Hu, F. Florio, Z. Chen, W.A. Phelan, M.A. Siegler et al., A chiral switchable photovoltaic ferroelectric 1D perovskite. Sci. Adv. **6**(9), eaay4213 (2020). https://doi.org/10.1126/sciadv.aay4213

172. X. Song, H. Yin, Q. Chang, Y. Qian, C. Lyu et al., One-dimensional $(NH=CINH_3)_3PbI_5$ perovskite for ultralow power consumption resistive memory. Research **2021**, 9760729 (2021). https://doi.org/10.34133/2021/9760729

173. G. Abbas, M. Hassan, Q. Khan, H. Wang, G. Zhou et al., A low power-consumption and transient nonvolatile memory based on highly dense all-inorganic perovskite films. Adv. Electron. Mater. **8**(9), 2101412 (2022). https://doi.org/10.1002/aelm.202101412

174. J.-Y. Seo, J. Choi, H.-S. Kim, J. Kim, J.-M. Yang et al., Wafer-scale reliable switching memory based on 2-dimensional layered organic–inorganic halide perovskite. Nanoscale **9**(40), 15278–15285 (2017). https://doi.org/10.1039/C7NR05582J

175. D. Lee, B. Hwang, J.-S. Lee, Impact of grain sizes on programmable memory characteristics in two-dimensional organic–inorganic hybrid perovskite memory. ACS Appl. Mater. Interfaces **11**(22), 20225–20231 (2019). https://doi.org/10.1021/acsami.9b05038

176. X.-F. Cheng, X. Hou, J. Zhou, B.-J. Gao, J.-H. He et al., Pseudohalide-induced 2D $(CH_3NH_3)_2PbI_2(SCN)_2$ perovskite for ternary resistive memory with high performance. Small **14**(12), 1703667 (2018). https://doi.org/10.1002/smll.201703667

177. H. Kim, M.-J. Choi, J.M. Suh, J.S. Han, S.G. Kim et al., Quasi-2D halide perovskites for resistive switching devices with ON/OFF ratios above 109. NPG Asia Mater. **12**, 21 (2020). https://doi.org/10.1038/s41427-020-0202-2

178. S. Lee, H. Kim, D.H. Kim, W.B. Kim, J.M. Lee et al., Tailored 2D/3D halide perovskite heterointerface for substantially enhanced endurance in conducting bridge resistive switching memory. ACS Appl. Mater. Interfaces **12**(14), 17039–17045 (2020). https://doi.org/10.1021/acsami.9b22918

179. H. An, W.K. Kim, C. Wu, T.W. Kim, Highly-stable memristive devices based on poly(methylmethacrylate): $CsPbCl_3$ perovskite quantum dot hybrid nanocomposites. Org. Electron. **56**, 41–45 (2018). https://doi.org/10.1016/j.orgel.2018.02.001

180. M.-C. Yen, C.-J. Lee, K.-H. Liu, Y. Peng, J. Leng et al., All-inorganic perovskite quantum dot light-emitting memories. Nat. Commun. **12**, 4460 (2021). https://doi.org/10.1038/s41467-021-24762-w

181. T.D. Dongale, N.B. Mullani, V.B. Patil, R.S. Tikke, P.S. Pawar et al., Mimicking the biological synapse functions of analog memory, synaptic weights, and forgetting with ZnO-based memristive devices. J. Nanosci. Nanotechnol. **18**(11), 7758–7766 (2018). https://doi.org/10.1166/jnn.2018.15540

182. Y.J. Jeon, H. An, Y. Kim, Y.P. Jeon, T.W. Kim, Highly reliable memristive devices with synaptic behavior *via* facilitating ion transport of the zeolitic imidazolate framework-8 embedded into a polyvinylpyrrolidone polymer matrix. Appl. Surf. Sci. **567**, 150748 (2021). https://doi.org/10.1016/j.apsusc.2021.150748

183. C.D. Wright, P. Hosseini, J.A.V. Diosdado, Beyond von-Neumann computing with nanoscale phase-change memory devices. Adv. Funct. Mater. **23**(18), 2248–2254 (2013). https://doi.org/10.1002/adfm.201202383

184. K. Sun, J. Chen, X. Yan, The future of memristors: materials engineering and neural networks. Adv. Funct. Mater. **31**(8), 2006773 (2021). https://doi.org/10.1002/adfm.202006773

185. C. Tian, L. Wei, Y. Li, J. Jiang, Recent progress on two-dimensional neuromorphic devices and artificial neural network. Curr. Appl. Phys. **31**, 182–198 (2021). https://doi.org/10.1016/j.cap.2021.08.014

186. T. Liu, R. Yan, H. Huang, L. Pan, X. Cao et al., A micromolding method for transparent and flexible thin-film supercapacitors and hybrid supercapacitors. Adv. Funct. Mater. **30**(46), 2004410 (2020). https://doi.org/10.1002/adfm.202004410

187. L. Sun, W. Wang, H. Yang, Recent progress in synaptic devices based on 2D materials. Adv. Intell. Syst. **2**(5), 1900167 (2020). https://doi.org/10.1002/aisy.201900167

188. S. Seo, J.-J. Lee, H.-J. Lee, H.W. Lee, S. Oh et al., Recent progress in artificial synapses based on two-dimensional van der waals materials for brain-inspired computing. ACS Appl. Electron. Mater. **2**(2), 371–388 (2020). https://doi.org/10.1021/acsaelm.9b00694

189. S. Oh, S. Jung, M.H. Ali, J.-H. Kim, H. Kim et al., Highly stable artificial synapse consisting of low-surface defect van der waals and self-assembled materials. ACS Appl. Mater. Interfaces **12**(34), 38299–38305 (2020). https://doi.org/10.1021/acsami.0c07394

190. V. Gupta, G. Lucarelli, S. Castro-Hermosa, T. Brown, M. Ottavi, Characterisation & modelling of perovskite-based synaptic memristor device. Microelectron. Reliab. **111**, 113708 (2020). https://doi.org/10.1016/j.microrel.2020.113708

191. D. Hao, J. Zhang, S. Dai, J. Zhang, J. Huang, Perovskite/organic semiconductor-based photonic synaptic transistor for artificial visual system. ACS Appl. Mater. Interfaces **12**(35), 39487–39495 (2020). https://doi.org/10.1021/acsami.0c10851

192. Y. Sun, L. Qian, D. Xie, Y. Lin, M. Sun et al., Photoelectric synaptic plasticity realized by 2D perovskite. Adv. Funct. Mater. **29**(28), 1902538 (2019). https://doi.org/10.1002/adfm.201902538

193. S.H. Jo, T. Chang, I. Ebong, B.B. Bhadviya, P. Mazumder et al., Nanoscale memristor device as synapse in neuromorphic systems. Nano Lett. **10**(4), 1297–1301 (2010). https://doi.org/10.1021/nl904092h

194. S.-I. Kim, Y. Lee, M.-H. Park, G.-T. Go, Y.-H. Kim et al., Dimensionality dependent plasticity in halide perovskite artificial synapses for neuromorphic computing. Adv. Electron. Mater. **5**(9), 1900008 (2019). https://doi.org/10.1002/aelm.201900008

195. L. Qian, Y. Sun, M. Wu, C. Li, D. Xie et al., A lead-free two-dimensional perovskite for a high-performance flexible photoconductor and a light-stimulated synaptic device. Nanoscale **10**(15), 6837–6843 (2018). https://doi.org/10.1039/C8NR00914G

196. M. Kumar, H.-S. Kim, D.Y. Park, M.S. Jeong, J. Kim, Compliance-free multileveled resistive switching in a transparent 2D perovskite for neuromorphic computing. ACS Appl. Mater. Interfaces **10**(15), 12768–12772 (2018). https://doi.org/10.1021/acsami.7b19406

197. T. Ohno, T. Hasegawa, T. Tsuruoka, K. Terabe, J.K. Gimzewski et al., Short-term plasticity and long-term potentiation mimicked in single inorganic synapses. Nat. Mater. **10**(8), 591–595 (2011). https://doi.org/10.1038/nmat3054

198. R. Ferreira, M. Shaikh, S.K. Jakka, J. Deuermeier, P. Barquinha et al., Bandlike transport in FaPbBr$_3$ quantum dot phototransistor with high hole mobility and ultrahigh photodetectivity. Nano Lett. **22**(22), 9020–9026 (2022). https://doi.org/10.1021/acs.nanolett.2c03317

199. V. Darshan, V.R. Rajeev, K.N. Narayanan Unni, Enhanced performance of room temperature ammonia sensors using morphology-controlled organic field-effect transistors. Org. Electron. **98**, 106280 (2021). https://doi.org/10.1016/j.orgel.2021.106280

200. S. Rehman, H. Kim, M.F. Khan, J.-H. Hur, J. Eom et al., Tunable resistive switching of vertical ReSe$_2$/graphene hetero-structure enabled by Schottky barrier height and DUV light. J. Alloys Compd. **855**, 157310 (2021). https://doi.org/10.1016/j.jallcom.2020.157310

201. X. Guo, L. Han, X. Hou, Insights into the device structure, processing and material design for an organic thin-film transistor towards functional circuit integration. Mater. Chem. Front. **5**(18), 6760–6778 (2021). https://doi.org/10.1039/d1qm00334h

202. J. Liu, Z. Yang, Z. Gong, Z. Shen, Y. Ye et al., Weak light-stimulated synaptic hybrid phototransistors based on island-like perovskite films prepared by spin coating. ACS Appl.

203. S. Aynehband, M. Mohammadi, R. Poushimin, J.-M. Nunzi, A. Simchi, Efficient FAPbI$_3$–PbS quantum dot graphene-based phototransistors. New J. Chem. **45**(34), 15285–15293 (2021). https://doi.org/10.1039/D1NJ03139B

204. W. Zhao, T. Chen, W. Wang, S. Bi, M. Jiang et al., Layer-by-layer 2D ultrathin conductive Cu$_3$(HHTP)$_2$ film for high-performance flexible transparent supercapacitors. Adv. Mater. Interfaces **8**(11), 2100308 (2021). https://doi.org/10.1002/admi.202100308

205. A. Subramanian, S. Hussain, N. Din, G. Abbas, A. Shuja et al., Solution-processed vertical field-effect transistor with separated charge generation and charge transport layers for high-performance near-infrared photodetection. ACS Appl. Electron. Mater. **2**(12), 3871–3879 (2020). https://doi.org/10.1021/acsaelm.0c00707

206. C. Chen, X. Zhang, G. Wu, H. Li, H. Chen, Visible-light ultrasensitive solution-prepared layered organic–inorganic hybrid perovskite field-effect transistor. Adv. Opt. Mater. **5**(2), 1600539 (2017). https://doi.org/10.1002/adom.201600539

207. X. Song, S. Liu, L. Ren, Y. Zuo, S. Wang et al., Two-dimensionalization of 3D perovskites for passive narrowband Photodetection. EcoMat **6**(7), e12472 (2024). https://doi.org/10.1002/eom2.12472

208. H. Wang, Y. Chen, E. Lim, X. Wang, S. Yuan et al., High-performance lead-free two-dimensional perovskite photo transistors assisted by ferroelectric dielectrics. J. Mater. Chem. C **6**(46), 12714–12720 (2018). https://doi.org/10.1039/C8TC04691C

209. F. Zhang, Q. Zhang, X. Liu, Y. Hu, Z. Lou et al., Property modulation of two-dimensional lead-free perovskite thin films by aromatic polymer additives for performance enhancement of field-effect transistors. ACS Appl. Mater. Interfaces **13**(20), 24272–24284 (2021). https://doi.org/10.1021/acsami.1c03041

210. Y. Park, M.-K. Kim, J.-S. Lee, 2D layered metal-halide perovskite/oxide semiconductor-based broadband optoelectronic synaptic transistors with long-term visual memory. J. Mater. Chem. C **9**(4), 1429–1436 (2021). https://doi.org/10.1039/d0tc04250a

211. X. Xu, W. Deng, X. Zhang, L. Huang, W. Wang et al., Dual-band, high-performance phototransistors from hybrid perovskite and organic crystal array for secure communication applications. ACS Nano **13**(5), 5910–5919 (2019). https://doi.org/10.1021/acsnano.9b01734

212. B. Pradhan, S. Das, J. Li, F. Chowdhury, J. Cherusseri et al., Ultrasensitive and ultrathin phototransistors and photonic synapses using perovskite quantum dots grown from graphene lattice. Sci. Adv. **6**(7), eaay5225 (2020). https://doi.org/10.1126/sciadv.aay5225

213. Y. Zou, F. Li, C. Zhao, J. Xing, Z. Yu et al., Anomalous ambipolar phototransistors based on all-inorganic CsPbBr$_3$ perovskite at room temperature. Adv. Opt. Mater. **7**(21), 1900676 (2019). https://doi.org/10.1002/adom.201900676

Mater. Interfaces **13**(11), 13362–13371 (2021). https://doi.org/10.1021/acsami.0c22604

214. J. Jiang, X. Zou, Y. Lv, Y. Liu, W. Xu et al., Rational design of Al_2O_3/2D perovskite heterostructure dielectric for high performance MoS_2 phototransistors. Nat. Commun. **11**, 4266 (2020). https://doi.org/10.1038/s41467-020-18100-9

215. L. Qian, Y. Sun, M. Wu, D. Xie, L. Ding et al., A solution-processed high-performance phototransistor based on a perovskite composite with chemically modified graphenes. Adv. Mater. **29**(22), 1606175 (2017). https://doi.org/10.1002/adma.201606175

216. J. Chen, W. Ouyang, W. Yang, J.-H. He, X. Fang, Recent progress of heterojunction ultraviolet photodetectors: materials, integrations, and applications. Adv. Funct. Mater. **30**(16), 1909909 (2020). https://doi.org/10.1002/adfm.201909909

217. F.P. García de Arquer, A. Armin, P. Meredith, E.H. Sargent, Solution-processed semiconductors for next-generation photodetectors. Nat. Rev. Mater. **2**(3), 16100 (2017). https://doi.org/10.1038/natrevmats.2016.100

218. K. Chandra Sekhar Reddy, V. Selamneni, M.G. Syamala Rao, J. Meza-Arroyo, P. Sahatiya et al., All solution processed flexible p-NiO/n-CdS rectifying junction: Applications towards broadband photodetector and human breath monitoring. Appl. Surf. Sci. **568**, 150944 (2021). https://doi.org/10.1016/j.apsusc.2021.150944

219. T. Handa, T. Aharen, A. Wakamiya, Y. Kanemitsu, Radiative recombination and electron-phonon coupling in lead-free $CH_3NH_3SnI_3$ perovskite thin films. Phys. Rev. Mater. **2**(7), 075402 (2018). https://doi.org/10.1103/PhysRevMaterials.2.075402

220. X. Fu, S. Jiao, Y. Jiang, L. Li, X. Wang et al., Large-scale growth of ultrathin low-dimensional perovskite nanosheets for high-detectivity photodetectors. ACS Appl. Mater. Interfaces **12**(2), 2884–2891 (2020). https://doi.org/10.1021/acsami.9b18826

221. P.K. Roy, R.K. Ulaganathan, C.M. Raghavan, S.M. Mhatre, H.-I. Lin et al., Unprecedented random lasing in 2D organolead halide single-crystalline perovskite microrods. Nanoscale **12**(35), 18269–18277 (2020). https://doi.org/10.1039/d0nr01171a

222. H. Jing, R. Peng, R.-M. Ma, J. He, Y. Zhou et al., Flexible ultrathin single-crystalline perovskite photodetector. Nano Lett. **20**(10), 7144–7151 (2020). https://doi.org/10.1021/acs.nanolett.0c02468

223. D. Wen, X. Wang, L. Liu, C. Hu, C. Sun et al., Inkjet printing transparent and conductive MXene ($Ti_3C_2T_x$) films: a strategy for flexible energy storage devices. ACS Appl. Mater. Interfaces **13**(15), 17766–17780 (2021). https://doi.org/10.1021/acsami.1c00724

224. B. Yang, X. Ouyang, X. Zhao, J. Su, Y. Li et al., Inch-sized 2D perovskite single-crystal scintillators for high-resolution neutron and X-ray imaging. InfoMat **7**(4), e12648 (2025). https://doi.org/10.1002/inf2.12648

225. S. Li, Y. Zhang, W. Yang, H. Liu, X. Fang, 2D perovskite $Sr_2Nb_3O_{10}$ for high-performance UV photodetectors. Adv. Mater. **32**(7), 1905443 (2020). https://doi.org/10.1002/adma.201905443

226. B. Hwang, Y. Park, J.-S. Lee, Impact of grain size on the optoelectronic performance of 2D Ruddlesden-Popper perovskite-based photodetectors. J. Mater. Chem. C **9**(1), 110–116 (2021). https://doi.org/10.1039/d0tc04350h

227. Y. Lin, J. Chen, M.M. Tavakoli, Y. Gao, Y. Zhu et al., Printable fabrication of a fully integrated and self-powered sensor system on plastic substrates. Adv. Mater. **31**(5), 1804285 (2019). https://doi.org/10.1002/adma.201804285

228. J. Wang, J. Li, S. Lan, C. Fang, H. Shen et al., Controllable growth of centimeter-sized 2D perovskite heterostructures for highly narrow dual-band photodetectors. ACS Nano **13**(5), 5473–5484 (2019). https://doi.org/10.1021/acsnano.9b00259

229. L. Qian, Y. Sun, M. Sun, Z. Fang, L. Li et al., 2D perovskite microsheets for high-performance photodetectors. J. Mater. Chem. C **7**(18), 5353–5358 (2019). https://doi.org/10.1039/c9tc00138g

230. M. Dyksik, S. Wang, W. Paritmongkol, D.K. Maude, W.A. Tisdale et al., Tuning the excitonic properties of the 2D $(PEA)_2(MA)_{n-1}Pb_nI_{3n+1}$ Perovskite family *via* quantum confinement. J. Phys. Chem. Lett. **12**(6), 1638–1643 (2021). https://doi.org/10.1021/acs.jpclett.0c03731

231. Z. Yin, J. Leng, S. Wang, G. Liang, W. Tian et al., Auger-assisted electron transfer between adjacent quantum wells in two-dimensional layered perovskites. J. Am. Chem. Soc. **143**(12), 4725–4731 (2021). https://doi.org/10.1021/jacs.1c00424

232. I. Bülthoff, W. Jung, R.G. Armann, C. Wallraven, Predominance of eyes and surface information for face race categorization. Sci. Rep. **11**(1), 1–9 (2021). https://doi.org/10.48550/arXiv.2108.04983

233. V.M. Montaño-Serrano, J.M. Jacinto-Villegas, A.H. Vilchis-González, O. Portillo-Rodríguez, Artificial vision algorithms for socially assistive robot applications: a review of the literature. Sensors **21**(17), 5728 (2021). https://doi.org/10.3390/s21175728

234. H. Tian, X. Wang, F. Wu, Y. Yang, T.-L. Ren, High performance 2D perovskite/graphene optical synapses as artificial eyes. 2018 IEEE International Electron Devices Meeting (IEDM). December 1–5, 2018, San Francisco, CA, USA. IEEE, (2018)., 38.6.1–38.6.4. https://doi.org/10.1109/IEDM.2018.8614666

235. Z. Xu, C. Wu, Y. Zhu, S. Ju, F. Ma et al., Bio-inspired smart electronic-skin based on inorganic perovskite nanoplates for application in photomemories and mechanoreceptors. Nanoscale **13**(1), 253–260 (2021). https://doi.org/10.1039/D0NR06550A

236. S.L. Hart, Beyond greening: Strategies for a sustainable world. Harvard Business Review **1**, 66–76 (1997). https://doi.org/10.1080/00076799700000047

237. V.G. Gude, N. Nirmalakhandan, S. Deng, Renewable and sustainable approaches for desalination. Renew. Sustain. Energy Rev. **14**(9), 2641–2654 (2010). https://doi.org/10.1016/j.rser.2010.06.008

238. P. Ron, C. Wilder, *The Clean Tech Revolution*. (Betascript Publishing 2007), pp. 112–115.

239. M. Grätzel, The light and shade of perovskite solar cells. Nat. Mater. **13**(9), 838–842 (2014). https://doi.org/10.1038/nmat4065

240. D.M. Chapin, C.S. Fuller, G.L. Pearson, A new silicon p-n junction photocell for converting solar radiation into electrical power. J. Appl. Phys. **25**(5), 676–677 (1954). https://doi.org/10.1063/1.1721711

241. G. Wang, Q. Su, H. Tang, H. Wu, H. Lin et al., 27.09%-efficiency silicon heterojunction back contact solar cell and going beyond. Nat. Commun. **15**(1), 8931 (2024). https://doi.org/10.1038/s41467-024-53275-5

242. X. Ru, M. Yang, S. Yin, Y. Wang, C. Hong et al., Silicon heterojunction solar cells achieving 26.6% efficiency on commercial-size p-type silicon wafer. Joule **8**(4), 1092–1104 (2024). https://doi.org/10.1016/j.joule.2024.01.015

243. H. Lin, M. Yang, X. Ru, G. Wang, S. Yin et al., Silicon heterojunction solar cells with up to 26.81% efficiency achieved by electrically optimized nanocrystalline-silicon hole contact layers. Nat. Energy **8**(8), 789–799 (2023). https://doi.org/10.1038/s41560-023-01255-2

244. L. Pereira, D. Brida, E. Fortunato, I. Ferreira, H. Águas et al., A-Si: H interface optimisation for thin film position sensitive detectors produced on polymeric substrates. J. Non Cryst. Solids **299**, 1289–1294 (2002). https://doi.org/10.1016/S0022-3093(01)01150-4

245. H. Águas, R. Martins, E. Fortunato, Role of ion bombardment on the properties of a-Si: H films. Vacuum **60**(1–2), 247–254 (2001). https://doi.org/10.1016/S0042-207X(00)00391-2

246. R. Martins, I. Ferreira, H. Águas, V. Silva, E. Fortunato et al., Engineering of a-Si: H device stability by suitable design of interfaces. Sol. Energy Mater. Sol. Cells **73**(1), 39–49 (2002). https://doi.org/10.1016/S0927-0248(01)00109-X

247. S. Morawiec, M.J. Mendes, S.A. Filonovich, T. Mateus, S. Mirabella et al., Broadband photocurrent enhancement in a-Si: H solar cells with plasmonic back reflectors. Opt. Express **22**(Suppl 4), A1059–A1070 (2014). https://doi.org/10.1364/OE.22.0A1059

248. D. Gaspar, A.C. Pimentel, M.J. Mendes, T. Mateus, B.P. Falcão et al., Ag and Sn nanoparticles to enhance the near-infrared absorbance of a-Si: H thin films. Plasmonics **9**(5), 1015–1023 (2014). https://doi.org/10.1007/s11468-014-9709-0

249. P. Narchi, J. Alvarez, P. Chrétien, G. Picardi, R. Cariou et al., Cross-sectional investigations on epitaxial silicon solar cells by kelvin and conducting probe atomic force microscopy: effect of illumination. Nanoscale Res. Lett. **11**(1), 55 (2016). https://doi.org/10.1186/s11671-016-1268-1

250. R. Cariou, W. Chen, I. Cosme-Bolanos, J.-L. Maurice, M. Foldyna et al., Ultrathin PECVD epitaxial Si solar cells on glass *via* low-temperature transfer process. Prog. Photovolt: Res. Appl. **24**(8), 1075–1084 (2016). https://doi.org/10.1002/pip.2762

251. H. Águas, S.K. Ram, A. Araújo, D. Gaspar, A. Vicente et al., Silicon thin film solar cells on commercial tiles. Energy Environ. Sci. **4**(11), 4620 (2011). https://doi.org/10.1039/c1ee02303a

252. G. Ribeiro, G. Ferreira, U.D. Menda, M. Alexandre, M.J. Brites et al., Sub-bandgap sensitization of perovskite semiconductors *via* colloidal quantum dots incorporation. Nanomaterials **13**(17), 2447 (2023). https://doi.org/10.3390/nano13172447

253. I.M. Santos, M. Alexandre, V.D. Mihailetchi, J.A. Silva, T. Mateus et al., Optically-boosted planar IBC solar cells with electrically-harmless photonic nanocoatings. Adv. Opt. Mater. **11**(15), 2300276 (2023). https://doi.org/10.1002/adom.202300276

254. S. Haque, M. Alexandre, A.T. Vicente, K. Li, C.S. Schuster et al., Photon shifting and trapping in perovskite solar cells for improved efficiency and stability. Light Sci. Appl. **13**(1), 238 (2024). https://doi.org/10.1038/s41377-024-01559-2

255. H.-S. Kim, C.-R. Lee, J.-H. Im, K.-B. Lee, T. Moehl et al., Lead iodide perovskite sensitized all-solid-state submicron thin film mesoscopic solar cell with efficiency exceeding 9%. Sci. Rep. **2**, 591 (2012). https://doi.org/10.1038/srep00591

256. U.D. Menda, G. Ribeiro, D. Nunes, T. Calmeiro, H. Águas et al., High-performance wide bandgap perovskite solar cells fabricated in ambient high-humidity conditions. Mater. Adv. **2**(19), 6344–6355 (2021). https://doi.org/10.1039/D1MA00432H

257. U.D. Menda, G. Ribeiro, J. Deuermeier, E. López, D. Nunes et al., Thermal-carrier-escape mitigation in a quantum-dot-In-perovskite intermediate band solar cell *via* bandgap engineering. ACS Photonics **10**(10), 3647–3655 (2023). https://doi.org/10.1021/acsphotonics.3c00738

258. A. Capasso, F. Matteocci, L. Najafi, M. Prato, J. Buha et al., Few-layer MoS$_2$ flakes as active buffer layer for stable perovskite solar cells. Adv. Energy Mater. **6**(16), 1600920 (2016). https://doi.org/10.1002/aenm.201600920

259. H. Tsai, W. Nie, J.-C. Blancon, C.C. Stoumpos, R. Asadpour et al., High-efficiency two-dimensional Ruddlesden-Popper perovskite solar cells. Nature **536**(7616), 312–316 (2016). https://doi.org/10.1038/nature18306

260. J.H. Noh, S.H. Im, J.H. Heo, T.N. Mandal, S.I. Seok, Chemical management for colorful, efficient, and stable inorganic-organic hybrid nanostructured solar cells. Nano Lett. **13**(4), 1764–1769 (2013). https://doi.org/10.1021/nl400349b

261. M. Alexandre, H. Águas, E. Fortunato, R. Martins, M.J. Mendes, Light management with quantum nanostructured dots-in-host semiconductors. Light Sci. Appl. **10**(1), 231 (2021). https://doi.org/10.1038/s41377-021-00671-x

262. G. Grancini, C. Roldán-Carmona, I. Zimmermann, E. Mosconi, X. Lee et al., One-Year stable perovskite solar cells by 2D/3D interface engineering. Nat. Commun. **8**, 15684 (2017). https://doi.org/10.1038/ncomms15684

263. M. Chen, P. Li, C. Liang, H. Gu, W. Tong et al., Enhanced efficiency and stability of perovskite solar cells by 2D perovskite vapor-assisted interface optimization. J. Energy Chem. **45**, 103–109 (2020). https://doi.org/10.1016/j.jechem.2019.10.006

264. Y. Zheng, T. Niu, X. Ran, J. Qiu, B. Li et al., Unique characteristics of 2D Ruddlesden-Popper (2DRP) perovskite for

future photovoltaic application. J. Mater. Chem. A **7**(23), 13860–13872 (2019). https://doi.org/10.1039/c9ta03217g

265. L. Chao, Z. Wang, Y. Xia, Y. Chen, W. Huang, Recent progress on low dimensional perovskite solar cells. J. Energy Chem. **27**(4), 1091–1100 (2018). https://doi.org/10.1016/j.jechem.2017.10.013

266. N. Zhou, Y. Shen, L. Li, S. Tan, N. Liu et al., Exploration of crystallization kinetics in quasi two-dimensional perovskite and high performance solar cells. J. Am. Chem. Soc. **140**(1), 459–465 (2018). https://doi.org/10.1021/jacs.7b11157

267. S. Rabhi, K. Sekar, K. Kalna, T. Hidouri, D.P. Samajdar et al., Enhancing perovskite solar cell performance through PbI$_2$ *in situ* passivation using a one-step process: experimental insights and simulations. RSC Adv. **14**(46), 34051–34065 (2024). https://doi.org/10.1039/D4RA06193D

268. W. Zhang, Z. Liu, L. Zhang, H. Wang, C. Jiang et al., Ultrastable and efficient slight-interlayer-displacement 2D *Dion*-Jacobson perovskite solar cells. Nat. Commun. **15**(1), 5709 (2024). https://doi.org/10.1038/s41467-024-50018-4

269. J.H. Heo, S.H. Im, J.H. Noh, T.N. Mandal, C.-S. Lim et al., Efficient inorganic–organic hybrid heterojunction solar cells containing perovskite compound and polymeric hole conductors. Nat. Photonics **7**(6), 486–491 (2013). https://doi.org/10.1038/nphoton.2013.80

270. J. Burschka, N. Pellet, S.-J. Moon, R. Humphry-Baker, P. Gao et al., Sequential deposition as a route to high-performance perovskite-sensitized solar cells. Nature **499**(7458), 316–319 (2013). https://doi.org/10.1038/nature12340

271. W.S. Yang, J.H. Noh, N.J. Jeon, Y.C. Kim, S. Ryu et al., SOLAR CELLS: High-performance photovoltaic perovskite layers fabricated through intramolecular exchange. Science **348**(6240), 1234–1237 (2015). https://doi.org/10.1126/science.aaa9272

272. J.-W. Lee, D.-J. Seol, A.-N. Cho, N.-G. Park, High-efficiency perovskite solar cells based on the black polymorph of HC(NH$_2$)$_2$PbI$_3$. Adv. Mater. **26**(29), 4991–4998 (2014). https://doi.org/10.1002/adma.201401137

273. J. Qiu, Y. Xia, Y. Zheng, W. Hui, H. Gu et al., 2D intermediate suppression for efficient ruddlesden–popper (RP) phase lead-free perovskite solar cells. ACS Energy Lett. **4**(7), 1513–1520 (2019). https://doi.org/10.1021/acsenergylett.9b00954

274. D. Lu, G. Lv, Z. Xu, Y. Dong, X. Ji et al., Thiophene-based two-dimensional *Dion*-jacobson perovskite solar cells with over 15% efficiency. J. Am. Chem. Soc. **142**(25), 11114–11122 (2020). https://doi.org/10.1021/jacs.0c03363

275. M. Chen, M.-G. Ju, M. Hu, Z. Dai, Y. Hu et al., Lead-free *Dion*–jacobson tin halide perovskites for photovoltaics. ACS Energy Lett. **4**(1), 276–277 (2019). https://doi.org/10.1021/acsenergylett.8b02051

276. H. Xu, Y. Jiang, T. He, S. Li, H. Wang et al., Orientation regulation of tin-based reduced-dimensional perovskites for highly efficient and stable photovoltaics. Adv. Funct. Mater. **29**(47), 1807696 (2019). https://doi.org/10.1002/adfm.201807696

277. Y. Zhou, H.F. Garces, B.S. Senturk, A.L. Ortiz, N.P. Padture, Room temperature "one-pot" solution synthesis of nanoscale CsSnI$_3$ orthorhombic perovskite thin films and particles. Mater. Lett. **110**, 127–129 (2013). https://doi.org/10.1016/j.matlet.2013.08.011

278. H. Lai, D. Lu, Z. Xu, N. Zheng, Z. Xie et al., Organic-salt-assisted crystal growth and orientation of quasi-2D ruddlesden–popper perovskites for solar cells with efficiency over 19%. Adv. Mater. **32**(33), 2001470 (2020). https://doi.org/10.1002/adma.202001470

279. Y. Huang, Y. Li, E.L. Lim, T. Kong, Y. Zhang et al., Stable layered 2D perovskite solar cells with an efficiency of over 19% *via* multifunctional interfacial engineering. J. Am. Chem. Soc. **143**(10), 3911–3917 (2021). https://doi.org/10.1021/jacs.0c13087

280. W. Ke, C.C. Stoumpos, I. Spanopoulos, M. Chen, M.R. Wasielewski et al., Diammonium cations in the FASnI$_3$ perovskite structure lead to lower dark currents and more efficient solar cells. ACS Energy Lett. **3**(7), 1470–1476 (2018). https://doi.org/10.1021/acsenergylett.8b00687

281. H. Yao, T. Wu, C. Wu, L. Ding, Y. Hua et al., Structural tailoring the phenylenediamine isomers to obtain 2D *Dion*–jacobson tin perovskite solar cells with record efficiency. Adv. Funct. Mater. **34**(12), 2312287 (2024). https://doi.org/10.1002/adfm.202312287

282. Y. Liao, H. Liu, W. Zhou, D. Yang, Y. Shang et al., Highly oriented low-dimensional tin halide perovskites with enhanced stability and photovoltaic performance. J. Am. Chem. Soc. **139**(19), 6693–6699 (2017). https://doi.org/10.1021/jacs.7b01815

283. E. Jokar, C.-H. Chien, C.-M. Tsai, A. Fathi, E.W. Diau, Robust tin-based perovskite solar cells with hybrid organic cations to attain efficiency approaching 10%. Adv. Mater. **31**(2), 1804835 (2019). https://doi.org/10.1002/adma.201804835

284. J. Zhao, Z. Zhang, G. Li, M.H. Aldamasy, M. Li et al., Dimensional tuning in lead-free tin halide perovskite for solar cells. Adv. Energy Mater. **13**(13), 2204233 (2023). https://doi.org/10.1002/aenm.202204233

285. F. Wang, X. Jiang, H. Chen, Y. Shang, H. Liu et al., 2D-quasi-2D-3D hierarchy structure for tin perovskite solar cells with enhanced efficiency and stability. Joule **2**(12), 2732–2743 (2018). https://doi.org/10.1016/j.joule.2018.09.012

286. Y. Xu, K.-J. Jiang, P. Wang, W.-M. Gu, G.-H. Yu et al., Highly oriented quasi-2D layered tin halide perovskites with 2-thiopheneethylammonium iodide for efficient and stable tin perovskite solar cells. New J. Chem. **46**(5), 2259–2265 (2022). https://doi.org/10.1039/d1nj05178d

287. F. Li, Y. Xie, Y. Hu, M. Long, Y. Zhang et al., Effects of alkyl chain length on crystal growth and oxidation process of two-dimensional tin halide perovskites. ACS Energy Lett. **5**(5), 1422–1429 (2020). https://doi.org/10.1021/acsenergylett.0c00286

288. T. Xue, Z. Huang, P. Zhang, M. Su, X. Hu et al., A shape memory scaffold for body temperature self-repairing wearable perovskite solar cells with efficiency exceeding 21%.

InfoMat **4**(12), e12358 (2022). https://doi.org/10.1002/inf2.12358

289. C. Ma, D. Shen, B. Huang, X. Li, W.-C. Chen et al., High performance low-dimensional perovskite solar cells based on a one dimensional lead iodide perovskite. J. Mater. Chem. A **7**(15), 8811–8817 (2019). https://doi.org/10.1039/c9ta01859j

290. D. Cortecchia, J. Yin, A. Petrozza, C. Soci, White light emission in low-dimensional perovskites. J. Mater. Chem. C **7**(17), 4956–4969 (2019). https://doi.org/10.1039/c9tc01036j

291. Y. Li, W. Wang, J. Dong, Y. Lu, X. Huang et al., Modification of PEDOT: PSS to enhance device efficiency and stability of the quasi-2D perovskite light-emitting diodes. Org. Electron. **108**, 106579 (2022). https://doi.org/10.1016/j.orgel.2022.106579

292. Y. Tu, S. Wang, Y. Zhang, L. Chen, Y. Fang et al., Balanced carrier injection of quantum dots light-emitting diodes: the case of interface barrier of bilayer ZnO electron transport layer. Nanotechnology **29**(48), 485203 (2018). https://doi.org/10.1088/1361-6528/aae0b8

293. Y. Zhang, M.I. Saidaminov, I. Dursun, H. Yang, B. Murali et al., Zero-dimensional Cs_4PbBr_6 perovskite nanocrystals. J. Phys. Chem. Lett. **8**(5), 961–965 (2017). https://doi.org/10.1021/acs.jpclett.7b00105

294. C. Zhou, Y. Tian, Z. Yuan, H. Lin, B. Chen et al., Highly efficient broadband yellow phosphor based on zero-dimensional tin mixed-halide perovskite. ACS Appl. Mater. Interfaces **9**(51), 44579–44583 (2017). https://doi.org/10.1021/acsami.7b12862

295. Y. Cao, N. Wang, H. Tian, J. Guo, Y. Wei et al., Perovskite light-emitting diodes based on spontaneously formed submicrometre-scale structures. Nature **562**(7726), 249–253 (2018). https://doi.org/10.1038/s41586-018-0576-2

296. J. Xing, Y. Zhao, M. Askerka, L.N. Quan, X. Gong et al., Color-stable highly luminescent sky-blue perovskite light-emitting diodes. Nat. Commun. **9**(1), 3541 (2018). https://doi.org/10.1038/s41467-018-05909-8

297. Y. Tian, C. Zhou, M. Worku, X. Wang, Y. Ling et al., Highly efficient spectrally stable red perovskite light-emitting diodes. Adv. Mater. **30**(20), e1707093 (2018). https://doi.org/10.1002/adma.201707093

298. D. Ma, K. Lin, Y. Dong, H. Choubisa, A.H. Proppe et al., Distribution control enables efficient reduced-dimensional perovskite LEDs. Nature **599**(7886), 594–598 (2021). https://doi.org/10.1038/s41586-021-03997-z

299. L. Kong, Y. Luo, Q. Wu, X. Xiao, Y. Wang et al., Efficient and stable hybrid perovskite-organic light-emitting diodes with external quantum efficiency exceeding 40 per cent. Light. Sci. Appl. **13**, 138 (2024). https://doi.org/10.1038/s41377-024-01500-7

300. H. Wang, W. Xu, Q. Wei, S. Peng, Y. Shang et al., *In-situ* growth of low-dimensional perovskite-based insular nanocrystals for highly efficient light emitting diodes. Light Sci. Appl. **12**(1), 62 (2023). https://doi.org/10.1038/s41377-023-01112-7

301. Y. Liu, Y. Dong, T. Zhu, D. Ma, A. Proppe et al., Bright and stable light-emitting diodes based on perovskite quantum dots in perovskite matrix. J. Am. Chem. Soc. **143**(38), 15606–15615 (2021). https://doi.org/10.1021/jacs.1c02148

302. B. Wang, Y.-H. Lou, Y. Xia, F. Hu, Y.-H. Li et al., Chemical reaction modulated low-dimensional phase toward highly efficient sky-blue perovskite light-emitting diodes. Angew. Chem. Int. Ed. **63**(39), e202406140 (2024). https://doi.org/10.1002/anie.202406140

303. L.-Z. Feng, Y.-H. Song, Z.-D. Li, B.-S. Zhu, Z.-Y. Ma et al., Dimensional and doping engineering of chiral perovskites with enhanced spin selectivity for green emissive spin light-emitting diodes. Nano Lett. **24**(20), 6084–6091 (2024). https://doi.org/10.1021/acs.nanolett.4c01138

304. A. Ben Abdelhadi, M. Gutiérrez, B. Cohen, L. Lezama, M. Lachkar et al., A new eco-friendly and highly emitting Mn-based hybrid perovskite toward high-performance green down-converted LEDs. J. Mater. Chem. C **12**(1), 286–295 (2023). https://doi.org/10.1039/d3tc03821a

305. L. Kong, Y. Sun, B. Zhao, K. Ji, J. Feng et al., Fabrication of red-emitting perovskite LEDs by stabilizing their octahedral structure. Nature **631**(8019), 73–79 (2024). https://doi.org/10.1038/s41586-024-07531-9

306. T. Jun, K. Sim, S. Iimura, M. Sasase, H. Kamioka et al., Lead-free highly efficient blue-emitting $Cs_3Cu_2I_5$ with 0D electronic structure. Adv. Mater. **30**(43), e1804547 (2018). https://doi.org/10.1002/adma.201804547

307. J.-Y. Yao, H. Liu, Z.-N. Chen, B. Ma, L.-J. Xu, Low-dimensional lead-free metal halides for efficient electrically driven light-emitting diodes. Angew. Chem. Int. Ed. **64**(6), e202423185 (2025). https://doi.org/10.1002/anie.202423185

308. G. Seo, H. Jung, T.D. Creason, V. Yeddu, M. Bamidele et al., Lead-free halide light-emitting diodes with external quantum efficiency exceeding 7% using host–dopant strategy. ACS Energy Lett. **6**(7), 2584–2593 (2021). https://doi.org/10.1021/acsenergylett.1c01117

309. H. Sun, X. Yang, P. Li, Y. Bai, Q. Meng et al., Solution synthesis and light-emitting applications of one-dimensional lead-free cerium(III) metal halides. Nano Lett. **24**(33), 10355–10361 (2024). https://doi.org/10.1021/acs.nanolett.4c03019

310. W. Bai, M. Liang, T. Xuan, T. Gong, L. Bian et al., Ligand engineering enables efficient pure red tin-based perovskite light-emitting diodes. Angew. Chem. Int. Ed. **62**(50), e202312728 (2023). https://doi.org/10.1002/anie.202312728

311. L. Yang, J. Luo, J. Gao, B. Song, J. Tang, Inorganic lanthanide compounds with f–d transition: from materials to electroluminescence devices. J. Phys. Chem. Lett. **13**(19), 4365–4373 (2022). https://doi.org/10.1021/acs.jpclett.2c00927

312. D. Han, J. Wang, L. Agosta, Z. Zang, B. Zhao et al., Tautomeric mixture coordination enables efficient lead-free perovskite LEDs. Nature **622**(7983), 493–498 (2023). https://doi.org/10.1038/s41586-023-06514-6

313. C. Bi, Z. Yao, X. Sun, X. Wei, J. Wang et al., Perovskite quantum dots with ultralow trap density by acid etching-driven ligand exchange for high luminance and stable pure-blue light-emitting diodes. Adv. Mater. **33**(15), 2006722 (2021). https://doi.org/10.1002/adma.202006722

314. Y. Jiang, C. Sun, J. Xu, S. Li, M. Cui et al., Synthesis-on-substrate of quantum dot solids. Nature **612**(7941), 679–684 (2022). https://doi.org/10.1038/s41586-022-05486-3

315. H. Shao, Y. Zhai, X. Wu, W. Xu, L. Xu et al., High brightness blue light-emitting diodes based on CsPb(Cl/Br)$_3$ perovskite QDs with phenethylammonium chloride passivation. Nanoscale **12**(21), 11728–11734 (2020). https://doi.org/10.1039/D0NR02597F

316. Y.-K. Wang, K. Singh, J.-Y. Li, Y. Dong, X.-Q. Wang et al., *In situ* inorganic ligand replenishment enables bandgap stability in mixed-halide perovskite quantum dot solids. Adv. Mater. **34**(21), e2200854 (2022). https://doi.org/10.1002/adma.202200854

317. G. Xu, C. Wang, Y. Li, W. Meng, G. Luo et al., Solid-state synthesis of cesium manganese halide nanocrystals in glass with bright and broad red emission for white LEDs. Chem. Sci. **14**(20), 5309–5315 (2023). https://doi.org/10.1039/D3SC01084H

318. H. Kim, J.H. Park, K. Kim, D. Lee, M.H. Song et al., Highly emissive blue quantum dots with superior thermal stability *via in situ* surface reconstruction of mixed CsPbBr$_3$–Cs$_4$PbBr$_6$ nanocrystals. Adv. Sci. **9**(5), 2104660 (2022). https://doi.org/10.1002/advs.202104660

319. F. Haque, M. Mativenga, Halide perovskite memtransistor enabled by ion migration. Jpn. J. Appl. Phys. **59**(8), 081002 (2020). https://doi.org/10.35848/1347-4065/aba5e1

320. L. Yin, W. Huang, R. Xiao, W. Peng, Y. Zhu et al., Optically stimulated synaptic devices based on the hybrid structure of silicon nanomembrane and perovskite. Nano Lett. **20**(5), 3378–3387 (2020). https://doi.org/10.1021/acs.nanolett.0c00298

321. J. Kim, S.M. Kwon, C. Jo, J.-S. Heo, W.B. Kim et al., Highly efficient photo-induced charge separation enabled by metal–chalcogenide interfaces in quantum-dot/metal-oxide hybrid phototransistors. ACS Appl. Mater. Interfaces **12**(14), 16620–16629 (2020). https://doi.org/10.1021/acsami.0c01176

322. M. Gedda, E. Yengel, H. Faber, F. Paulus, J.A. Kreß et al., Ruddlesden-popper-phase hybrid halide perovskite/small-molecule organic blend memory transistors. Adv. Mater. **33**(7), e2003137 (2021). https://doi.org/10.1002/adma.202003137

323. K. Pei, A.H.Y. Lau, P.K.L. Chan, Understanding molecular surface doping of large bandgap organic semiconductors and overcoming the contact/access resistance in organic field-effect transistors. Phys. Chem. Chem. Phys. **22**(13), 7100–7109 (2020). https://doi.org/10.1039/d0cp00487a

324. U. Zschieschang, J.W. Borchert, M. Giorgio, M. Caironi, F. Letzkus et al., Roadmap to gigahertz organic transistors. Adv. Funct. Mater. **30**(20), 1903812 (2020). https://doi.org/10.1002/adfm.201903812

325. A. Perinot, M. Giorgio, V. Mattoli, D. Natali, M. Caironi, Organic electronics picks up the pace: mask-less, solution processed organic transistors operating at 160 MHz. Adv. Sci. **8**(4), 2001098 (2021). https://doi.org/10.1002/advs.2020 01098

326. C.-F. Lai, C.-Z. Zhong, Y.-C. Lee, Ultrastable and highly luminescent quantum dots coating highly dense protective layers of Na-poly(Al-O-Si) nanocomposites for light-emitting diodes. Adv. Mater. Interfaces **9**(35), 2201710 (2022). https://doi.org/10.1002/admi.202201710

327. X. Li, W. Cai, H. Guan, S. Zhao, S. Cao et al., Highly stable CsPbBr$_3$ quantum dots by silica-coating and ligand modification for white light-emitting diodes and visible light communication. Chem. Eng. J. **419**, 129551 (2021). https://doi.org/10.1016/j.cej.2021.129551

328. Y. Ji, M. Wang, Z. Yang, H. Qiu, S. Ji et al., Highly stable Na: CsPb(Br, I)$_3$@Al$_2$O$_3$ nanocomposites prepared by a pre-protection strategy. Nanoscale **12**(11), 6403–6410 (2020). https://doi.org/10.1039/d0nr00069h

329. I.C. Smith, E.T. Hoke, D. Solis-Ibarra, M.D. McGehee, H.I. Karunadasa, A layered hybrid perovskite solar-cell absorber with enhanced moisture stability. Angew. Chem. Int. Ed. **53**(42), 11232–11235 (2014). https://doi.org/10.1002/anie.201406466

330. J. You, Z. Hong, Y.M. Yang, Q. Chen, M. Cai et al., Low-temperature solution-processed perovskite solar cells with high efficiency and flexibility. ACS Nano **8**(2), 1674–1680 (2014). https://doi.org/10.1021/nn406020d

331. J.-C. Blancon, H. Tsai, W. Nie, C.C. Stoumpos, L. Pedesseau et al., Extremely efficient internal exciton dissociation through edge states in layered 2D perovskites. Science **355**(6331), 1288–1292 (2017). https://doi.org/10.1126/science.aal4211

332. Z. Song, C.L. McElvany, A.B. Phillips, I. Celik, P.W. Krantz et al., A technoeconomic analysis of perovskite solar module manufacturing with low-cost materials and techniques. Energy Environ. Sci. **10**(6), 1297–1305 (2017). https://doi.org/10.1039/C7EE00757D

333. Z. Song, A. Abate, S.C. Watthage, G.K. Liyanage, A.B. Phillips et al., Perovskite solar cell stability in humid air: partially reversible phase transitions in the PbI$_2$-CH$_3$NH$_3$I-H$_2$O system. Adv. Energy Mater. **6**(19), 1600846 (2016). https://doi.org/10.1002/aenm.201600846

334. J. Pan, C. Mu, Q. Li, W. Li, D. Ma et al., Room-temperature, hydrochloride-assisted, one-step deposition for highly efficient and air-stable perovskite solar cells. Adv. Mater. **28**(37), 8309–8314 (2016). https://doi.org/10.1002/adma.201601881

335. J. Almutlaq, J. Yin, O.F. Mohammed, O.M. Bakr, The benefit and challenges of zero-dimensional perovskites. J. Phys. Chem. Lett. **9**(14), 4131–4138 (2018). https://doi.org/10.1021/acs.jpclett.8b00532

336. K.A. Bush, A.F. Palmstrom, Z.J. Yu, M. Boccard, R. Cheacharoen et al., 23.6%-efficient monolithic perovskite/silicon tandem solar cells with improved stability. Nat. Energy **2**(4), 17009 (2017). https://doi.org/10.1038/nenergy.2017.9

337. V.J.Y. Lim, A.M. Ulatowski, C. Kamaraki, M.T. Klug, L. Miranda Perez et al., Air-degradation mechanisms in mixed lead-tin halide perovskites for solar cells. Adv. Energy Mater. **13**(33), 2200847 (2023). https://doi.org/10.1002/aenm.20220 0847

338. M. Pantaler, K.T. Cho, V.I.E. Queloz, I. García Benito, C. Fettkenhauer et al., Hysteresis-free lead-free double-perovskite solar cells by interface engineering. ACS Energy Lett. **3**(8), 1781–1786 (2018). https://doi.org/10.1021/acsenergylett.8b00871

339. A. Kumar, S. Singh, Numerical modeling of lead-free perovskite solar cell using inorganic charge transport materials. Mater. Today Proc. **26**, 2574–2581 (2020). https://doi.org/10.1016/j.matpr.2020.02.545

340. A. Agresti, B. Berionni Berna, S. Pescetelli, A. Catini, F. Menchini et al., Copper-based corrole as thermally stable hole transporting material for perovskite photovoltaics. Adv. Funct. Mater. **30**(46), 2003790 (2020). https://doi.org/10.1002/adfm.202003790

341. L. Lanzetta, J.M. Marin-Beloqui, I. Sanchez-Molina, D. Ding, S.A. Haque, Two-dimensional organic tin halide perovskites with tunable visible emission and their use in light-emitting devices. ACS Energy Lett. **2**(7), 1662–1668 (2017). https://doi.org/10.1021/acsenergylett.7b00414

342. M.S. Adli Azizman, A.W. Azhari, N. Ibrahim, D.S. Che Halin, S. Sepeai et al., Mixed cations tin-germanium perovskite: a promising approach for enhanced solar cell applications. Heliyon **10**(8), e29676 (2024). https://doi.org/10.1016/j.heliyon.2024.e29676

343. N. Chen, T. Cai, W. Li, K. Hills-Kimball, H. Yang et al., Yb- and Mn-doped lead-free double perovskite Cs_2AgBiX_6 (X = Cl^-, Br^-) nanocrystals. ACS Appl. Mater. Interfaces **11**(18), 16855–16863 (2019). https://doi.org/10.1021/acsami.9b02367

344. M.T. Lee, C.H. Liao, C.H. Tsai, C.H. Chen, Highly efficient, deep-blue doped organic light-emitting devices. Adv. Mater. **17**(20), 2493–2497 (2005). https://doi.org/10.1002/adma.200501169

345. F. Yang, R. Zhu, Z. Zhang, Z. Su, W. Zuo et al., High-stable lead-free solar cells achieved by surface reconstruction of quasi-2D tin-based perovskites. Adv. Mater. **36**(7), 2308655 (2024). https://doi.org/10.1002/adma.202308655

346. S. Ma, G. Yuan, Y. Zhang, N. Yang, Y. Li et al., Development of encapsulation strategies towards the commercialization of perovskite solar cells. Energy Environ. Sci. **15**(1), 13–55 (2022). https://doi.org/10.1039/D1EE02882K

347. L. Zhang, C. Sun, T. He, Y. Jiang, J. Wei et al., High-performance quasi-2D perovskite light-emitting diodes: from materials to devices. Light Sci. Appl. **10**(1), 61 (2021). https://doi.org/10.1038/s41377-021-00501-0

348. Z. Zhang, R. Ji, X. Jia, S.-J. Wang, M. Deconinck et al., Semitransparent perovskite solar cells with an evaporated ultrathin perovskite absorber. Adv. Funct. Mater. **34**(50), 2307471 (2024). https://doi.org/10.1002/adfm.202307471

349. Z. He, H. Duan, J. Zeng, J. Zhou, X. Zhong et al., Perovskite retinomorphic image sensor for embodied intelligent vision. Sci. Adv. **11**(1), eads2834 (2025). https://doi.org/10.1126/sciadv.ads2834

350. J.S. Manser, M.I. Saidaminov, J.A. Christians, O.M. Bakr, P.V. Kamat, Making and breaking of lead halide perovskites. Acc. Chem. Res. **49**(2), 330–338 (2016). https://doi.org/10.1021/acs.accounts.5b00455

351. E. Unger, T.J. Jacobsson, The perovskite database project: a perspective on collective data sharing. ACS Energy Lett. **7**(3), 1240–1245 (2022). https://doi.org/10.1021/acsenergylett.2c00330

Publisher's Note Springer Nature remains neutral with regard to jurisdictional claims in published maps and institutional affiliations.